SLAC-R-937

UNIVERSITÀ DEGLI STUDI DI PISA

FACOLTÀ DI SCIENZE M.F.N.

Measurement of D^0 lifetime with the *BABAR* detector

Dissertazione di Dottorato in Fisica

Candidato:
Gabriele Simi

Relatore:
Chiar.mo Prof. Marcello Giorgi

Anno Accademico 2000/2001

Work supported in part by US Department of Energy contract DE-AC02-76SF00515.
SLAC National Accelerator Laboratory, Menlo Park, CA 94025

Università degli Studi di Pisa

Facoltà di Scienze M.F.N.

Dissertazione di Dottorato in Fisica

Measurement of D^0 lifetime with the *BABAR* detector

Candidato:
Gabriele Simi

Relatore:
Chiar.mo Prof. Marcello Giorgi

Controrelatore:
Chiar.mo Prof.

Controrelatore:
Chiar.mo Prof.

Anno Accademico 2000/2001

Introduction

This work is the result of the researches carried out during a three years Ph.D. period in the *BABAR* experiment. The first chapter consists in an introduction to the theoretical aspects of the D^0 meson lifetime determination and *CP* violation parameters, as well as an overview of the *CP* violation in the B sector, which is the main topic of the experiment. The description of the experimental apparatus follows with particular attention to the Silicon Vertex Tracker detector, the most critical detector for the determination of decay vertices and thus of lifetimes and time dependent *CP* violation asymmetries. In the fourth chapter the operation and running of the vertex detector is described, as a result from the experience as Operation Manager of the SVT, with particular attention to the safety of the device and the data quality assurance. The last chapter is dedicated to the determination of the D^0 meson lifetime with the *BABAR* detector, which is the main data analysis carried out by the candidate. The analysis is characterized by the selection of an extremely pure sample of D^0 mesons for which the decay flight length and proper time is reconstructed. The description of the unbinned maximum likelihood fit follows, as well as the discussion of the possible sources of systematic uncertainties. In the appendix is also presented a preliminary study of a possible development regarding the determination of mixing and *CP* violation parameters for the D^0 meson.

Chapter 1

The *BABAR* experiment

The primary physics goal of the *BABAR* experiment is the systematic study of *CP*-violating asymmetries in the decay of neutral B mesons to *CP* eigenstates. Such measurements are designed to test the Standard Model prediction for *CP*-violation based on the Cabibbo-Kobayashi-Maskawa mechanism [1], but many decay modes of the B mesons permit searches for other sources of *CP* violation. The secondary goal is to perform precision measurements of decays of bottom and charm mesons and τ leptons and the search for rare processes that become accessible with the high luminosity of the PEP-II B Factory [2]. The design of the detector is optimized for *CP* studies, but it is also well suited for these other physics studies. The scientific goals of the *BABAR* experiment were first presented in the Letter of Intent [3], detailed physics studies have been documented in the *BABAR* Physics Book [4] and earlier workshops [5].

In the following we will introduce also the relevant aspects of the *CP* violation physics at this B Factory since this is its primary physics goal and motivation. We will then talk about the determination of D^0 meson lifetime with the *BABAR* detector that is the main topic of this work. As part of a future development we will introduce the aspects relative to the measurement of the mixing in the charm sector and the possibility of improving the *CP* violating parameters for the D^0 meson using doubly Cabibbo suppressed decays.

1.1 *CP* violation

1.1.1 Motivation for *CP* violation studies

Probably the most fascinating motivation of studying *CP* violation is the cosmological puzzle of the particular abundance of baryons in our local region of the universe, suggesting a disappearance of the antimatter from the universe.

Cosmological theories on the origin of the universe, such as grand unified theories or even the standard model, allow for baryon number violating processes at sufficiently high temperatures so at the thermal equilibrium in the early high temperature epochs the net baryon number of the universe is zero.

In a large class of theories the baryon number asymmetry is generated at the weak phase transition, such theories, however, must include *CP* violation from sources beyond the minimal Standard Model because calculations made in that model show that it does not generate a large enough matter-antimatter imbalance to produce the baryon number to entropy ratio observed in the universe today.

This is a hint that *CP* violation from beyond Standard Model sources is worth looking for. It is by no means a rigorous argument. There are theories in which baryon number asymmetry is generated at a much higher temperature and then protected from thermalization to zero by $B - L$ (baryon number minus lepton number) symmetry. Such theories do not in general require any new low energy *CP* violation mechanism. Neither do they forbid it.

On the other hand in many aspects of modern particle physics symmetry laws play an important role. They are related to conservation principles and most of the theories derive their laws from symmetry considerations and are thus intrinsically based on them.

CP symmetry is one of the experimentally least constrained discrete symmetries. We know that *CP* violation do occur since it has been observed in rare kaon decays [6] but it is not yet known whether the pattern of *CP* violation predicted by the minimal Standard Model is the one found in nature. The K-decay observations, together with other measurements, place constraints on the parameters of the Standard Model mixing matrix (the

CKM matrix) but do not yet provide any test. A multitude of *CP*-violating effects are expected in B decays, some of which are very cleanly predicted by the Standard Model. If a sufficient number of independent observations of *CP* violation in B decays can be made then it will be possible to test the Standard Model predictions for *CP* violation. Either the relationships between various measurements will be consistent with the Standard Model predictions and fully determine the CKM parameters or there will be no single choice of CKM parameters that is consistent with all measurements.

This latter case, of course, would be much more interesting. It would indicate that there is a contribution of physics beyond the Standard Model. There may be enough information in the pattern of the inconsistencies to learn something about the nature of the new physics contributions. Thus the aim of the game is to measure enough quantities to impose redundant constraints on Standard Model parameters, including particularly the convention-independent combinations of *CP*-violating phases of CKM matrix elements.

1.1.2 *CP* violation in field theories

We present in the following how CP violation occurs in a general field theory independently from the model assumptions.

We know that the Lagrangian function have to be a Lorentz scalar and thus can only depend on bilinear combination of the fields of the theory. The transformation properties under *CP* for combinations of fermion fields (scalar, pseudo scalar, vector, pseudo-vector) are listed in below

$$\begin{array}{lcccc} \text{term} & \bar{\psi}_i\psi_j & i\bar{\psi}_i\gamma^5\psi_j & \bar{\psi}_i\gamma^\mu\psi_j & \bar{\psi}_i\gamma^\mu\gamma^5\psi_j \\ CP \text{ transformed} & \bar{\psi}_j\psi_i & -i\bar{\psi}_j\gamma^5\psi_i & -(g^{\mu\mu})\bar{\psi}_j\gamma^\mu\psi_i & -g^{\mu\mu}\bar{\psi}_j\gamma^\mu\gamma^5\psi_i \end{array} \tag{1.1}$$

Similarly the boson fields

$$\begin{array}{lcccc} \text{term} & H & A & W^{\pm\mu} & \partial^\mu \\ CP \text{ transformed} & H & -A & -(g^{\mu\mu})W^{\mp\mu} & (g^{\mu\mu})\partial^\mu \end{array} \tag{1.2}$$

The Lagrangian function can be obtained from the combination of these terms with complex coupling constants where each combination need to appear together with its hermitian conjugate. The *CP* operator transforms each combination in its hermitian conjugate. The Lagrangian function is

invariant if the coupling constant is real, while is not invariant if the coupling constant is complex. But not all the phases that appear in the complex coupling constants have physical meaning. In fact it is always possible to redefine each field by a phase without changing the results of the theory and thus eliminate some of the phases in the coupling constants. However, if after all the possible redefinitions some phases still remain *CP* violation can occur.

1.1.3 *CP* violation in the Standard Model

In the Standard Model the *CP* violating phases are provided by the mixing matrix of the quarks. The three left-handed quark generations $\mathbf{u}' = (u, c, t)$ and $\mathbf{d}' = (d, s, b)$ are coupled to the vector bosons with the following Lagrangian

$$\mathcal{L}_W = -\frac{g}{\sqrt{2}}\bar{\mathbf{u}}'\gamma^\mu \mathbf{d}' W_\mu^+ + h.c. \tag{1.3}$$

However the fields directly coupled to the boson fields do not correspond to the states with a definite mass but they are a general linear combination with an unitary matrix M_{ij}.

$$\mathbf{u}' = {M^{(u)}}^+ \mathbf{u}, \quad \mathbf{d}' = {M^{(d)}}^+ \mathbf{d} \tag{1.4}$$

The matrix $V = M^{(u)}{M^{(d)}}^+$, often called CKM quark mixing matrix, is an unitary 3×3 complex matrix and thus have nine free parameters pf wich three are real and 6 immaginary. Five of them can be eliminated with an appropriate redefinition of the quark fields so only 4 free parameters are allowed. Three of them need to be real hence only 1 complex number is allowed in this picture. This remaining phase generates *CP* violation in the Standard Model

The unitarity of the CKM matrix implies various relations among its elements. Three of them are very useful for understanding the Standard Model predictions for *CP* violation:

$$V_{ud}V_{us}^* + V_{cd}V_{cs}^* + V_{td}V_{ts}^* = 0,$$
$$V_{us}V_{ub}^* + V_{cs}V_{cb}^* + V_{ts}V_{tb}^* = 0,$$
$$V_{ud}V_{ub}^* + V_{cd}V_{cb}^* + V_{td}V_{tb}^* = 0.$$

Each of these three relations requires the sum of three complex quantities to vanish and so can be geometrically represented in the complex plane as a triangle. These are "the unitarity triangles".

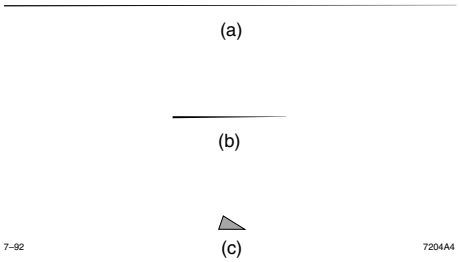

Figure 1.1: The three unitarity triangles a) $V_{id}V_{is}^* = 0$, b)$V_{is}V_{ib}^* = 0$, and c) $V_{id}V_{ib}^* = 0$, drawn to a common scale.

It is instructive to draw the three triangles, knowing the experimental values (within errors) for the various $|V_{ij}|$. In the first two triangles (fig. 1.1) , one side is much shorter than the other two, and so they almost collapse to a line. *CP* violation take origin from the interference of amplitudes related to different sides of the triangle then either the interference term is very small or the *CP* violating phase is very small. This would give an intuitive understanding of why *CP* violation is small in the leading K decays (the first triangle) and in the leading B_s decays (the second triangle). The most exciting physics of *CP* violation lies in the B system, related to the third triangle. The openness of this triangle predicts large *CP* asymmetries in B decays.

The angles of this triangle (fig. 1.2) can be expressed in terms of CKM matrix elements as follows:

$$\alpha = \left[-\frac{V_{td}V_{tb}^*}{V_{ud}V_{ub}^*}\right],\ \beta = \left[-\frac{V_{cd}V_{cb}^*}{V_{td}V_{tb}^*}\right],\ \alpha = \left[-\frac{V_{ud}V_{ub}^*}{V_{cd}V_{cb}^*}\right] \tag{1.5}$$

The measurement of all this angles in the *BABAR* experiment will allow the over determination of this triangle performing a consistency check of the standard model pattern for *CP* violation.

1.1.4 Mixing and *CP* violation at *BABAR*

Like in neutral K and D mesons, in neutral B mesons there are two flavor eigenstates, $B^0 = \bar{b}d$ and $\bar{B}^0 = \bar{d}b$, which have definite quark content and are most useful to understand particle production and particle decay processes; and there are eigenstates of the Hamiltonian, namely states of definite mass and lifetime (B_H, B_L), which propagate through space in a definite fashion. If *CP* were a good symmetry, the mass eigenstates would also be

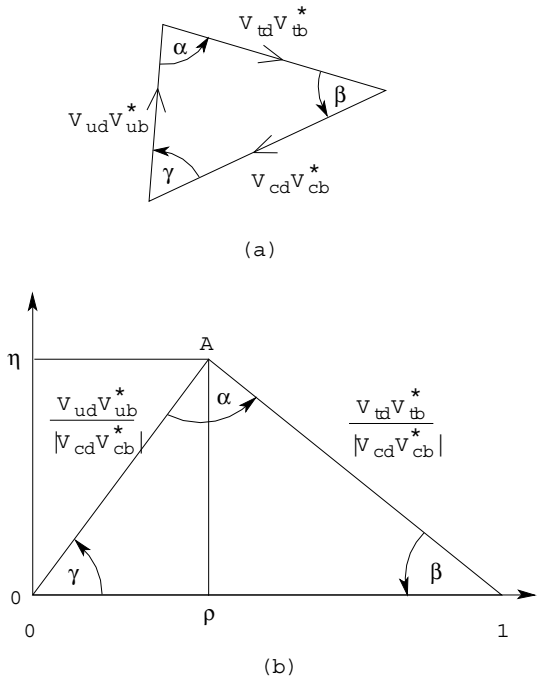

Figure 1.2: untitarity triangle for the B_u system obtained dividing each side by $|V_{cd}V_{cb}^*|$.

CP eigenstates, namely under a *CP* transformation they would transform into themselves with a definite eigenvalue ± 1. But since *CP* is not a good symmetry, the mass eigenstates can be different from *CP* eigenstates.

In addition in the *BABAR* experiment neutral B mesons are produced from the $\Upsilon(4S)$ resonance in a coherent flavor state

$$|\Psi_{fl}\rangle = |B^0\rangle|\overline{B}^0\rangle - |\overline{B}^0\rangle|B^0\rangle \tag{1.6}$$

The produced mesons evolve together in this state until one of them decays. The other one then starts evolving and it can decay as a B or a $\bar{B}$ depending on the time elapsed between the two decays. The mass eigenstates in fact are not flavor eigenstates, and so the flavor eigenstates are mixed with one another as they propagate through space.

In the following we will discuss the evolution of the initial B^0 ($\overline{B}^0$) state. The formalism applies to both B systems, and a similar notation can be used also for D^0 (or K^0) mesons. However, the two neutral K mesons have very different lifetimes (while their masses are almost identical), so that it

is more convenient to define the states by the mean-life, K_L and K_S for the long-lived and short-lived state, respectively. For the neutral D mesons, the mixing rate is much slower than the decay rate so that flavor eigenstates are the most convenient basis.

An arbitrary linear combination of the neutral B-meson flavor eigenstates ,

$$a|B^0\rangle + b|\bar{B}^0\rangle, \tag{1.7}$$

is governed by a time-dependent Schrödinger equation

$$i\frac{d}{dt}\begin{pmatrix} a \\ b \end{pmatrix} = H\begin{pmatrix} a \\ b \end{pmatrix} \equiv (M - \frac{i}{2}\Gamma)\begin{pmatrix} a \\ b \end{pmatrix} \tag{1.8}$$

for which M and Γ are 2×2 Hermitian matrices. CPT invariance guarantees $H_{11} = H_{22}$.

The light B_L and heavy B_H mass eigenstates are given by

$$|B_L\rangle = \ p|B^0\rangle + q|\bar{B}^0\rangle, \tag{1.9}$$

$$|B_H\rangle = \ p|B^0\rangle - q|\bar{B}^0\rangle. \tag{1.10}$$

The complex coefficients p and q obey the normalization condition

$$|q|^2 + |p|^2 = 1. \tag{1.11}$$

Note that $\arg(q/p^*)$ is just an overall common phase for $|B_L\rangle$ and $|B_H\rangle$ and has no physical significance.

The mass difference Δm_B and width difference $\Delta\Gamma_B$ between the neutral B mesons are defined as follows:

$$\Delta m_B \equiv M_H - M_L, \ \Delta\Gamma_B \equiv \Gamma_H - \Gamma_L, \tag{1.12}$$

so that Δm_B is positive by definition. Finding the eigenvalues of (1.8), one gets

$$(\Delta m_B)^2 - \frac{1}{4}(\Delta\Gamma_B)^2 = 4(|M_{12}|^2 - \frac{1}{4}|\Gamma_{12}|^2), \tag{1.13}$$

$$\Delta m_B \Delta\Gamma_B = 4\mathcal{R}e(M_{12}\Gamma_{12}^*). \tag{1.14}$$

The ratio q/p is given by

$$\frac{q}{p} = -\frac{\Delta m_B - \frac{i}{2}\Delta\Gamma_B}{2(M_{12} - \frac{i}{2}\Gamma_{12})} = -\frac{2(M_{12}^* - \frac{i}{2}\Gamma_{12}^*)}{\Delta m_B - \frac{i}{2}\Delta\Gamma_B}, \tag{1.15}$$

and finally the evolved state of initial B^0 ($\overline{B}^0$) meson denoted as $|B^0_{\rm phys}\rangle$ is

$$|B^0_{\rm phys}(t)\rangle = g_+(t)|B^0\rangle + (q/p)g_-(t)|\bar{B}^0\rangle, \tag{1.16}$$

$$|\bar{B}^0_{\rm phys}(t)\rangle = (p/q)g_-(t)|B^0\rangle + g_+(t)|\bar{B}^0\rangle, \tag{1.17}$$

where

$$g_+(t) = e^{-iMt}e^{-\Gamma t/2}\cos(\Delta m_B t/2), \tag{1.18}$$

$$g_-(t) = e^{-iMt}e^{-\Gamma t/2} i\sin(\Delta m_B t/2), \tag{1.19}$$

Kaon experiments can easily separate the mass eigenstates and investigate K_L and K_S decays independently because of the large lifetime difference between the neutral kaons. This is impossible in B and D experiments so there one will follow the decays of $B^0_{\rm phys}(t)$ and $\bar{B}^0_{\rm phys}(t)$ instead.

1.1.5 Three types of *CP* violation

The types of *CP* violation can be divided in three different categories on the basis of the mechanism that generates the violation.

In the interference between the decays with and without mixing

Consider now the decay of B mesons in final *CP* eigenstates. The final states are accessible both to B^0 and $\overline{B}^0$. *CP* asymmetry can be observed comparing the decay rate of a B^0 at the time t with the rate of the $\overline{B}^0$. The time t is the time elapsed between the two decays. Since the $\Upsilon(4S)$ is a spin 1 particle the $B^0\overline{B}^0$ evolve coherently in a L=1 state until one of the two decays. If the decay identifies its b-flavor (called *tag* decay) the other one starts evolving (or has evolved) as the opposite flavored B. Because of the mixing and the fact that the final state is accessible to both B^0 and $\overline{B}^0$ we can have a decay of two B^0 mesons of the same flavor. The interference between the amplitude with mixing and the one without mixing generates *CP* violation.

It can be measured considering the rate asymmetry of the decay of the $B^0(t)$ and $\overline{B}^0(t)$ as a function of t.

$$\alpha_{f_{CP}} = \frac{\Gamma(B^0(t)\to f_{CP}) - \Gamma(\overline{B}^0(t)\to f_{CP})}{\Gamma(B^0(t)\to f_{CP}) + \Gamma(\overline{B}^0(t)\to f_{CP})} \tag{1.20}$$

where $\lambda_{f_{CP}} = \frac{q}{p}\frac{\bar{A}_{f_{CP}}}{A_{f_{CP}}}$.

The above asymmetry can be expressed as

$$a_{f_{CP}} = \frac{(1-|\lambda_{f_{CP}}|^2)\cos(\Delta m_B t) - 2\mathcal{I}m\lambda_{f_{CP}}\sin(\Delta m_B t)}{1+|\lambda_{f_{CP}}|^2}. \tag{1.21}$$

The *CP* violation occurs when $\lambda \neq \pm 1$. In the clean modes (such a as $B^0 \to J/\psi K_S^0$) however $|\lambda| = 1$ and the expression above simplifies to

$$a_{f_{CP}} = -\mathcal{I}m\lambda_{f_{CP}}\sin(\Delta m_B t). \tag{1.22}$$

If there is only two amplitudes interfering and there are no hadronic uncertainties the phase of λ can easily be expressed in terms of the CKM matrix parameters.

For the Class 1 decay $B^0 \to J/\psi K_S^0$ the quark subprocess $b \to c\bar{c}s$ which is dominated by the W-mediated tree diagram[1]:

$$\frac{\bar{A}_{\psi K_S}}{A_{\psi K_S}} = \eta_{\psi K_S}\left(\frac{V_{cb}V_{cs}^*}{V_{cb}^*V_{cs}}\right)\left(\frac{V_{cs}V_{cd}^*}{V_{cs}^*V_{cd}}\right)e^{-2i\xi_B}. \tag{1.23}$$

The *CP* eigenvalue of the state is $\eta_{\psi K_S} = -1$. Taking into account also the $K-\bar{K}$ mixing[2] one finds

$$\lambda(B\to\psi K_S) = -\left(\frac{V_{tb}^*V_{td}}{V_{tb}V_{td}^*}\right)\left(\frac{V_{cb}V_{cs}^*}{V_{cb}^*V_{cs}}\right)\left(\frac{V_{cs}^*V_{cb}}{V_{cs}V_{cb}^*}\right) \Longrightarrow \mathcal{I}m\lambda_{\psi K_S} = \sin(2\beta). \tag{1.24}$$

For this decay th hadronic uncertainty is of $\mathcal{O}(10^{-3})$. This measurement will thus give the theoretically cleanest determination of a CKM parameter, even cleaner than the determination of $\sin\theta_C$ from $K \to \pi\ell\nu$.

Another interesting example is $B \to \pi\pi$. The quark subprocess is $b \to u\bar{u}d$ which is dominated by the W-mediated tree diagram. Neglecting for the moment the second, pure penguin, in the amplitude one finds

$$\frac{\bar{A}_{\pi\pi}}{A_{\pi\pi}} = \eta_{\pi\pi}\frac{V_{ub}V_{ud}^*}{V_{ub}^*V_{ud}}e^{-2i\xi_B}. \tag{1.25}$$

The *CP* eigenvalue for two pions is $+1$ and thus we find

$$\lambda(B\to\pi^+\pi^-) = \left(\frac{V_{tb}^*V_{td}}{V_{tb}V_{td}^*}\right)\left(\frac{V_{ud}^*V_{ub}}{V_{ud}V_{ub}^*}\right) \Longrightarrow \mathcal{I}m\lambda_{\pi\pi} = \sin(2\alpha). \tag{1.26}$$

[1] $2\xi_B$ is the *CP* opearator phase of the B^0 meson

[2] $K-\bar{K}$ mixing is essential because $B^0 \to K^0$ and $\bar{B}^0 \to \bar{K}^0$, and interference is possible only due to $K-\bar{K}$ mixing

The pure penguin term in the decay amplitude has a weak phase, $\arg(V_{td}^* V_{tb})$, different from the term with the tree contribution, so it modifies both $\mathcal{I}m\lambda$ and (if there are non-trivial strong phases) $|\lambda|$. Recent results from CLEO suggest that the $B \to K\pi$ rate is comparable to or larger than the $B \to \pi\pi$ rate. This in turn indicates that the penguin contribution to $B \to \pi\pi$ channel is significant, probably 10% or more. This then introduces *CP* violation in decay, unless the strong phases cancel (or are zero, as suggested by factorization arguments). The resulting hadronic uncertainty can be eliminated using isospin analysis [7]. This requires a measurement of the rates for the isospin-related channels $B^+ \to \pi^+\pi^0$ and $B^0 \to \pi^0\pi^0$ as well as the corresponding *CP* conjugate processes. The rate for $\pi^0\pi^0$ is expected to be small and the measurement is difficult, but even an upper bound on this rate can be used to limit the magnitude of hadronic uncertainties.

The analysis of $B \to D^+D^-$ proceeds along very similar lines. The quark subprocess here is $b \to c\bar{c}d$, and so the tree contribution gives

$$\lambda(B \to D^+D^-) = \eta_{D^+D^-} \left(\frac{V_{tb}^* V_{td}}{V_{tb} V_{td}^*}\right) \left(\frac{V_{cd}^* V_{cb}}{V_{cd} V_{cb}^*}\right) \Longrightarrow \mathcal{I}m\lambda_{DD} = -\sin(2\beta). \tag{1.27}$$

since $\eta_{D^+D^-} = +1$. Again, there are hadronic uncertainties due to the pure penguin term in the decay amplitude, but they are estimated to be small.

CP violation in the decay

It occurs when the modulus of the amplitude for a process is different from the one for the *CP* conjugated.

Let us consider an initial state i that decay in a final state f trough two amplitudes, and its corresponding complex conjugate process. The amplitudes can be in general complex and the phases that appear can be of various origin. They can be for instance generated by the long distance strong interaction of the final state. Strong interaction is *CP* conserving so this *strong* phase (ξ) will be the same in $i \to f$ and $\overline{i} \to \overline{f}$. However the uneliminated phases in the coupling constants of the Lagrangian change sign for the *CP* conjugate process.

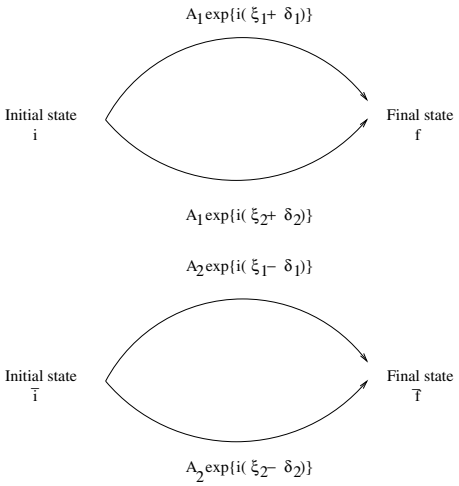

Figure 1.3: Direct *CP* violation

In the first case the interference gives a term $\cos((\xi_2 - \xi_1) + (\delta_2 - \delta_1))$ in the total amplitude

$$|A_{tot}|^2 = |A_1|^2 + |A_2|^2 + 2|A_1||A_2|\cos((\xi_2 - \xi_1) + (\delta_2 - \delta_1)) \tag{1.28}$$

while in the second case gives a term $\cos((\xi_2 - \xi_1) - (\delta_2 - \delta_1))$

$$|\bar{A}_{tot}|^2 = |A_1|^2 + |A_2|^2 + 2|A_1||A_2|\cos((\xi_2 - \xi_1) - (\delta_2 - \delta_1)) \tag{1.29}$$

Thus the total partial rate asymmetry results

$$\alpha_{dir} = \frac{\Gamma(i \to f) - \Gamma(\bar{i} \to \bar{f})}{\Gamma(i \to f) + \Gamma(\bar{i} \to \bar{f})} = \frac{-2|A_1|A_2|\sin(\xi_2 - \xi_1)\sin(\delta_2 - \delta_1)}{|A_1|^2 + |A_2|^2 + 2|A_1 A_2|\cos(\xi_2 - \xi_1)\cos(\delta_2 - \delta_1)} \tag{1.30}$$

We note from this that in order to have an asymmetry two phases are needed in the decay amplitude, one even under the *CP* operation, one odd.

CP violation in mixing

A second quantity that is independent of phase conventions and physically meaningful is

$$\left|\frac{q}{p}\right|^2 = \left|\frac{M_{12}^* - \frac{i}{2}\Gamma_{12}^*}{M_{12} - \frac{i}{2}\Gamma_{12}}\right|. \tag{1.31}$$

When *CP* is conserved, the mass eigenstates must be *CP* eigenstates. In that case $\left|\frac{q}{p}\right|^2 = 1$ and the relative phase between M_{12} and Γ_{12} vanishes.

Therefore

$$|q/p| \neq 1 \Longrightarrow CP\text{violation}. \tag{1.32}$$

This type of *CP* violation is here called *CP violation in mixing*; it is often referred to as *indirect CP violation* because it results from the mass eigenstates being different from the *CP* eigenstates.

For the neutral B system, this effect could be observed through the asymmetries in semi-leptonic decays:

$$a_{\rm sl} = \frac{\Gamma(\bar{B}^0_{\rm phys}(t) \to \ell^+\nu X) - \Gamma(B^0_{\rm phys}(t) \to \ell^-\nu X)}{\Gamma(\bar{B}^0_{\rm phys}(t) \to \ell^+\nu X) + \Gamma(B^0_{\rm phys}(t) \to \ell^-\nu X)}. \tag{1.33}$$

In terms of $|q/p|$,

$$a_{\rm sl} = \frac{1 - |q/p|^4}{1 + |q/p|^4}, \tag{1.34}$$

Effects of *CP* violation in mixing in neutral B_d decays, such as the asymmetries in semi-leptonic decays, are expected to be small, $\mathcal{O}(10^{-2})$. Moreover, to calculate the deviation of q/p from a pure phase, one needs to calculate Γ_{12} and M_{12}. This involves large hadronic uncertainties, in particular in the hadronization models for Γ_{12}. The overall uncertainty is easily a factor of 2–3 in $|q/p| - 1$. Thus even if such asymmetries are observed, it will be difficult to relate their rates to fundamental CKM parameters.

1.1.6 Comparisons with K and D system

To compare the effects of *CP* violation in mixing, note that $|q/p|_K$ and $|q/p|_{B_d}$ are both very close to 1. *CP* violation in mixing is then small in both systems. However, while for the B_d system the reason for that is the small lifetime difference ($\frac{\Delta\Gamma_B}{\Gamma_B} \sim 10^{-2}$, $\frac{\Delta M_B}{\Gamma_B} \sim 0.7$,), in the K system the reason is the smallness of the relevant *CP*-violating phase ($arg(M_{12}) - arg(\Gamma_{12}) \sim 10^{-3}$) . In the D sector instead the standard model short distance prediction for $\Delta M/\Gamma$, $\Delta\Gamma/2\Gamma$ is insignificant due to the GIM suppression mechanism and to the smallness of the relevant CKM matrix elements. Inclusion of long distance contribution can lead to values as low as $10^{-4} - 10^{-3}$ and soft GIM suppression in OPE [9] can achieve values of $\mathcal{O}(10^{-3})$. Even a very conservative SM prediction leads to a a value less than 0.01. Mixing and CP violation predictions are thus both small so this is a clean field to look for new physics contributions.

1.2 Charm lifetimes

BABAR is namely a B factory but is indirectly also a charm (and τ) factory. Charmed mesons are produced either in the decay of the B meson or from the $c\overline{c}$ continuum. In the latter case the cross section $e^+e^- \to c\overline{c}$ is about 1.3 nb leading to 2.6 million charm decays per fb^{-1}. In B decays the number of charm mesons per $B\overline{B}$ is about 1.2 that combined with a cross section $e^+e^- \to b\overline{b}$ of 1.05 nb gives another 2.6 million charm decays per fb^{-1}.

This huge number of charmed mesons allow precision measurements in the charm sector and in particular of lifetimes. This is an important point for *BABAR* because a precise measurement the decay length leads to a more complete understanding of the systematics related with the measurement of the vertex distance in *BABAR*.

From an engineering point of view the lifetime (or equivalently the total width) is needed to extract partial widths from branching ratio measurements. From a theoretical point of view instead, this is a test of the models that predict the lifetime a heavy hadron. These calculations based on the fundamental constituents quarks and gluons try to factorize the short distance contribution from the long distance one, which is usually the main engine that generates lifetime differences in hadrons with the same flavor. Since the differences depend on $1/m_Q^3$ they are reduced in B mesons but are more evident in the D mesons.

In addition $D^0\overline{D}^0$ mixing and CP violation effects are predicted to be extremely small in standard model calculations and a positive observation would be a hint of some underlying new physics.

1.2.1 Spectator quark decay model

Heavy hadrons, such as B, D (and K) can decay in many ways, pure leptonic modes ($D^+ \to \mu^+\nu_\mu$, $B^+ \to \tau^+\nu_\tau$), semi leptonic modes ($D \to Kl\nu$, $B \to D^*l\nu$) or non leptonic modes

$$\Gamma_{tot} = \Gamma_{PL} + \Gamma_{SL} + \Gamma_{NL} \tag{1.35}$$

The simplest picture of the semi leptonic and hadronic decay process is the spectator quark model in which the heavy quark is treated as a free

particle. In the perturbative calculation (and from dimensional considerations) the total width turns out to be proportional to the fifth power of the free quark mass m_Q

$$\frac{1}{\tau} = \Gamma \propto G_F^2 m_Q^5 \tag{1.36}$$

The lifetime value can be obtained rescaling the τ (μ) lifetime by the factor (m_Q/m_τ) obtaining for charmed hadrons a single lifetime of

$$\tau_c \sim \tau_\tau / \left(m_c/m_\tau\right)^5 = 291\ fs / \left(1.5/1.77\right)^5 \sim 700 fs$$
$$\tau_c \sim \tfrac{1}{5}\tau_\mu / \left(m_c/m_\mu\right)^5 = 2.19\ \mu s / \left(1.5/0.105\right)^5 \sim 700 fs$$

However for heavy hadrons the lifetimes of the particles with same flavor are not at all the same:

$$\tau(K^+)/\tau(K_s) \sim 140, \quad \tau(D^+)/\tau(D^0) \sim 2.5, \quad \tau(B+)/\tau(B0) \sim 1.06$$

How to explain these differences?
The solution to this has been to take into account the effects of the light valence quark(s) and has lead to cope with non perturbative QCD corrections and to develop the operator product expansion (OPE) technology [8].

Lifetime differences

In the charm case the lifetime of mesons and baryons spans from the lifetime of the D^+ (the longest) to one of the Ω_c (the shortest) with a difference of one order of magnitude, as reported in tab. 1.1.

Particle	lifetime [PDG]	quark content
D^+	$1050 \pm 13\ fs$	$c\bar{d}$
D_s^+	$496 \pm 10\ fs$	$c\bar{s}$
D^0	$412 \pm 3\ fs$	$c\bar{u}$
Ξ_c^+	$330 \pm 50\ fs$	usc
Λ_c^+	$206 \pm 12\ fs$	udc
Ξ_c^0	$98 \pm 20\ fs$	dsc
Ω_c	$64 \pm 20\ fs$	ssc

Table 1.1: Summary of the wide range of lifetimes of charmed hadrons

Let us consider the particularly interesting case of the difference between D^0 and D^+.

The QCD graphs that contributes to the decays shown in figure 1.4 are the spectator decay, the internal spectator and the W-exchange and the W-annihilation (and any interference between them). Purely leptonic modes in eq. 1.35 are helicity suppressed due to the $V-A$ coupling of the W bosons to the left handed fermions [3], the semi-leptonic width of D^0 and D^+ are equal at the 10% level. The lifetime difference originates in the non leptonic modes, due to the influence of the light quark.

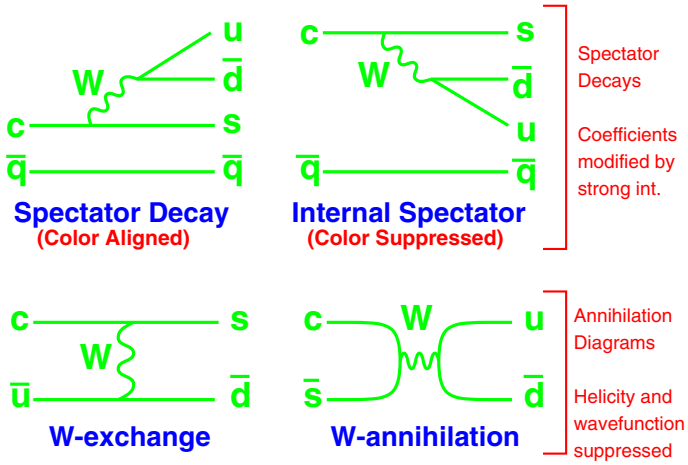

Figure 1.4: Hadronic decay diagrams for charm meson decays

To be noted the presence of two identical anti-quarks in the final state of the D^+ decay: $(c\bar{d}) \to (s\bar{d}u)\bar{d}$. The internal and the external spectator decay lead to the same final state allowing for an interference of the two amplitudes. This is often called Pauli Interference (PI) because is generated by the presence of two identical fermions in the final state. The computations show that this interference is destructive, leading to a smaller hadronic width for the D^+ and explaining (at least qualitatively) the lifetime difference.

It is also possible to understand qualitatively how the presence of two identical quarks in the final state generates smaller width for the D^+.

Let us consider the spectator quark model for the decay of the charm meson. The leading hadronic diagram of the charm quark is the tree transi-

[3] $D^+ \to \tau^+\nu_\tau$ is suppressed for a phase space factor

tion $c \to su\bar{d}$. In the case of D^0 it is accompanied by a $\bar{u}$ quark while in the case of the D^+ it is accompanied by a $\bar{d}$ quark leading to the two identical $\bar{d}\bar{d}$ quarks in the final state.

Let us consider the final state $|su\bar{d}\bar{d}\rangle$. We can separate the Hilbert space in the direct product of the Hilbert spaces of two quarks states of $|su\rangle$ and $|\bar{d},\bar{d}\rangle$:

$$|s,u,\bar{d},\bar{d}\rangle = |s,u\rangle \otimes |\bar{d},\bar{d}\rangle \tag{1.37}$$

The two identical $\bar{d}$ quarks in the final state have to be in a completely antisymmetric state because of the Fermi statistic. When the decay happen with zero orbital angular momentum ($L_{tot} = L_{su} = L_{\bar{d}\bar{d}} = 0$) two $\bar{d}$ quarks spin state must be a spin singlet:

$$|\bar{d},\bar{d}\rangle = \frac{|+1/2,-1/2\rangle - |-1/2,+1/2\rangle}{\sqrt{2}}. \tag{1.38}$$

The decay amplitude is thus the sum of two pieces

$$\begin{aligned} A &= \langle c,\bar{d}| \left(|s,u\rangle \otimes \frac{|+1/2,-1/2\rangle - |-1/2,+1/2\rangle}{\sqrt{2}} \right) \\ &= \left(\frac{\langle c,\bar{d}| \left(|s,u\rangle \otimes |+1/2,-1/2\rangle \right)}{\sqrt{2}} - \frac{\langle c,\bar{d}| \left(|s,u\rangle \otimes |-1/2,+1/2\rangle \right)}{\sqrt{2}} \right) \\ &= A_1 - A_2 \end{aligned} \tag{1.39}$$

Since the total momentum J is zero and the orbital angular momentum and the spin of $\bar{d}\bar{d}$ system is zero the su system is constrained to have zero spin, hence su need to be in a singlet state. Also the initial state $|c\bar{u}\rangle$ need to be in a singlet state because for the D^0 $J = 0$, $P = -1$. We note now that a spin singlet state has negative parity $P(|c\bar{d}\rangle = -|c\bar{d}\rangle, P|su\rangle = -|su\rangle$.

We introduce between the initial and final state the identity $1 = P^+P$

$$\begin{aligned} A_1 &= \langle c,\bar{d}|1 \left(|s,u\rangle \otimes |+1/2,-1/2\rangle \right) \\ &= \langle c,\bar{d}|P^+P \left(|s,u\rangle \otimes |+1/2,-1/2\rangle \right) \\ &= \langle c,\bar{d}| \left(|s,u\rangle \otimes |-1/2,+1/2\rangle \right) = A_2 \end{aligned}$$

and hence the amplitude $A = A_1 - A_2$ cancels. However this apply only for orbital momentum equal to zero so higher orbital momentum amplitudes are allowed.

However we should note that the Cabibbo allowed W-exchange diagram could contribute only to the D^0 width and can in principle lower its lifetime

but this is again suppressed for the helicity argument and for the "wave-function overlap" factor f_D ($\sim |f_D|^2 m_s^2/m_c^4 \sim 10^{-3}$) leading to a negligible contribution.

1.2.2 OPE theoretical framework

The theoretical framework that allows the quantitative treatment of non perturbative QCD effects in heavy hadrons decays is based on the Operator Product Expansion (OPE) technology. This technology consists basically in the expansion of the decay amplitude in powers of $1/m_Q$ where m_Q is the mass of the heavy quark, and the separation of perturbative effects (numerical coefficients) from non perturbative ones (hadronic matrix elements).

The effective weak Lagrangian for the decay [11]

$$\mathcal{L}_W = \frac{4G_F}{\sqrt{2}} \left(c_1 \mathcal{O}_1 + c_2 \mathcal{O}_2\right) \tag{1.40}$$

takes into account the coupling between the free quark currents $\bar{\psi}\Gamma_\mu\psi$

$$\mathcal{O}_1 = (\bar{s}\Gamma_\mu c)(\bar{u}\Gamma^\mu d),\ \mathcal{O}_2 = (\bar{s}_i\Gamma_\mu c^j)(\bar{u}_j\Gamma^\mu d_i) \tag{1.41}$$

where $\Gamma_\mu = \gamma_\mu \frac{(1-\gamma_5)}{2}$, $c_1 \sim 1.3$ and $c_2 =\sim -0.5$ are known from perturbation theory [12] and basically incorporates the short distance effects.

The total width for the decay can be computed from the forward scattering amplitude for the H_c hadron using the optical theorem [13]

$$\begin{aligned} S &= 1 - iT2\pi\delta(E - E') \\ \Gamma_{H_c}\langle H_c|H_c\rangle &= -2\mathcal{I}m\langle H_c|T|H_c\rangle \end{aligned} \tag{1.42}$$

The S matrix expansion evaluated at the second order in $\mathcal{L}_W$ permits to construct the forward scattering amplitude for T:

$$-\frac{2\mathcal{I}m\langle H_c|T|H_c\rangle}{\langle H_c|H_c\rangle} = \frac{\mathcal{I}m\int d^4x\langle H_c|\{\mathcal{L}_W(x)\mathcal{L}_W(0)\}_T|H_c\rangle}{2M_{H_c}} \tag{1.43}$$

The second term in 1.43 can be expanded [8] in a sum of hadronic matrix elements of local operators $\mathcal{Q}_i$ of dimension i (i.e. $\mathcal{Q}_i \sim m^i$). Since[4] the dimension of the matrix element is $\frac{\langle H_c|\mathcal{Q}_i|H_c\rangle}{2M_{H_c}} = \frac{\langle 0|b_p\mathcal{Q}_i b_q^+|0\rangle}{2M_{H_c}} \sim m^{i-3}$ the

[4] with the normalization of creation operators $[b_p, b_q^+] = 2\pi^3 2p^0\delta^3(p-q)$

expansion turns out to be an expansion in inverse powers of the quark mass m_c

$$\Gamma_{(H_Q \to f)} = \frac{G_F^2 |V_{CKM}|^2 m_c^5}{192\pi^3} \sum_i c_i^{(f)} \frac{\langle H_c | \mathcal{Q}_i | H_c \rangle}{2M_{H_c} m_c^{i-3}} \tag{1.44}$$

where c_i are c-numbers. The leading terms can be found explicitating the operators $\mathcal{Q}_i$ to the the $1/(m_c)^4$ order. For semi-leptonic and non leptonic decays it takes the following form:

$$\begin{aligned} \Gamma_{(H_c \to f)} = \; & \frac{G_F^2 |V_{CKM}|^2 m_c^5}{192\pi^3} \left[c_3^{(f)} \frac{\langle H_c | \bar{c} c | H_c \rangle}{2M_{H_c}} + c_5^{(f)} \frac{\langle H_c | \bar{c} i\sigma G Q | H_c \rangle}{2M_{H_c} m_c^2} + \right. \\ & \left. \sum_i c_6^{(f)} \frac{\langle H_c | (\bar{c}\Gamma_i q)(\bar{q}\Gamma_i c) | H_c \rangle}{2M_{H_c} m_c^3} + \mathcal{O}(1/m_c^4) \right] \end{aligned} \tag{1.45}$$

where c is the field operator for the heavy quark, σ is the spin, G is the gluonic field, $\Gamma_i = \gamma_i \frac{(1-\gamma_5)}{2}$, and q is the field operator of the light quark. In this equation we should note:

- The $c_i^{(f)}$ coefficient are c-numbers that incorporate the short distance physics and are computed using perturbation theory.
- The hadronic matrix elements take into account the contribution from long distance physics (soft QCD).
- It can be shown that $\frac{1}{2M_{H_c}} \langle H_c | \bar{c} c | H_c \rangle = \frac{m_c}{E_c} = 1 + \mathcal{O}\left(\frac{1}{m_c^2}\right)$ so in the limit $m_c \to \infty$ the total width has the m_c^5 behavior according with the free quark model. The second and third term represent thus the preasimptotic corrections.
- The first term that generates lifetime differences within same flavor hadrons is of order $1/(m_c^2)$. In addition This correction depends upon the spin and thus generates differences between pseudo-scalar mesons and baryons.
- The third term $\mathcal{O}(1/m_c^3)$ generates instead difference that depends on the light quark and thus generates differences within mesons.

In the particular case of the D^+ lifetime the additional diagrams due to the presence of two identical quarks in the final state can be computed and lead to the destructive interference. However the prediction is value around

2 with a big error. The present measurements [PDG] give a value of about 2.5.

The situation is even worse if we compare the D^0 lifetime with the D_s lifetime. Present measurements definitely show that D_s lifetime is greater than D^0 lifetime $\tau(D_s)/\tau(D^0) = 1.211 \pm 0.017$ but the calculations lead to values only a few % different from 1. Higher values can be obtained including a big effect of the W-exchange diagrams, that on the other hand are not found in the exclusive decays.

The present level of prediction of the theory is far from being satisfactory but the the predicted hierarchy of the lifetimes is correct. However precision measurements of lifetimes and other quantities can lead to a better understanding of the theoretical models.

1.3 D^0 $\overline{D}^0$ mixing and new physics

Mixing between D^0 and $\overline{D}^0$ mesons is not allowed at the tree level in the S.M. and can be treated with the same formalism that we have used for B and K mesons. Note also that in this case only down quarks contribute to the box diagram 1.5. In the D sector however not only $\Delta\Gamma \ll \Gamma$ but also $\Delta M \ll \Gamma$ with the present experimental limits.

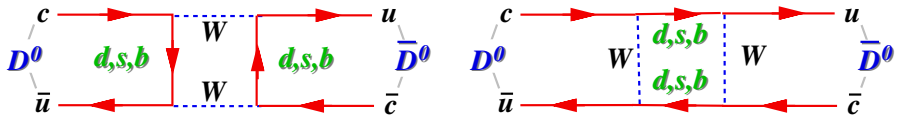

Figure 1.5: The two box diagram for mixing.
sample

In addition the Standard Model predictions are so small that a "big" mixing can be a sharp indication of new underlying physics. The smallness of the mixing rate is due to the GIM [16] suppression and the smallness of the relevant CKM matrix elements. Consider the box diagrams that represent the lowest order short distance contribution to the D mixing (fig. 1.5), the mixing amplitude calculated from these diagrams is proportional to the appropriate CKM matrix factors and to a loop integral that depends upon

the quark masses in the loop [17]

$$\langle \overline{D}^0 | H | D^0 \rangle \propto \sum_{i,j=d,s,b} V_{ci}^* V_{ui} V_{cj} V_{uj}^* S(m_i, m_j) \tag{1.46}$$

If the quark masses are identical all the loop integrals $S(m_i, m_j)$ are equal and the amplitude cancels because of the unitarity of the CKM matrix. If the mass differences are small the GIM mechanism suppresses the mixing. For the charm sector the b quark contribution in the loop is insignificant because the CKM factor is $\sim \sin\theta_c^5$ suppressed relative to the factors $V_{cd}^* V_{ud}$ and $V_{cs}^* V_{us}$. Since d-s mass difference is relatively small the mixing rate results in the $10^{-9} - 10^{-10}$ range [9] Long distance contributions, more difficult to compute, can achieve values around [9] 10^{-6}.

If there is new physics such as fourth generation of quarks, leptoquars etc. they can contribute to the box diagram and thus to ΔM. Because the SM prediction is so small there is a large window to see the effect of such a new physics, unhidden by the SM effects.

1.3.1 Charm mixing in DCS decays

Let us consider an initial D^0 meson whose flavor can be determined from the sign of the bachelor pion in the $D^{*+} \to D^0 \pi^+$ decay. Some final states (such as $K^+\pi^-$) can be obtained either directly via a doubly Cabibbo suppressed decay $D^0 \to K^+\pi^-$ (amplitude A) or via oscillation $D^0 \overline{D}^0$ and a subsequent decay $\overline{D}^0 \to K^+\pi^-$ (amplitude $\bar{A}$). Following the same formalism that we have used for the B mesons in section 1.1.4 we can find the mixing rate

$$r_{mix}(t) = \left| \langle \overline{D}^0 | D^0(t) \rangle \right|^2 = \frac{1}{4} e^{-\Gamma t} \left| \frac{q}{p} \right|^2 \left(\Delta M^2 + \frac{1}{4} \Delta\Gamma^2 \right) t^2 \tag{1.47}$$

which has been expanded as a function of the small parameter $\Delta M t$ since $\Delta M \ll \Gamma$. Integrating over t we find the mixing rate for the D^0

$$r_{mix} = \frac{1}{2} \left| \frac{q}{p} \right|^2 \left[\left(\frac{\Delta M}{\Gamma} \right)^2 + \left(\frac{\Delta\Gamma}{4\Gamma} \right)^2 \right] \tag{1.48}$$

which is unfortunately very small in the standard model $r_{mix} \leq 10^{-8}$. Since the doubly Cabibbo suppressed decay is suppressed by a factor $\sim \tan\theta_c^4 \sim 3 \times 10^{-3}$ the interference with a mixing of the same order of magnitude can

be revealed in the proper time distribution of the decay. The decay rate of an initial D^0 meson to the $K^+\pi^-$ final state (called "wrong sign") is

$$\begin{aligned} r_{ws}(t) &= \left|\langle D^0|K^+\pi^-\rangle\right|^2 \\ &= e^{-t}\left|A\cos\left(\frac{\Delta M}{\Gamma}-i\frac{\Delta\Gamma}{2\Gamma}\right)\frac{t}{2}+\bar{A}\frac{q}{p}i\sin\left(\frac{\Delta M}{\Gamma}-i\frac{\Delta\Gamma}{2\Gamma}\right)\frac{t}{2}\right|^2 \end{aligned} \tag{1.49}$$

where the time t is now measured in units of τ_{D^0} for convenience. Defining $\lambda_D = \frac{Ap}{Aq}$ and expanding in powers of the small parameters $\frac{\Delta M}{\Gamma}t$ and $\frac{\Delta\Gamma}{2\Gamma}t$ we obtain for the proper time distribution

$$r_{ws}(t) = e^{-t}\left|\bar{A}\right|^2\left[\frac{A}{\bar{A}}+\frac{r_{mix}}{2}t^2+\left|\frac{q}{p}\right|^2\left(\frac{\Delta\Gamma}{2\Gamma}\mathcal{R}e(\lambda_D)+\frac{\Delta M}{\Gamma}\mathcal{I}m(\lambda_D)\right)t\right] \tag{1.50}$$

If we assume that CP is an exact symmetry then $\frac{q}{p}=1$ and $\lambda_D = \lambda_{\bar{D}} = \sqrt{R_{DCS}}\,e^{i\delta}$. We can also redefine x, y for a rotation of $\delta = \arg\lambda_D$

$$y' = \frac{\Delta\Gamma}{2\Gamma}\cos\delta+\frac{\Delta M}{\Gamma}\sin\delta,\ x' = -\frac{\Delta\Gamma}{2\Gamma}\sin\delta+\frac{\Delta M}{\Gamma}\cos\delta \tag{1.51}$$

and we obtain a simple expression for the distribution of the "wrong sign" decay proper time distribution

$$r_{ws}(t) = e^{-t}\left|\bar{A}\right|^2\left[R_{DCS}+\frac{r_{mix}}{2}t^2+y'\sqrt{R_{DCS}}t\right] \tag{1.52}$$

We note in equation 1.52 that the DCS term has no time dependence, while the mixing term has a t^2 dependence and the interference term is proportional to t. If δ is small, as has been argued in [14], [15], then $y' = \frac{\Delta\Gamma}{2\Gamma}$. The $e^{-t}\left|\bar{A}\right|^2$ part of the distribution can be extracted from right sign decays while the parameters R_{DCS}, x', y' can extracted from the proper time distribution fit.

Chapter 2

BABAR Detector

2.1 Introduction

The PEP-II B Factory is an asymmetric e^+e^- collider designed to operate at a luminosity of 3×10^{33} cm^{-2}s^{-1} and beyond at a center-of-mass energy of 10.58 GeV, the mass of the $\Upsilon(4S)$ resonance. This resonance decays almost exclusively into $B\overline{B}$ or B^+B^- pairs and thus provides an ideal laboratory for the study of B mesons. In PEP-II, the electron beam of 9.0 GeV collides head-on with the positron beam of 3.1 GeV resulting in a boost to the $\Upsilon(4S)$ resonance of $\beta\gamma = 0.56$. This boost makes it possible to reconstruct the decay vertices of the two B mesons and to determine their relative decay times. One can therefore measure the decay time dependence of decay rates. The crucial test of CP invariance is a comparison of these rates for B^0 and $\overline{B}^0$ to a CP eigenstate. Experimentally this requires events in which one B meson decays to a CP eigenstate and is fully reconstructed and the other B meson is tagged as B^0 or a $\overline{B}^0$ by its decay products, a charged lepton, a charged kaon or a D* decay.

The very small branching ratios of B mesons to CP modes, typically 10^{-4}, and the need for full reconstruction of final states with two or more charged particles and several π^0 plus the tagging of the second B place stringent requirements on the detector:

Physics requirements

- a large and uniform acceptance, in particular down to small polar angles relative to the boost direction, to avoid particle losses;

- excellent detection efficiency for charged particles down to 60 MeV/c and for photons to 25 MeV;
- high momentum resolution to separate small signals from background;
- excellent energy and angular resolution for the detection of photons from π^0 and radiative B decays in the range from 25 MeV to 4 GeV;
- very good vertex resolution, both transverse and parallel to the beam;
- identification of electrons and muons over a range of momentum, primarily for the detection of semi-leptonic decays used to tag the B flavor and for the study of semi-leptonic and rare decays;
- identification of hadrons over a wide range of momentum for B flavor tagging as well as for the separation of pions from kaons in decay modes like $B^0 \to K^{\pm}\pi^{\mp}$ and $B^0 \to \pi^+\pi^-$ as well as in charm meson and τ decays;
- a highly efficient, selective trigger system with redundancy so as to avoid significant signal losses and systematic uncertainties;

Factory requirements

- low noise electronics and data acquisition systems of high flexibility and operational stability;
- high degree of reliability of components and frequent monitoring and automated calibrations, plus control of the environmental conditions to assure continuous and stable operation;
- an on-line computing and network system that can control, process, and store the expected high volume of data; and
- detector components that can tolerate significant doses of radiation and operate under high background condition.

To reach the desired sensitivity for the most interesting measurements, data sets of order 10^8 B mesons will be needed. For the peak cross section at the $\Upsilon(4S)$ of 1.2 nb this will require an integrated luminosity of order 100 fb^{-1} or three years of reliable and highly efficient operation of a detector

of state-of-the art capabilities at a storage ring operating with only few interruptions at design luminosity or above.

2.2 PEP-II

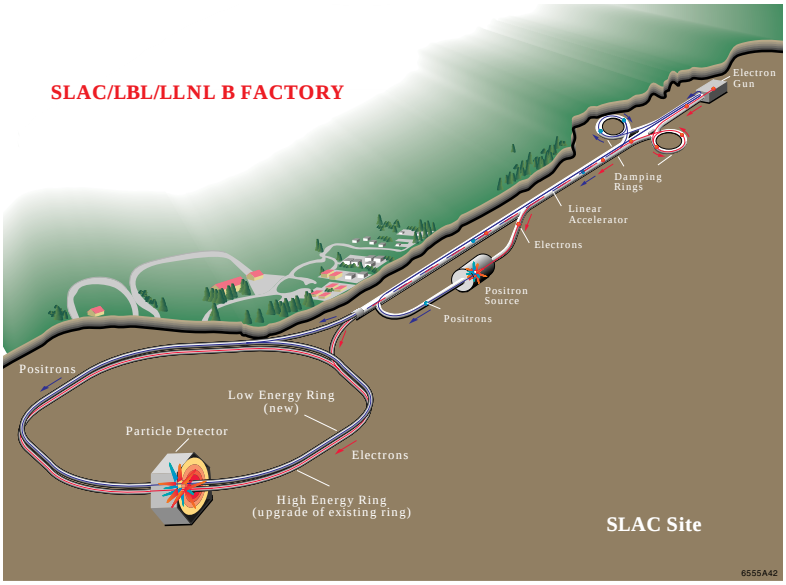

Figure 2.1: PEP-II overview

PEP-II is an e^+e^- storage ring system designed to operate at a center of mass energy of 10.58 GeV, corresponding to the mass of the $\Upsilon(4S)$ resonance. The parameters of these energy asymmetric storage rings are presented in table 2.1. PEP-II has surpassed its design luminosity, both in terms of the instantaneous and the integrated daily luminosity, with significantly fewer bunches than anticipated.

PEP-II typically operates in a series of 40 minute fills during which the colliding beams coast. At the end of each fill, it takes about three minutes to replenish the beams for the next fill. After a loss of the stored beams, it takes approximately 10-15 minutes to refill the two beams. *BABAR* divides the data into runs, defined as periods of three hour duration or less during which beam and detector conditions are judged to be stable. While most

Table 2.1: PEP-II beam parameters; values are given both for design and typical colliding beam operation in the first year. HER and LER refer to the high energy e^- and low energy e^+ ring, respectively. σ_{Lx}, σ_{Ly}, and σ_{Lz} refer to the horizontal, vertical, and longitudinal r.m.s size of the luminous region.

Parameters	Units	Design	Typical
Energy HER/LER	GeV	9.0/3.1	9.0/3.1
Current HER/LER	A	0.75/2.15	0.7/1.3
# of bunches		1658	553-829
Bunch spacing	ns	4.2	6.3-10.5
σ_{Lx}	μm	110	120
σ_{Ly}	μm	3.3	5.6
σ_{Lz}	mm	9	9
Luminosity	pb^{-1}/d	135	120

of the data are recorded at the peak of the $\Upsilon(4S)$ resonance, some 12% are taken at an energy 40 MeV below to allow for studies of the non-resonant background.

2.2.1 Interaction region

PEP-II collides the bunches head-on to avoid the coupling of transverse and longitudinal modes caused by the crossing angle at DORIS-I that limited its luminosity. The energy asymmetry makes it possible to separate the beams magnetically but is not possible to use different focusing optics for the two beams. The higher energy beam (HER) has indeed more focusing than the other with equal currents, that would result in an asymmetric focusing. To compensate this and obtain a symmetric focusing, the lower energy beam has been designed to have a higher current. It is usually more difficult [23] to obtain a high current electron beam w.r.t. a positron beam because the positive ions that remain in the beam pipe are attracted by the electron beam and can generate orbit instabilities. This is indeed the reason why the electron beam has been chosen to have the lower current (and the higher energy). However PEP-II experts [23] claim that with the present working conditions the positron beam (the one with higher current) becomes instable

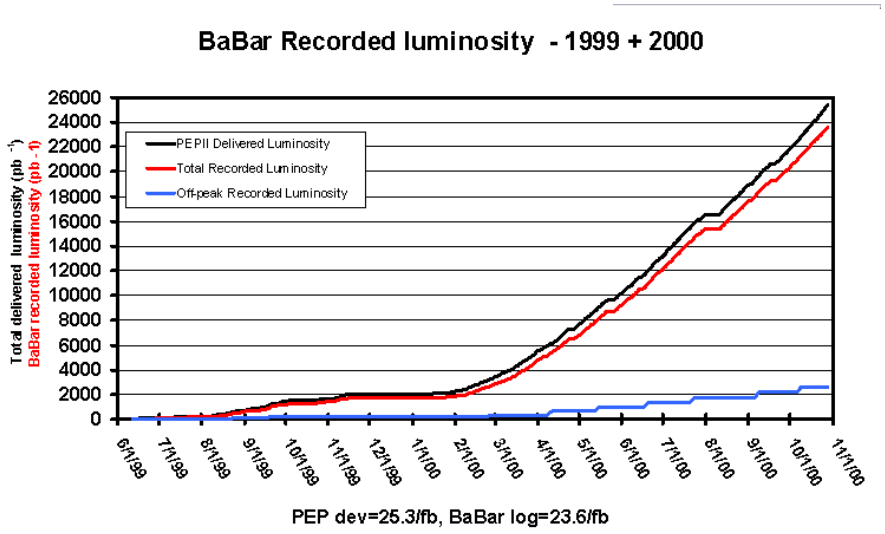

P

Figure 2.2: PEP-II-delivered and BaBar-recorded integrated luminosity in the 1999 and 2000 runs.

at high currents because of a multiplication effect of electrons extracted from the walls of the beam pipe

The large beam currents inherent to the high luminosity of PEP-II and the necessity to separate closely-spaced bunches as close as possible to the interaction point (I), tightly couple the issues of detector design, interaction region layout, and remediation of machine induced background. The bunches are separated magnetically in the horizontal plane by a pair of dipole magnets (B1), followed by a series of offset quadrupoles. The tapered B1 dipoles, located at $\pm$ 21 cm on either side of the IP, and the Q1 quadrupoles are made of samarium-cobalt and operate inside the field of the *BABAR* solenoid, while Q2, Q4, and Q5, located outside or in the fringe field of the solenoid, are standard iron magnets. The collision axis is off-set from the z-axis of the *BABAR* detector by about 20 mrad in the horizontal plane [18].

The interaction region is enclosed by a water-cooled beam pipe composed of two thin layers of beryllium (0.83 mm and 0.53 mm) with a 1.48- mm water channel in-between. To attenuate synchrotron radiation, the inner surface of the pipe is gold-plated (approximately 4 μm). In addition, the beam

pipe is wrapped with 150 μm Ta foil on either side of the IP, *i.e.,* beyond $z = +10.1$ cm and $z = -7.9$ cm. The total thickness of the central beam pipe section at normal incidence corresponds to 1.06% of a radiation length.

The beam pipe, the permanent magnets and the SVT are assembled and aligned and then enclosed in a 4.4-m long support tube. This rigid structure is inserted into the *BABAR* detector, spanning the IP. The central section of this tube is fabricated from carbon-fiber epoxy composite thus reducing the thickness to 1.08% of a radiation length.

2.2.2 Luminosity, Beam Energies and Position

The beam parameters that are most critical for the *BABAR* data analysis are the luminosity, the energies of the two beams and the position and size of the luminous region.

Luminosity

While PEP-II uses a high-rate luminosity monitor sampling radiative Bhabha scattering to provide a fast relative measurement of the luminosity for operations, *BABAR* derives the absolute luminosity off-line from QED processes. The best result is obtained from $\mu^+\mu^-$ pairs. For a sample of 1 fb^{-1}, the statistical error is 1.3%, compared to a systematic error of 0.5 % on the relative, and 1.5 % on the absolute value of the luminosity. This error is currently dominated by uncertainties in the Monte Carlo generator and the simulation of the detector. It is expected that with a better understanding of the efficiency the overall systematic error on the absolute value of the luminosity can be reduced by a factor two.

Beam Energies

During operation, the mean energies of the two beams are calculated from the total magnetic bending strength (including the effects of off-axis quadrupole fields, steering magnets, and wigglers) and the beam orbits. While the systematic uncertainty in the PEP-II calculation of the absolute beam energies is estimated to be $5 - 10$ MeV, the relative energy setting for each beam is accurate and stable to about 1 MeV. The energy spread of the LER and HER is 2.3 MeV and 5.5 MeV, respectively.

To ensure that data are recorded close to the peak of the $\Upsilon(4S)$ resonance, the observed ratio of $B\overline{B}$ enriched hadronic events to lepton pair production is monitored on-line. At the peak of the resonance, a 2.5% change in the $B\overline{B}$ production rate corresponds to a 2 MeV change in the c.m. energy, a value that is close to the tolerance to which the energy of PEP-II can be held. However, a drop in the $B\overline{B}$ rate does not distinguish between energy settings below or above $\Upsilon(4S)$ peak. The sign of the energy change must be determined from other indicators. The best monitor and absolute calibration of the c.m. energy is derived from the measured c.m. momentum of fully reconstructed B mesons combined with the known B meson mass. An absolute error of 1.1 MeV can be obtained for an integrated luminosity of 1 fb^{-1}. This error is equally limited by the knowledge of the B mass [19] and the detector resolution.

Beam Direction

The direction of the beams relative to *BABAR* is measured iteratively run-by-run using e^+e^- and $\mu^+\mu^-$ events. The resultant uncertainty in the direction of the boost from the laboratory to the c.m. frame, $\vec{\beta}$, is about 1 mrad, dominated by alignment errors. This translates into an uncertainty of about 0.3 MeV in the energy substituted mass. $\vec{\beta}$ is consistent to within 1 mrad with the orientation of the elongated beam spot (see below). It is stable to better than 1 mrad from one run to the next.

Beam Size and Position

The size and position of the luminous region are critical parameters for the decay-time-dependent analyses and their values are monitored continuously on-line and off-line. The design values for the size of the luminous region are presented in table 2.1 above. The vertical size is too small to be measured directly. It is inferred from the measured luminosity, the horizontal size, and the beam currents; it varies typically by 1-2 μm.

The transverse position, size and angles of the luminous region relative to the *BABAR* coordinate system are determined by analyzing the distribution of the closest distance of approach to the z-axis of the tracks in well measured two-track events as a function of the azimuth ϕ. The longitudinal

parameters are derived from the longitudinal vertex distribution of the two tracks. A combined fit to 9 parameters (3 average coordinates, 3 widths, and 3 small angles) converges readily, even after significant changes in the beam position. The uncertainties in the average beam position are of the order of a few μm in the transverse plane and 100 μm along the collision axis. Run-by-run variations in the beam position are comparable to these measurement uncertainties, indicating that the beams are stable over the period of a typical run. The fit parameters are stored run by run in the conditions database. These measurements are also checked off-line by measuring the primary vertices in multi-hadron events. The measured horizontal and longitudinal beam sizes, corrected for tracking resolution, are consistent with those measured by PEP-II.

2.3 Detector overview

The *BABAR* detector (figure 2.3, 2.4) has been designed and fabricated by a collaboration of 500 physicists of XX institutions from 9 countries and installed at SLAC in Fall 1998. First data with PEP-II colliding beams were collected in May 1999.

The *BABAR* superconducting solenoid which produces a field of 1.5 T axial magnetic field contains a set of nested detectors: a five layers Silicon Vertex Tracker (SVT), a central Drift Chamber (DCH) for charged particles detection and momentum measurement ,a quartz-bar Ĉerenkov radiation detector (DIRC) for particle identification, and a CsI crystal electromagnetic calorimeter for detecting photons and separating electrons from charged pions. The calorimeter has a barrel section and endcap which extends it asymmetrically into the forward direction (e^- beam direction), where many of the collision products emerge. Two layers of cylindrical resistive plate counters (RPCs) are located between the barrel calorimeter and the magnet cryostat. All the detectors located inside the magnet have full acceptance in azimuth. The flux return outside the cryostat is composed of 18 layers of steel, which increase in thickness outward, and are instrumented with 19 layers of planar RPCs in the barrel and 18 in the endcaps. The RPC's allow the separation of muons and charged hadrons, and also detect penetrating neutral-strange hadrons.

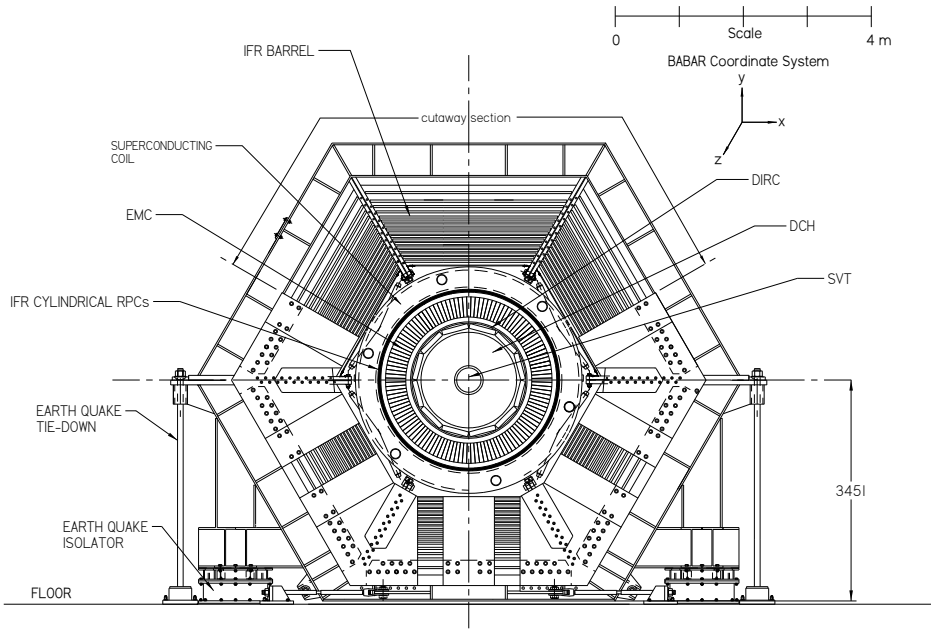

Figure 2.3: *BABAR* detector front view.

Since the average momentum of charged particles produced in B meson decay is less than 1 GeV/c, the errors on the measured track parameters are dominated by multiple Coulomb scattering, rather than the intrinsic spatial resolution of the detectors. Similarly, the detection efficiency and energy resolution of low energy photons are severely impacted by material in front of the calorimeter. Thus, special care has been given to keep the material in the active volume of the detector to a minimum. Figure 2.5 shows the distribution of material in the various detector systems in units of radiation lengths. Specifically, each curve indicates the material a particle traverses before it reaches the first active element of a specific detector system.

2.4 Silicon Vertex Tracker

The Silicon Vertex Tracker is the fundamental detector for the reconstruction of the B decay vertex and the secondary vertices, as well as the tracking of low momenta particles. Section 3 has been dedicated to detailed description of the design, construction and performance of this detector.

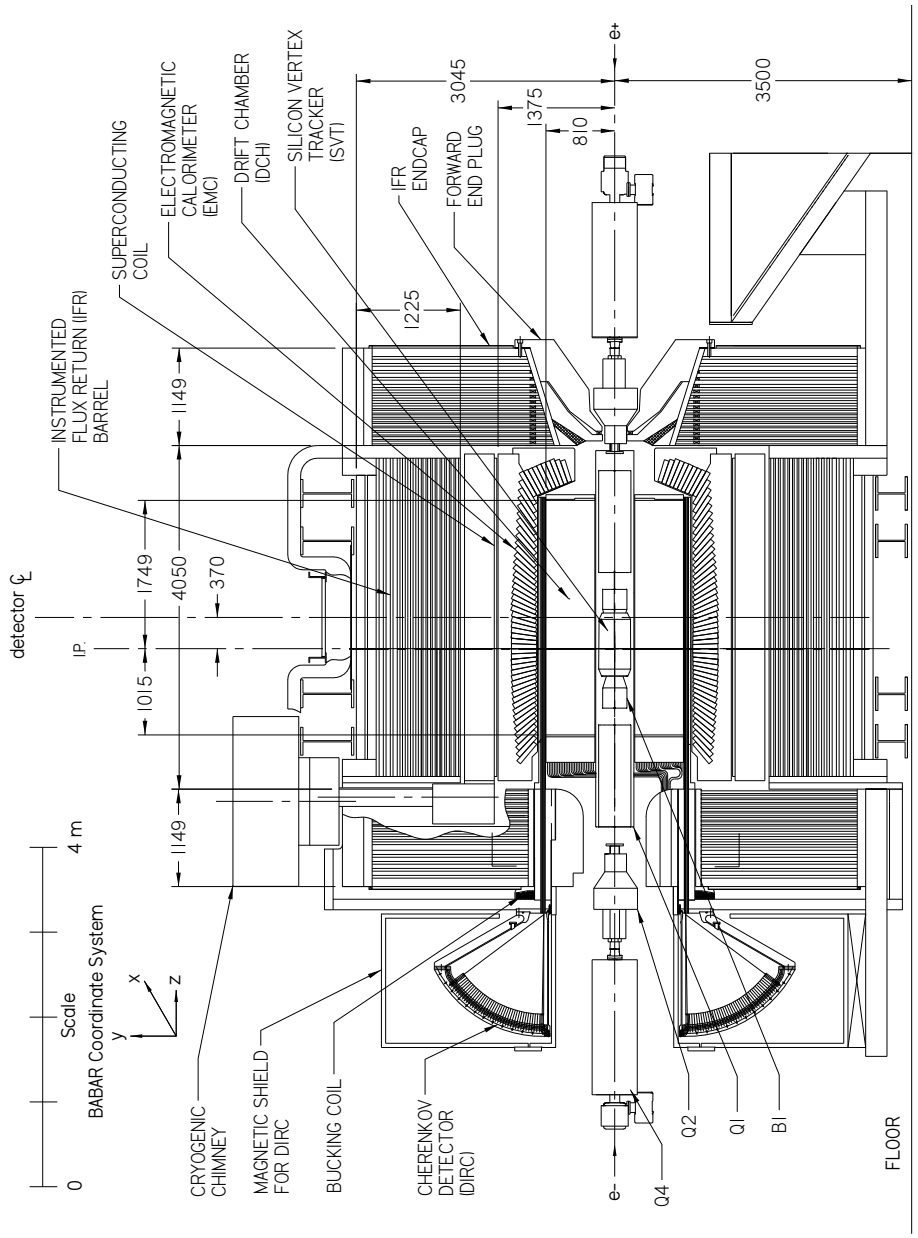

Figure 2.4: *BABAR* detector side view.

2.5 Drift Chamber

The Drift chamber (DCH) is the main tracking device for charged particles with transverse momenta p_T about above $120\,\mathrm{MeV}/c$, providing the measure-

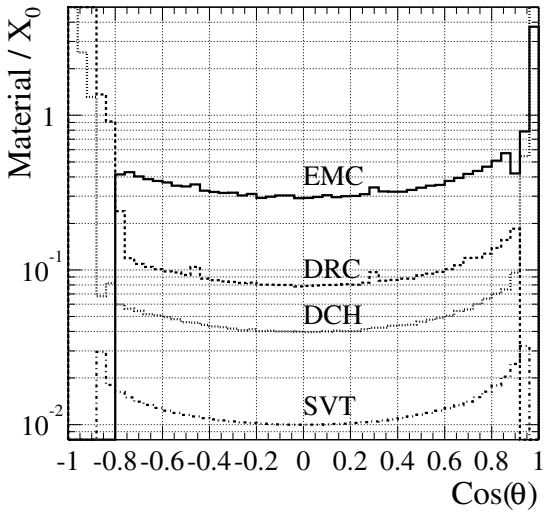

Figure 2.5: BABAR material.

ment of p_T from the curvature of the particle traversing the 1.5 T magnetic field.

2.5.1 Purpose and design requirements

It is designed to provide excellent momentum resolution in order to reconstruct exclusive final states with minimal background. For almost all momenta, multiple scattering is a significant, if not dominant, limitation on track parameter resolution. In order to reduce this contribution to the chamber p_T measurement, material within the chamber volume has been minimized by using low-mass aluminum field wires and a low-mass helium-based counting gas. The chamber structure is also designed to be as light as possible. A thin inner wall improves the contribution of the high-precision measurement in the outer layer of the SVT to the p_T resolution, and minimizes backgrounds due to photon conversions in the chamber wall. Material in the outer walls and the forward endplate has been minimized so as not to degrade the performance of the DIRC and EMC systems.

The DCH participates in the detector trigger by providing one of two complementary fast data streams with a latency of less than 11.5 μs and a maximum jitter of about 0.5 μs. The DCH trigger requires one and one-half tracks, *i.e.,* one track traversing the full chamber radius together with one

track traversing at least half the chamber radius.

For low momentum particles, the DCH provides particle identification by measurement of ionization loss ($\mathrm{d}E/\mathrm{d}x$). For the helium-based gas mixtures under consideration, a resolution of around 7% should be attainable for the $\mathrm{d}E/\mathrm{d}x$ measurement, allowing π/K separation up to 700 MeV/c. This capability is complementary to the DIRC in the barrel region, while in the extreme backward and forward directions where there is no dedicated particle identification device, it is the only available measurement.

The DCH also allows the reconstruction of secondary vertices, such as decays of K_S^0 s outside the silicon detector volume. For this purpose, the chamber should be able to measure not only the transverse coordinate, but also the longitudinal position of tracks with good ($\sim$1 mm) resolution. Good z resolution also aids in matching DCH and SVT tracks, and in projecting tracks to the DIRC and calorimeter.

Finally, the chamber must be operational with a margin of safety at the expected backgrounds, which are predicted to be $\sim$5 kHz/cell for the innermost layers. For a five-year period of operation, the integrated charge is expected to be 0.025C/cm for sense wires in the innermost DCH layers, where variations in z and ϕ have been included.

2.5.2 Mechanical design and overview

The final design adopted for the Drift Chamber, illustrated in figure 2.6, consist of a 280 cm-long cylinder with an inner radius of 23.6 cm and an outer radius of 80.9 cm.

It is mounted in cantilever from the rear endplate to the DIRC central support tube, within the volume inside the DIRC and outside the PEP-II support tube. The center of the chamber is displaced forward by 36.7 cm to improve the forward track length, given the asymmetric boost for the $\Upsilon(4S)$ events. The beryllium inner wall (0.28% radiation lengths), the thin outer half of the forward endplate (15 cm aluminum), and the carbon-fiber outer cylinder are all designed to minimize material in front of the calorimeter.

The drift system design consists of of 7104 hexagonal cells (fig. 2.7), approximately 1.8 cm wide by 1.2 cm high, arranged in 40 concentric layers between a radius of 25.3 and 79.0 cm. The active volume provides charged particle tracking over the polar angle range $-0.92 < cos\theta_{lab} < 0.96$. The 40

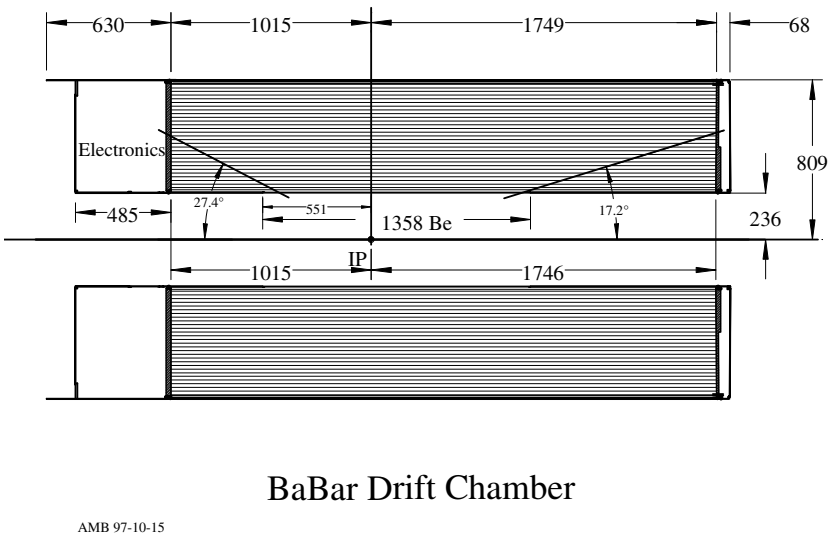

Figure 2.6: *BABAR* Drift Chamber

layers are grouped into 10 superlayers [1] of 4 layers each, organized with the same orientation for sense and field wires within a given superlayer. The superlayer structure facilitates fast local segment finding as the first step in pattern recognition. This arrangement is particularly important for L1 trigger decisions. Superlayers alternate in orientation, first axial (A), then plus a small stereo angle (U), followed by minus a small stereo angle (V). All superlayers participate in the L1 track finding.

[1] Cylindrical layers of cells are grouped four at a time into super layers. The first 16 layers are shown in fig 2.7. The plus signs, open circles, filled circles, and crosses denote sense wires, field wires, guard wires, and clearing wires, respectively. Lines have been added between field wires to aid in visualization of the cells. The numbers on the right side give the stereo angles (mrad) of sense wires in each layer. A 1 mm thick beryllium inner cylinder is shown inside of the first layer.

Table 2.2: Layer arrangement for the *BABAR* Drift Chamber

Superlayer	Inner Radius [cm]	Cells/ Layer	Stereo Angle [mrad]
1	26.04	96	0
2	31.85	112	+[44.9–50.0]
3	37.05	128	−[52.3–57.4]
4	42.27	144	0
5	48.08	176	+[55.6–59.7]
6	53.32	192	−[62.8–66.9]
7	58.54	208	0
8	64.30	224	+[65.0–68.5]
9	69.52	240	−[72.1–75.8]
10	74.72	256	0

Individual cells are formed by either $3\times120\,\mu$m grounded aluminum field wires (inner cells in a superlayer), or 2 field wires and $1\times80\,\mu$m aluminum cathode wire at about 350 V (outer cells in a superlayer), per $20\,\mu$m rhenium-tungsten sense wire operating at a nominal 1900–1960 V. Table 2.2 lists a summary of the main geometric features of the design. The counting gas is a low-mass 80%:20% mixture of He:Isobutane, with a small amount (3000 ppm) of water vapor to prolong the lifetime of the chamber in a high rate environment. The combination of low-mass gas and minimization of material in the field cage itself, is designed to reduce the contribution of multiple scattering to the p_T resolution for the typically soft tracks produced in a $\Upsilon(4S)$ event.

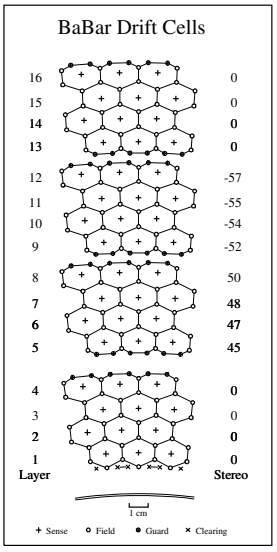

Figure 2.7: *BABAR* Drift Cell Configuration.

The reconstruction algorithm for tracks of charged particles is described in detail in section 5.

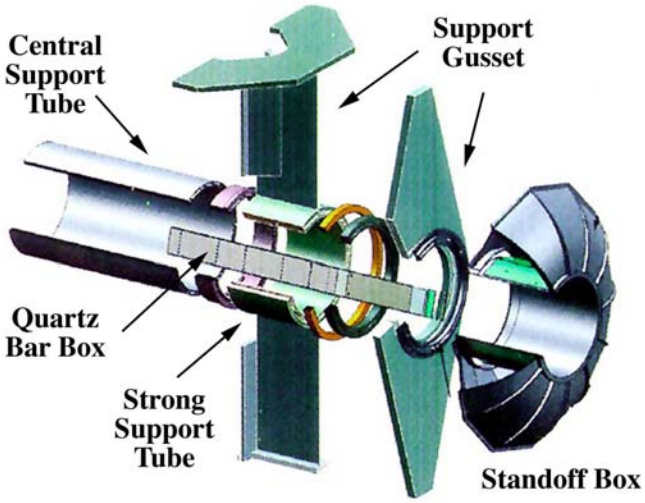

Figure 2.8: Schematics of the DIRC mechanical support structure.

2.6 Ĉherenkov light detector

The DIRC (fig. 2.8), the Detector of Internally Reflected Ĉherenkov radiation, is a novel concept and technology employed primarily for the separation of pions and kaons from about 500 MeV/c to the kinematic limit of 4 GeV/c.

The Particle Identification (PID) system is surrounded by a high-performance CsI electromagnetic calorimeter. Thus, the PID system inside the calorimeter volume should be thin and uniform in radiation lengths (to minimize degradation of the fine calorimeter energy resolution) and thin in the radial dimension to reduce the volume, hence, the CsI material cost of the calorimeter. Finally, for high-luminosity running conditions, the PID system must have fast signal response, and be able to tolerate high backgrounds.

2.6.1 Principles and layout

The DIRC [24] is a novel type of ring-imaging Ĉherenkov detector, based on the principle that the magnitudes of angles are maintained upon reflection from a flat surface. Figure 2.9 shows a schematic of the DIRC geometry that illustrates the principles of light production, transport, and imaging. The radiator material of the DIRC is synthetic fused silica (colloquially

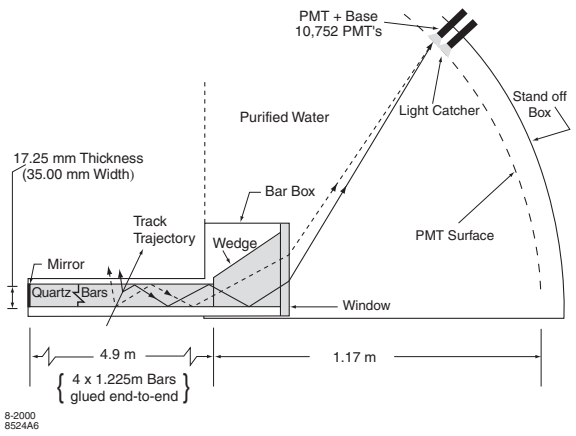

Figure 2.9: Schematics of the DIRC fused silica radiator bar and imaging region.

referred to as "quartz") in the form of long, thin bars with rectangular cross section. These bars serve both as radiators and as light pipes for the portion of the light trapped in the radiator by total internal reflection. A charged particle with velocity v, traversing the fused silica bar with index of refraction $n(\sim 1.473)$, generates a cone of Cherenkov photons of half-angle θ_c with respect to the particle direction, where $\cos\theta_c = 1/\beta n(\beta = v/c, c =$ velocity of light). For particles with $\beta \approx 1$, some photons will always lie within the total internal reflection limit, and will be transported to either one or both ends of the bar, depending on the particle incident angle. To avoid having to instrument both bar ends with photon detectors, a mirror is placed at the forward end, perpendicular to the bar axis, to reflect incident photons to the backward (instrumented) bar end.

Once photons arrive at the instrumented end, most of them emerge into a water-filled expansion region, called the standoff box. A fused silica wedge at the exit of the bar reflects photons at large angles and thereby reduces the size of the required detection surface. The photons are detected by an array of densely packed photomultiplier tubes (PMTs), each surrounded by reflecting "light catcher" cones [25] to capture light which would otherwise miss the PMT active area. The PMTs are placed about 1.2 m from the bar end. The expected Cherenkov light pattern at this surface is essentially a conic section, whose cone opening-angle is the Cherenkov production angle modified by refraction at the exit from the fused silica window.

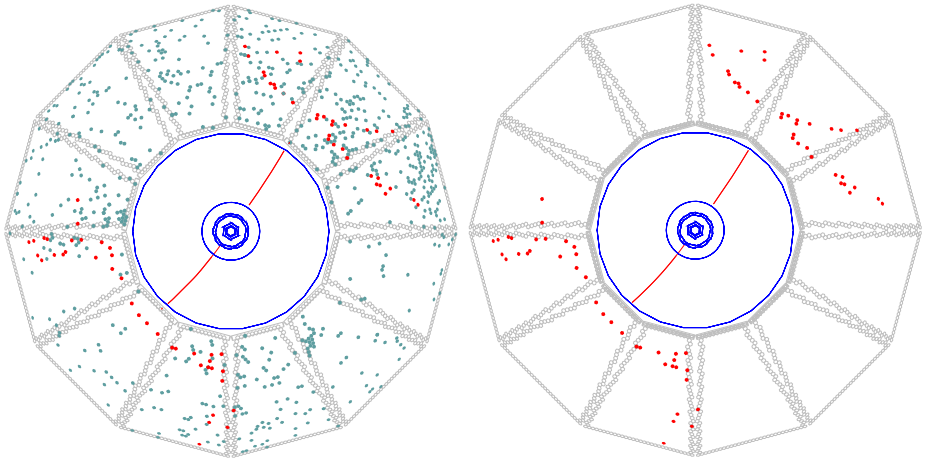

Figure 2.10: Display of one $e^+e^- \to \mu^+\mu^-$ event reconstructed in *BABAR* with two different time cuts. On the left, all DIRC PMTs that were hit within the ±300 ns trigger window are shown. On the right, only those PMTs that were hit within 8 ns of the expected Ĉherenkov photon arrival time are displayed.

The DIRC is intrinsically a three-dimensional imaging device. Photons are focused onto the phototube detection surface via a "pin-hole" defined by the exit aperture of the bar, so that the photon propagation angles can be measured in two-dimensional space formed by the surface of the photo-multipliers. The time taken for the photon to travel from the point of origin to the pmt is also related to the photon propagation angle $(\alpha_x, \alpha_y, \alpha_z)$ with respect to the bar axis. As the track position and angles are known from the tracking system, these three α angles can be used to (over-)determine the Ĉherenkov angle θ_c. This over-constraint on the angles is particularly useful in dealing with high background rates.

2.6.2 Ĉerenkov angle reconstruction

An unbinned maximum likelihood formalism incorporates all information provided by the space and time measurements from the DIRC.

The emission angle and the arrival time of the Ĉherenkov photons are reconstructed from the observed space-time coordinates of the PMT hits, transformed into the Ĉherenkov coordinate system. The known spatial position of the bar through which the track passed and the PMTs hit within

the readout window of ±300 ns of the trigger signal is used to calculate the three-dimensional vector pointing from the center of the end of the bar to the center of each tube. This vector is then extrapolated into the synthetic fused silica bar using Snell's law. This procedure defines, up to the top/bottom, left/right, forward/backward and wedge/no-wedge ambiguities, the Cherenkov angles θ_c and ϕ_c of a photon.

The DIRC time measurement represents the third dimension of the photomultiplier hit reconstruction. The timing resolution is insufficiently precise to be competitive with the positional information for Cherenkov angle reconstruction, but is used to suppress background hits from the accelerator and, more importantly, other tracks in the same event. It is also used to resolve the forward-backward and wedge ambiguities in the hit-to-track association. The relevant observable to distinguish between signal and background photons is the difference between the measured and expected photon time, δt_γ. It is calculated for each photon using the track time-of-flight (assuming it to be a charged pion), the measured hit time of the PMT and the photon propagation time within the bar and the water filled standoff box. The time information and the requirement of using only physically possible photon propagation paths that are within the region of total internal reflection reduces the number of ambiguities from 16 to typically 3. Applying the time information also substantially improves the correct matching of photons with tracks and reduces the number of accelerator induced background hits by approximately a factor 40, as can be seen in Figure 2.10.

The reconstruction routine currently provides a likelihood value for each for the 5 stable particle types (e,μ,π,K,p) if the track passes through the active volume of the DIRC. These likelihoods are calculated in an iterative process by maximizing the likelihood value for the entire event while testing different hypotheses for each track. If enough photons are found, the result of a fit of θ_c and the number of observed signal and background photons are also given for each track.

2.6.3 Performance

Figure 2.11 shows the number of photoelectrons as a function of the polar angle. It varies from a minimum of about 20 for small polar angles at the center of the barrel to well over 50 at large polar angles. This is in

good agreement with the value expected from the Monte Carlo simulation at all angles. This spectrum also demonstrates a very useful feature of the

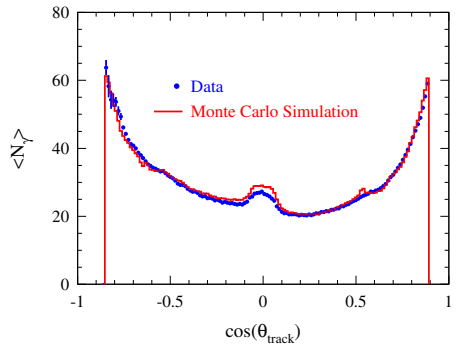

Figure 2.11: Number of detected photoelectrons *vs.* track polar angle for reconstructed di-muon events in data and simulation.

DIRC in the *BABAR* environment, namely, the performance improves in the forward direction, as is needed to cope with the angle-momentum correlation of particles from the boost. The small decreasing of the number of photons from the backward direction to the forward one is a consequence of the photon absorption along the bar before reaching the stand off box in the backward end.

With the present alignment, the typical track Ĉherenkov angle resolution for di-muon events is shown in Figure 2.12 to be about 2.5 mrad. This is about 15% worse than the 2.2 mrad expected from simulation. From the measured single track resolution *vs.* momentum in di-muon events and

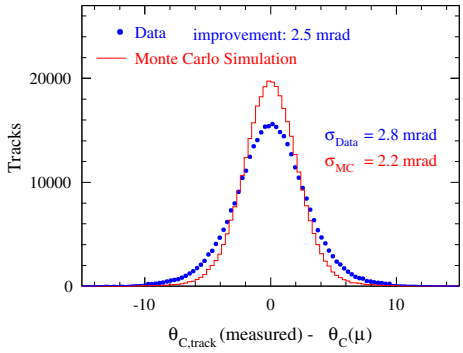

Figure 2.12: Resolution of the reconstructed Ĉherenkov polar angle per track for di-muons.

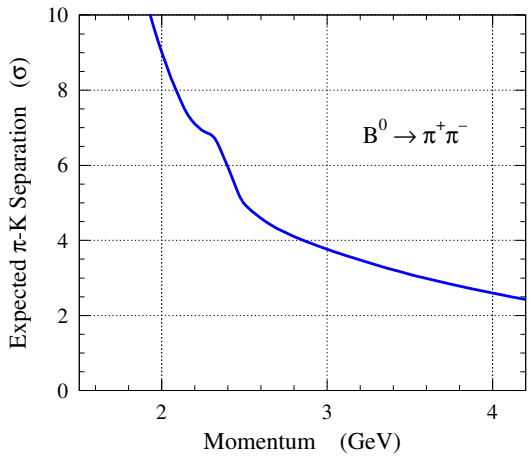

Figure 2.13: π-K separation in $B^0 \to \pi^+\pi^-$ events *vs.* track momentum inferred from the measured Ĉherenkov angle resolution and number of Ĉherenkov photons per track in di-muon events.

the difference between the expected Ĉherenkov angles of charged pions and kaons, the pion-kaon separation power of the DIRC can be inferred. As shown in Figure 2.13, the separation between kaons and pions at 3 GeV/c is about 4.3 σ, approximately 10% worse than predicted by the Monte Carlo simulation.

Figure 2.14 shows an example of the use of the DIRC for sample selection. The $K\pi$ invariant two body mass spectra are shown without (a), and with (b) the use of the DIRC for kaon identification. The mass peak corresponds to the decay of the D^0 particle.

The efficiency for correctly identifying a charged kaon that hit a radiator bar and the probability to wrongly identify a pion as kaon are determined using D^0 decays selected kinematically from inclusive D^* production and are shown as a function of track momentum in Fig. 2.15. The mean kaon selection efficiency and pion mis-identification are $96.2 \pm 0.2\%$ (stat.) and $2.1 \pm 0.1\%$ (stat.), respectively.

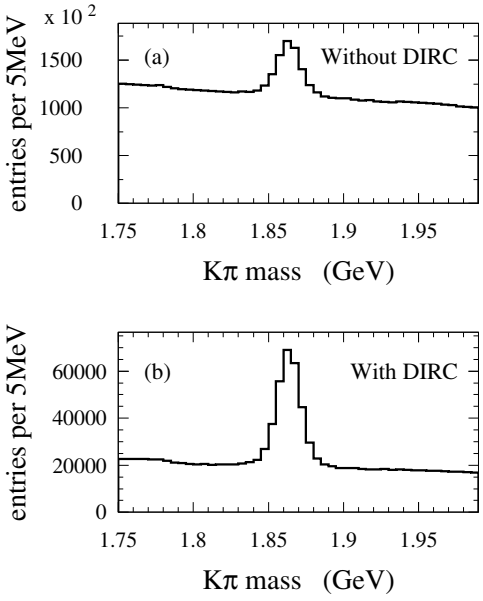

Figure 2.14: Invariant Kπ inclusive mass spectrum (a) without and (b) with the use of the DIRC for kaon identification. The mass peak corresponds to the decay of the D^0 particle.

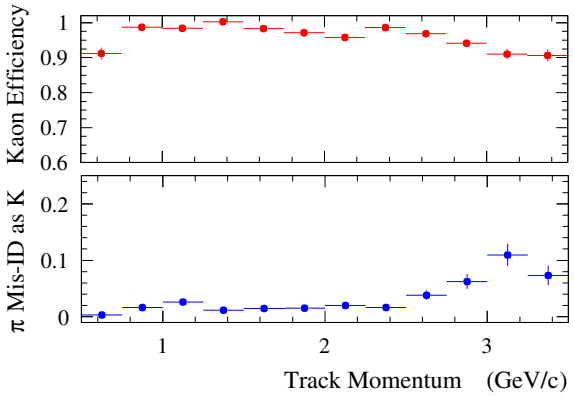

Figure 2.15: Efficiency and mis-identification probability for the selection of charged kaons as a function of track momentum determined using D^0 decays selected kinematically from inclusive D^* production.

2.7 Electomagnetic calorimeter

2.7.1 Design requirements

The *BABAR* electromagnetic calorimeter is required to detect low-energy photons with high efficiency, and to precisely measure their energy and direction. It is also the primary sub-detector providing electron-hadron separation. The efficient reconstruction of extremely rare decays of B mesons containing π^0 s (e.g. $B^0 \to \pi^0\pi^0$) pose the most stringent design requirements on energy resolution of order 1% while excellent photon efficiency at low energies ($\sim$ (20 MeV)) is required for efficient reconstruction of B meson decays containing multiple π^0 and η [26]. Similar precision is required for efficient separation of electrons and hadrons with purities required at the 0.1% level for momentum as low as 500 MeV/c. The upper bound on the energy range required is set by the highest energy particles produced. At the $\Upsilon(4S)$ these are 9 GeV electrons from Bhabha events rising to 13 GeV to allow for possible running at the $\Upsilon(5S)$ The π^0 mass resolution is dominated by the energy resolution at low energies ($< 2\,\mathrm{GeV}$) and the angular resolution at high energies. The angular resolution is required to be a few milliradians in order to maintain good π^0 mass resolution at all energies. The need for high efficiency requires hermetic coverage of the acceptance region while excellent resolution can only be achieved by minimizing the material in front of and between the active detector elements. In addition we require high efficiency in data taking over the anticipated 10 year lifetime of the experiment. This implies that all inaccessible detector elements must be highly reliable and that routine detector maintenance such as calibrations be performed with minimal interference to normal detector operation.

2.7.2 Detector layout

The electromagnetic calorimeter (fig. 2.16) contains 6580 CsI crystals doped with thallium iodide at $\sim$1000ppm. Each crystal is a truncated trapezoidal pyramid and ranges from 16 to 17.5 radiation lengths in thickness. The front faces are typically $\sim$5 cm in each dimension. The crystals are arranged quasi-projectively in a barrel structure of 48 θ rows by 120 crystals in azimuth (ϕ), with an inner radius of 90 cm. The forward end is closed by a separable endcap capable of holding nine additional rows. At present, eight are filled

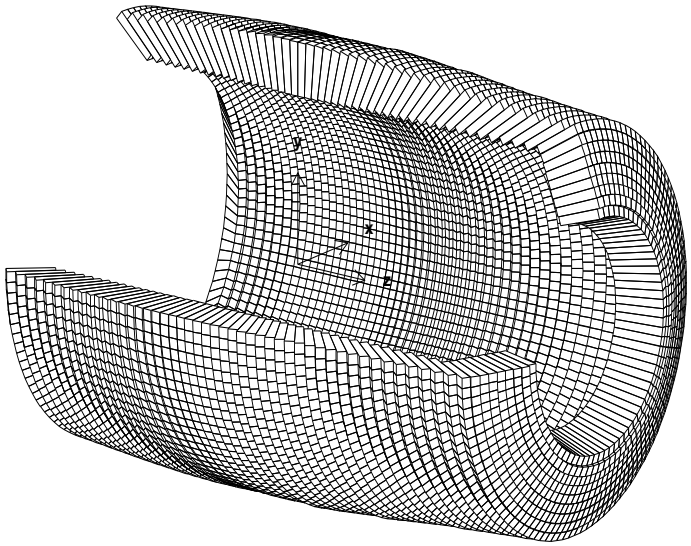

Figure 2.16: The crystal geometry of the Electromagnetic Calorimeter.

with crystals and the innermost with shielding absorber. The polar angle coverage of the calorimeter is $-0.78 < cos\theta_{lab} < 0.96$. Beamline elements occlude $cos\theta_{lab} > 0.94$. Each crystal is wrapped with a diffuse reflective material (TYVEK) and housed in a thin eggcrate-like carbon fiber composite mechanical structure. There are 280 such modules in the barrel (7 types, 40 of each type) and 20 identical endcap modules. Crystals are read out with two independent $2\,cm^2$ large area PIN photodiodes epoxied to their rear faces. Dual range ASIC preamplifiers reside directly behind the photodiodes in a shielded housing that also provides a thermal path for heat removal. Shielded ribbon cables carry analog signals to the end flanges of the barrel and the back plate of the endcap where dual-range digitizing electronics provide 18 bit resolution of signals from $\sim$50 keV (LSB) to $\sim$10 GeV. A short shaping time of 400ns is used in the preamplifiers to reduce the impact of soft ($<$5 MeV) beam related photon backgrounds. Noise performance can be recovered by digitally processing the waveform sampled at 4MHz.

2.7.3 Cristals description

CsI(Tl) scintillator is a natural technology choice to achieve our design requirements. The electromagnetic calorimeter is a hermetic, total-absorption array of 0.1% thallium-iodide doped cesium iodide (CsI(Tl))crystals, read out with solid state photo-detectors matched to the spectrum of scintillation light. Crystals are arranged quasi-projectively in a barrel-endcap geometry (Figure 2.16). The high light yield and small Molière radius gives the

Table 2.3: Properties of CsI(Tl) .

Radiation Length	1.86 cm
Molière Radius	3.8 cm
Density	4.53 g/cm^3
Light Yield	50000 γ/ MeV
Light Yield Temp. Coeff.	0.28 %/°C
Peak Emission λ_{max}	565 nm
Refractive Index (λ_{max})	1.79
Decay Time	680 ns (64%)
	3.34 μs (36%)

excellent energy and angular resolution required, while the short radiation length guarantees complete shower containment at *BABAR* energies with a relatively compact design. Furthermore, the high light yield and peak of the emission spectrum permit efficient use of a silicon photodiode readout. This readout chain is itself compact and most importantly allows the calorimeter to be located within the magnetic solenoid volume, minimizing the material in front of the detector which can cause pre-showering.

The energy resolution of a calorimeter is determined by fluctuations in the electromagnetic shower propagation and in the case of a homogeneous crystal detector is empirically described by Eq. 2.1. The resolution as a function of energy E is given by σ_E parameterized as the quadratic sum of a stochastic term σ_1 and a constant term σ_2.

$$\frac{\sigma_E}{E} = \frac{\sigma_1}{\sqrt[4]{E}} \oplus \sigma_2 \tag{2.1}$$

The stochastic term, which is dominant at at low energies ($<$ 100 MeV),

arises from fluctuations in photon statistics and electronic noise in the readout chain. If care is taken to minimize the light loss fluctuations from showers traversing non-sensitive gaps and inter-crystal material while maximizing the light transmission into the photodiodes, this term can be reduced to 1-2% in CsI(Tl), where it is assumed that the coherent and incoherent noise introduced by the readout system can be reduced to have negligible impact on the resolution. This demands the design of low-noise electronics and also the implementation of a real-time digital signal processing algorithm to achieve optimal performance.

The constant term, dominant at higher energies ($> 1\,\mathrm{GeV}$), arises from several effects of which the principals are fluctuations in shower containment due to leakage out the rear of the crystal, albedo, absorption of energy in the inter-crystal support materials and from pre-showering in the materials in front of the crystal. These effects can be minimized by appropriate choice of the detector geometry and support-structure material; their impact on resolution is constant in time.

Non-uniformities in the cristals result in a non-linear energy response as mean shower depth varies logarithmically with incident energy. Some can be reduced to negligible levels initially, by careful quality assurance of the crystals and the wrapping procedures during construction. However, radiation damage during operation causes a degradation in response that changes with time. This requires a novel energy dependent calibration and monitoring system which employs a radioactive source, a light pulser, and reconstructed data. These calibrations must be updated every few days during operation, and be fully automated to track time dependent radiation-damage effects. Residual uncertainties in this calibration combined with shower fluctuations contributes to a degradation in resolution.

The angular resolution improves as the transverse size of the crystal decreases. However the total number of crystals required and therefore the cost increases. In addition the energy resolution is degraded by the summing of electronic noise from each crystal. The transverse size of the crystals is chosen to be comparable to the Molière radius achieving the required angular resolution at low energies of a few milliradians.This also limits the total number of crystals (and readout channels) to an acceptable level.

The inaccessibility of crystals following assembly and the requirement

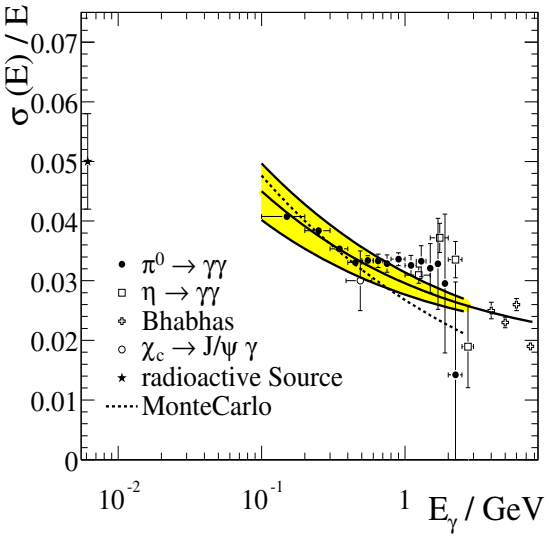

Figure 2.17: The energy resolution for the electromagnetic calorimeter measured using photon and electron candidates. The solid curve is a fit to Eq. 2.1 along and the shaded area denotes the one sigma error on the fit

of a ten year lifetime with no single crystal failures has been addressed by a combination of extensive accelerated aging tests during the design phase, and dual redundancy in the readout chain. Procedures developed during the design phase were imposed during assembly by strict quality control.

2.7.4 Performance

Energy Resolution

The energy resolution is measured directly with the radioactive source at low energy and with electrons from Bhabha scattering at high energy, yielding resolutions of $\sigma_{\rm E}/{\rm E} = 5.0 \pm 0.8\%$ at 6.13 MeV and $\sigma_{\rm E}/{\rm E} = 1.9 \pm 0.07\%$ at 7.5 GeV. Figure 2.17 shows the energy resolution extracted from a variety of data as a function of energy. The mass resolution of π^0 and η candidates in which the two photons in the decay have approximately equal energy can be used to infer the energy resolution at an energy less than 1 GeV. The process $\chi_{c1} \to J/\psi\,\gamma$ provides an additional measurement at 500 MeV. The resolution at higher energy is measured with electrons from Bhabha

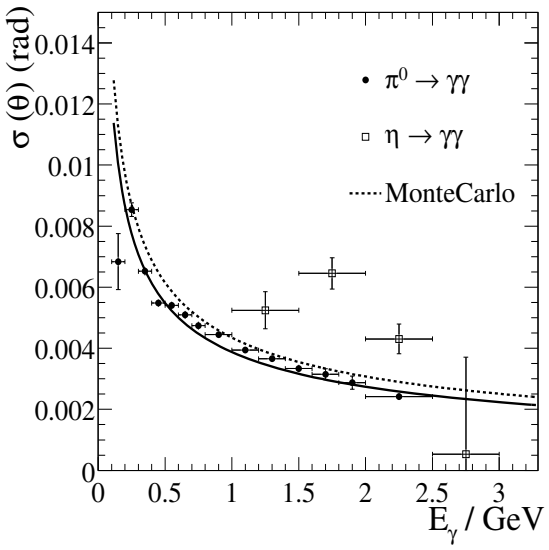

Figure 2.18: The angular resolution for the electromagnetic calorimeter measured using photon and η candidates. The solid curve is a fit to Eq. 2.2.

scattering. The expectation from Monte Carlo, where the contributions from electronic noise and low energy beam backgrounds are included, is shown as a dashed curve. The data fit the curve given by Eq. 2.1 with $\sigma_1 = 2.32 \pm 0.30\%$ and $\sigma_2 = 1.85 \pm 0.12\%$.

Angular Resolution

Figure 2.18 shows the angular resolution measured as a function of energy. The decays of π^0 and η candidates in which the two photons from the decay have approximately equal energy are used to infer the angular resolution. It varies between about 12 milliradians at low energies and 3 milliradians at high energy. The expectation from Monte Carlo is shown in the dashed curve. The data fit the empirical parameterization:

$$\frac{\sigma_{\theta,\phi}}{\mathrm{E}} = \frac{\sigma_1}{\sqrt{\mathrm{E}}} + \sigma_2 \tag{2.2}$$

where $\sigma_1 = 3.87 \pm 0.07\,\mathrm{mr}$ and $\sigma_2 = 0.00 \pm 0.04\,\mathrm{mr}$. There are many more π^0 than η decays. However the statistical significance of the disagreement between data and Monte Carlo is similar for both samples. The angular resolution tends to be higher in data. The cause of the discrepancy is currently

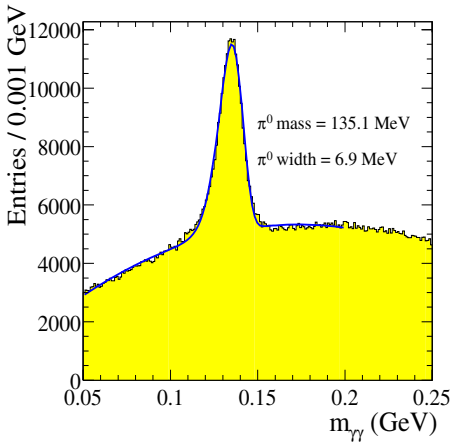

Figure 2.19: The π^0 mass peak reconstructed from photon candidates in hadronic events. The photon candidates are required to have an energy of at least 30 MeV and the energy of the π^0 must be greater than 300 MeV to reduce combinatoric backgrounds. The solid line is a fit to the data.

under investigation.

π^0 Mass and Width

Figure 2.19 shows the two-photon invariant mass for π^0 candidates. The π^0 candidates are taken from hadronic B-meson events. The invariant mass is stable to less than 1% over the full photon energy range. The width of $6.9\,\mathrm{MeV}/c^2$ compares to a Monte-Carlo estimate of $6.8\,\mathrm{MeV}/c^2$ in hadronic B meson events. In low-occupancy $\tau^+\tau^-$ events the width is observed to be $6.5\,\mathrm{MeV}/c^2$ for π^0 energies below about 1 GeV. Improved resolution is also observed in hadronic events where only isolated photons are considered.

Electron-Hadron Separation

Electron-hadron separation is accomplished by use of the shower energy, lateral shower moments and incident track parameters. The comparison of shower energy and incident momentum (E/p) is the most significant separation variable. Figure 2.20 shows the electron efficiency and pion misidentification rate for different momenta using a selection algorithm. The efficiency of electron identification is measured using electrons from radia-

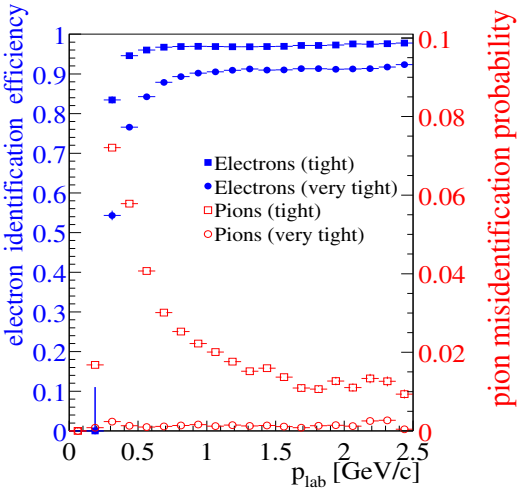

Figure 2.20: The electron efficiency and pion mis-identification rate for different momenta.

tive Bhabhas and $\gamma\gamma \to e^+e^-$ events. The pion misidentification probability is measured in three prong τ decays. The tight selector has an average efficiency of 94.8% in the momentum range $0.5\,\mathrm{GeV}/c < p < 2\,\mathrm{GeV}/c$, with a pion misidentification probability of roughly 1.2%. The very tight selector has an efficiency of 88.1% with an average pion misidentification of 0.3%. The electron-hadron separation power meets design expectations.

2.8 Instrumented flux return

2.8.1 Physics Requirements and Goals

The Instrumented Flux Return (IFR) was designed to identify muons with high efficiency and good purity and to detect neutral hadrons (primarily K_L^0 and neutrons) over a wide range of momenta and angles. Muons are important for tagging the flavor of neutral B mesons via semi-leptonic decays, for the reconstruction of vector mesons, like the J/ψ, and the study of semi-leptonic and rare decays involving leptons of B and D mesons and τ leptons. K_L^0 detection allows for the study of exclusive B decays, in particular CP eigenstates, it could also help in vetoing charm decays and improve the reconstruction of neutrinos.

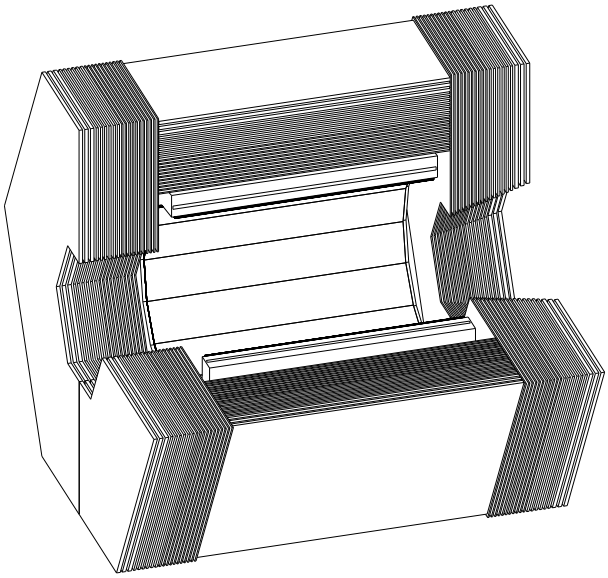

Figure 2.21: Overview of the IFR: Barrel sectors and forward (FW) and backward (BW) end-doors; the shape of the RPC modules and their dimensions are indicated.

The principal requirements for IFR are large solid angle coverage and good efficiency and high background rejection for muons down to momenta below 1 GeV/c. For neutral hadrons, high efficiency and good angular resolution are most important. Since this system is very large and difficult to access, high reliability and extensive monitoring of the detector performance and the associated electronics plus the voltage distribution are necessary.

2.8.2 Overview and RPC Concept

The IFR uses the steel flux return of the magnet as muon filter and hadron absorber. Single gap resistive plate chambers (RPC) [27] with two-coordinate readout have been chosen as detectors.

The RPC are installed in the gaps in the finely segmented steel of the six barrel sectors and the two end-doors of the flux return, as illustrated in Figure 2.21. The steel segmentation has been optimized on the basis of Monte Carlo studies of muon penetration and charged and neutral hadron interactions. The steel is segmented into 18 plates, increasing in thickness from 2 cm of the inner 9 plates to 10 cm of outermost plate(s).

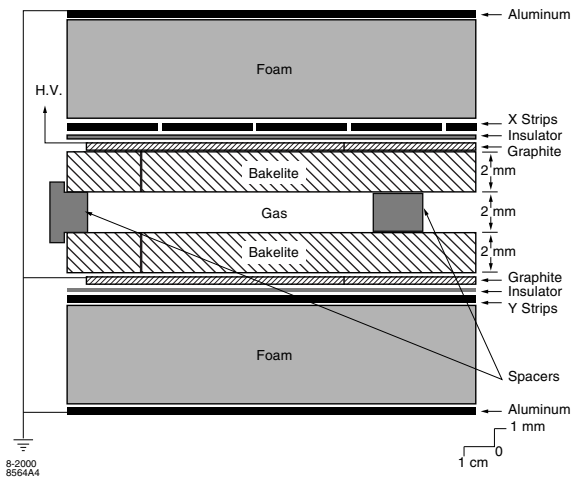

Figure 2.22: Cross section of a planar RPC with the schematics of the HV connection.

The nominal gap width is 2.2 cm İn addition, two layers of cylindrical RPCs are installed between the EMC and the magnet cryostat to detect particles exiting the EMC.

RPCs detect streamers from ionizing particles via capacitive readout strips. They offer several advantages: simple, low cost construction and the possibility of covering odd shapes with minimum dead space. Further benefits are large signals and fast response allowing for simple and robust front end electronics and good time resolution, typically 1-2 ns. The position resolution depends on the segmentation of the readout, a few mm are achievable.

A cross section of an RPC shown schematically in Figure 2.22. The construction of the planar and the cylindrical RPCs differ in detail, but are based on the same concept.

The planar RPCs consist of two bakelite (phenolic polymer) sheets, 2 mm thick and separated by a gap of 2 mm. The gap is enclosed at the edge by a 7 mm wide frame. The gap width is kept uniform by polycarbonate spacers (0.8 cm^2) that are glued to the bakelite, spaced at distances of 10 cm. The bulk resistivity of the bakelite sheets has been especially tuned to $10^{11} - 10^{12}$ Ω m. The external surfaces are coated with graphite to achieve a surface resistivity of $\approx$ 100 kΩ/square. These two graphite

surfaces are connected to high voltage (≈ 8 kV) and ground, and protected by an insulating mylar film. The bakelite surfaces facing the gap are treated with linseed oil to improve performance. The modules are operated in limited streamer mode and the signals are read out capacitively, on both sides of the gap, by external electrodes made of aluminum strips on a mylar substrate.

The cylindrical RPCs has resistive electrodes made of a special plastic composed of a conducting polymer and ABS. The gap thickness and the spacers are identical to the planar RPCs. No linseed oil or any other surface treatments have been applied. The very thin and flexible electrodes are laminated to fiberglass boards and foam to form a rigid structure. The copper readout strips are attached to the fiberglass boards.

2.8.3 Efficiency Measurements and Performance

The efficiency of the RPCs is evaluated for both normal collision data and dedicated cosmic rays. Every week cosmic ray data are recorded at different voltage settings and the efficiency is measured chamber by chamber as a function of the applied voltage. The absolute efficiency at the nominal working voltage (typically 7.6 kV) is stored in the data base for use in the event reconstruction software.

To calculate the efficiency in a given chamber, nearby hits in a given layer and hits in different layers are combined to form clusters. Two different algorithms are used: The first is based solely on the IFR information and uses data recorded with a dedicated IFR trigger; the second matches the IFR clusters with the tracks reconstructed in the drift chamber. Both these algorithms start from one-dimensional IFR clusters defined as a group of adjacent hits in one of the two readout coordinates. The cluster position is defined as the centroid of the strips in the cluster. In the first algorithm, two-dimensional clusters are formed by joining one-dimensional clusters (of the same readout coordinate) in different layers, provided the distance between their coordinate centroids is less then a given value. In each sector, two-dimensional clusters in different coordinates are combined to three-dimensional clusters as long as there are less than three layers missing one of the two coordinates. The second algorithm extrapolates charged tracks reconstructed by the drift chamber into the IFR. IFR clusters which

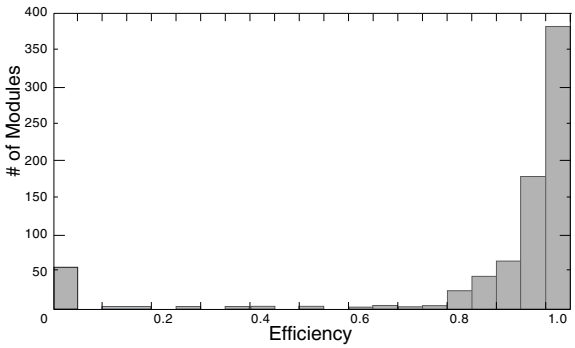

Figure 2.23: Distribution of the efficiency for all RPC modules measured with cosmic rays in June 1999. Some 50 modules were not operational at that time.

are less than 12 cm from the extrapolated track are combined to form three-dimensional or two-dimensional clusters. A detailed discussion of the clustering algorithm can be found elsewhere [28].

The residual distributions from straight line fits to two-dimensional clusters typically have an r.m.s. width of less than 1 cm. An RPC is considered efficient if a signal is detected at a distance of less than 10 cm from the fitted straight line in either of the two readout planes. Following the installation and commissioning of the IFR system all the RPC modules were tested with cosmic rays and their efficiency was measured. The results are presented in Figure 2.23. Of the RPC active modules 75% exceed an efficiency of 90%.

Early tests indicated that the RPC dark current was very temperature dependent, specifically, the current increases 14-20% per °C. Since the IR experimental hall does not have temperatures regulation this presents a serious problem. The FECs that are installed in the steel gaps each produce 3 W, adding up to a total power dissipation of 3.3 kW in the barrel and 1.3 kW in the forward end-door.

During the first summer of operation the daily average temperature in the IR hall was 28 °C and the maximum hall temperature frequently exceeded 31 °C. The temperature inside the steel rose to more than 37 °C and the dark currents in many modules exceeded the capabilities of the HV system and RPCs had to be temporarily disconnected.

To overcome this problem water cooling was installed on the barrel and

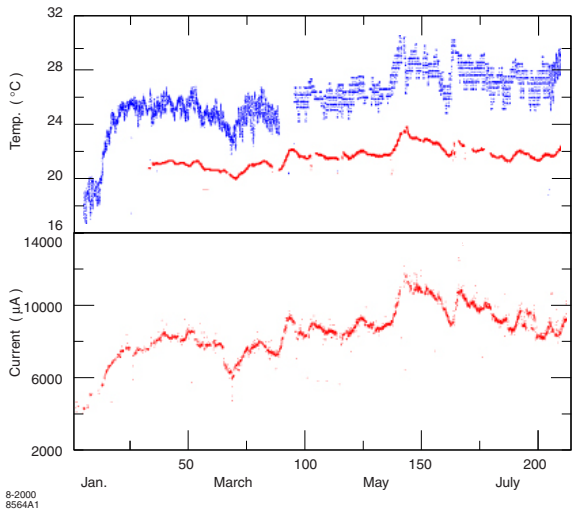

Figure 2.24: History of the temperature and dark current in the RPC modules since January 2000. top: temperature in the IR-2 hall and in the backward end-door; bottom: total dark current in the 216 modules of the backward end-door.

end-door steel, removing $\approx$ 10kW of heat and stabilizing the temperature to 20-21 °C in the barrel, 22 °C in the backward and 24 °C in the forward end-doors. Figure 2.24 shows the history of temperature in the hall and temperature and total dark current in the backward end-door. While the current closely follow the temperature variations, the range of change is now limited to a few degrees.

During the operation at high temperatures a large fraction of the RPCs ($> 50\%$) showed not only very high dark currents but also a reduction in efficiency [29]. After the cooling was installed and the RPCs were reconnected, some of them continued to deteriorate while others remained stable, some of them ($> 30\%$) at full efficiency. (see Figure 2.25. Detailed efficiency studies revealed large regions of very low efficiencies in these modules, but no clear pattern was identified.

The cause of the efficiency loss remains under investigation. Several possible causes have been excluded as the primary source of the problem, such as the change in the bakelite bulk resistivity, loosened spacers, gas flow or composition. A number of prototype RPCs developed similar efficiency problems after being operated above a temperature 36 °C for a period of

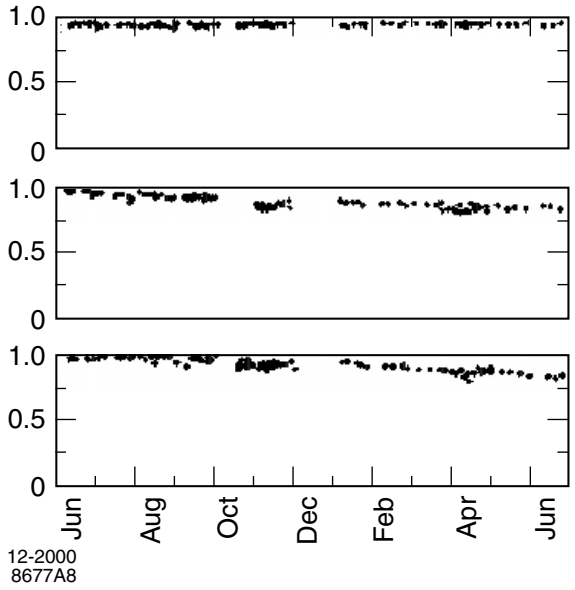

Figure 2.25: Efficiency history for 12 months starting in June 1999 for RPC modules showing different performance: a) highly efficient and stable; b) slow continuous decrease in efficiency; c) more recent, faster decease in efficiency.

two weeks. In some of these modules evidence was found that the linseed oil had failed to cure and had accumulated at various spots under the impact of the high voltage.

Improvement program

In order to solve some of the inefficiency problems an improvement program is currently under development. At the moment it foresees at the end of this year the substitution of the RPCs in the endcap region with new ones based on the same base concept but with an improved linseed oil essication technique. The modules in the barrel region are more complicated to substitute and the eventual replacement is foreseen in two years from now. During this period of time studies to improve the performance are in program and will eventually lead to a different technology for the barrel RPCs.

Muon Identification

While muon identification relies almost entirely on the IFR, other detector systems provide complementary information. Charged particles are reconstructed in the SVT and DCH and muon candidates are required to meet the criteria for minimum ionizing particles in the EMC, i.e. tracks depositing large amounts of energy are rejected. Charged tracks that are reconstructed in the tracking systems are extrapolated to the IFR taking into account the non-uniform magnetic field, multiple scattering and the average energy loss. The projected intersections with the RPC planes are computed and for each readout plane all clusters detected within a maximum distance from the predicted intersection are associated with the track.

For each cluster in the IFR associated with a charged track a number of variables are defined to discriminate muons from charged hadrons: 1) the total number of interaction lengths traversed from the IP to the last RPC layer with an associated cluster, 2) the difference between this measured number of interaction lengths and the number of interaction lengths predicted for a muon of the same momentum and angle, 3) the average number and the r.m.s. of the distribution of RPC strips per layer, 4) the $\chi^2$the for geometric match between the projected track and the centroids of clusters in different RPC layers, and 5) the χ^2 of a polynomial fit to the 2-dimensional IFR

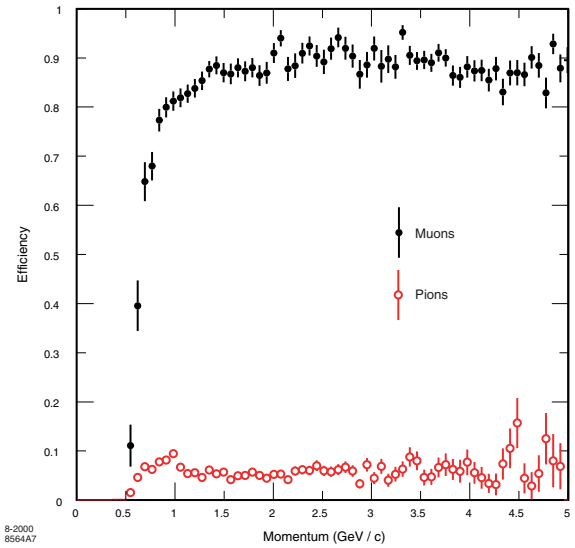

Figure 2.26: Muon efficiency and pion misidentification probability as a function of the track momentum, obtained with loose selection criteria.

clusters. These variables will be combined into global likelihood analysis to optimize the efficiency and purity of muons. At present, cuts on individual variables are employed.

The performance of muon selection has been tested on samples of muons from $\mu\mu ee$ and $\mu\mu\gamma$ final states and pions from 3-prong τ decays and $K_S \to \pi^+\pi^-$ decays. The selection of these control samples is based on kinematic variables, and not on variables used for muon selection. As illustrated in Figure 2.26 a muon detection efficiency of 90% has been achieved in the momentum range of $1 < p < 3$ GeV/c with a 5% fake rate for pions. The pion misidentification can be reduced by a factor of two by tighter selection cuts which lower the detection efficiency to 75%. No correction for decay-in-flight has been applied.

K_L and Neutral Hadron Detection

K_L and other neutral hadrons interact in the iron of the IFR and can be identified as clusters that are not associated with a charged track. Monte Carlo simulations predict that about 64% of K_L's above a momentum of 1 GeV/c produce one cluster in the cylindrical RPC, and/or a cluster with hits in two or more planar RPC layers. The centroid of the 3-dimensional

IFR cluster is taken as the interaction point of the neutral hadron, and thus defines its production angle. Due to insufficient sampling no calorimetric energy information can be obtained.

Pairs of unassociated clusters that have an angular separation of $\leq$ 0.3 rad are combined into a composite cluster, thus joining clusters that originate from showers that spread into adjacent sector of the barrel, several sections of the end-doors and/or the cylindrical RPC. This procedures also combines multiple clusters from large fluctuations in the hadronic shower development.

Since a significant fraction of the hadrons interact before reaching the IFR, information from the EMC and the cylindrical RPCs is combined and the production angle of the neutral hadron is taken from the first interaction point in the detector. Neutral showers in the EMC are associated with the neutral hadrons detected in the IFR, based on a match in production angles. For a good match a χ^2 probability of $\geq 1\%$ is required, assuming uncorrelated angular errors of $\sigma_\phi = 0.180$ rad and $\sigma_\theta = 0.150$ rad for the polar and azimuthal angles.

An estimate of the angular resolution of the neutral hadron cluster can be derived from a sample of K_L^0 produced in the reaction $e^+e^- \to \phi\gamma \to K_L^0 K_S^0 \gamma$. The K_L^0 direction is inferred from the missing momentum computed from the measured particles in the final state, γ and K_S^0. The data in Figure 2.27 indicate that the resolution is of the order of 50 mrad.

For multi-hadron events with a reconstructed J/Ψ decay Figure 2.28 shows the angular difference, $\Delta\phi$, between the missing momentum and the direction of the nearest neutral hadron cluster. The observed peak demonstrates clearly that the missing momentum can be associated with a neutral hadron, assumed to be a K_L^0.

2.9 Electronics, Trigger, Data Acquisition and On-Line Computing

The electronics, trigger, data acquisition and on-line computing represent a collection of tightly coupled hardware and software systems. These systems were designed to maximize the physics data acceptance, maintainability and reliability while minimizing complexity, deadtime, downtime and cost.

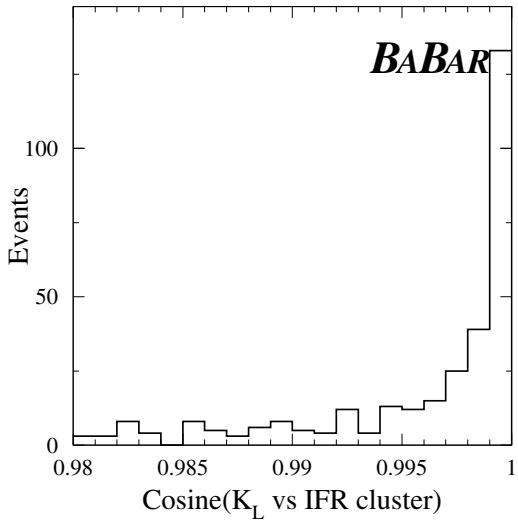

Figure 2.27: Angular difference, $\cos\Delta\theta$, between the direction of the missing momentum and the closest neutral IFR cluster for a sample of ϕ mesons produced in the reaction $e^+e^- \to \phi\gamma$ with $\phi \to K_L^0 K_S^0$.

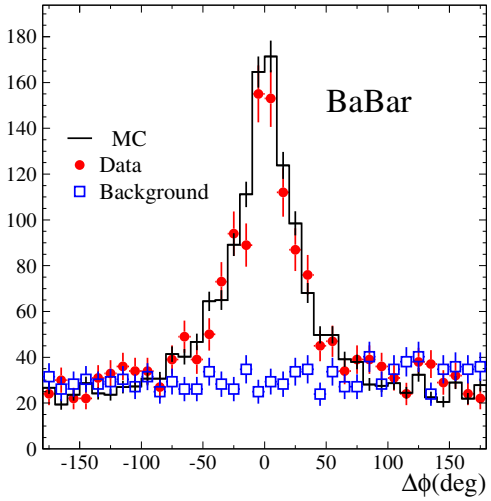

Figure 2.28: Difference between the direction of the reconstructed neutral hadron cluster and the transverse missing momentum of the event. Data and MC are normalized to the same luminosity; the background is obtained using neutral hadrons and the missing momentum from different events.

- *Front-End Electronics* (FEE) assemblies are physically located on the detector and consist of signal processing and digitization electronics along with a standard digital transport mechanism into the data acquisition system.

- A data reduction, transport and event building system, *Online Dataflow* (ODF), handles digitized data from the FEE, performs initial data reduction and formatting ("feature extraction") and builds complete events from the various data sources within the detector.

- A farm of commercial Unix processors and associated software, *Online Event Processing* (OEP), provides the real-time environment within which complete events are processed by the L3 trigger algorithms, completely reconstructed for the monitoring of a carefully selected subsample of events, and recorded in an intermediate raw data format to mass storage.

- In a second farm of processors, *Online Prompt Reconstruction* (OPR), completely reconstructs on all physics events, performs monitoring and constants generation in near real-time. Physics event data are transferred to an object database and are thus available for further analyses.

- A *Fast Control and Timing System* (FCTS) generates needed beam and trigger-related signals along with timing fiducials.

- A robust and flexible two-level trigger handles the full accelerator collision rate, one in hardware, *Level 1* (L1), the other in software, *Level 3* (L3). A provision is made for an intermediate trigger (Level 2) should unexpected conditions require its implementation.

- An *Online Run Control* (ORC) system handles the logic for managing the state of the detector systems, starting and stopping runs, and performing calibrations. A user interface provides operator access to detector operation.

- A system to control and monitor the detector and its support systems, *Online Detector Control* (ODC), is based upon the EPICS (Experimental Physics Industrial Control System) toolbox. This system

includes communication links with the PEP-II accelerator complex. User interfaces provide operator access and displays.

2.9.1 Electronics

A common electronics architecture is shared by all *BABAR* detector subsystems; common vendors were chosen for many of its components such as VME crates and power supplies. Event data from the detector flows through the FEE circuitry, while monitoring and control signals are handled by a separate, parallel system. All FEE systems, listed in Table 2.4, are mounted directly on the detector for performance reasons. This solution also minimizes the cable plant and avoids noise pickup and grounding loops generated in long analog signal cables. Electronics for all detector subsystems utilize standard *BABAR* interfaces to the global electronics and software.

Table 2.4: Overview of the Front-End Electronics (PH=pulseheight, ASD=amplifier-shaper-discriminator)

System	Elements	PH (bits)	Time (ns)	No. Channels	Custom ICs
SVT	Si Strips	4	-	150,000	ASD/storage
		-	-		
DCH	Wires	-	-	7,104	ASD
		6	2		ADC/TDC
DIRC	PMTs	-	-	10,752	ASD
		-	0.5		TDC/FIFO
EMC	PIN diodes	-	-	13,160	amplifier/shaper
		17-18	-	6,580	ADC ranging chip
IFR	RPC Strips	1	-	51,584	

Each FEE chain consists of an amplifier, digitizer, a trigger latency buffer for storing data during the L1 trigger processing, and a de-randomizing event buffer for storing data between the L1 accept and and subsequent transfer to the data acquisition system (Figure 2.29). Custom ICs have been developed to perform the signal processing (Table 2.4). The digital L1 latency buffers function as fixed length data pipelines and are managed by common protocol signals generated by the FCTS. All de-randomizing event buffers function as

FIFOs capable of storing a fixed number of events. During normal operation, analog signal processing, digitization, and data readout occur continuously and simultaneously.

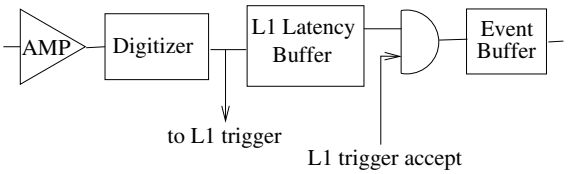

Figure 2.29: Front-End Electronics. Analog signals arrive from the left, proceed conditionally through the indicated steps and are injected into the remainder of the data acquisition system.

Since many of the front-end circuits are totally inaccessible or access requires significant downtime, stringent requirements were placed on reliability. Most components underwent comprehensive MTBF (mean time between failure) studies. A burn-in procedure was followed for all circuits prior to installation with the goal of minimizing initial failure rates.

2.9.2 Trigger

The trigger system operates as a sequence of two independent stages, the second conditional upon the first. The L1 trigger is performed first at the machine crossing rate. Its goal is to sufficiently reduce that rate to a level acceptable for the L3 software trigger which runs on a farm of commercial processors.

The L1 trigger is optimized for simplicity and speed. It consists of a pipelined hardware processor. It is designed to provide an output trigger rate of $\lesssim$ 2 kHz. The L1 trigger selection is based on a reduced data set from the DCH, EMC and IFR. Its maximum L1 response latency for a given collision is 12 μs. Based on both the complete event and L1 trigger information, the L3 software algorithms select events of interest allowing them to be transfered to mass storage for further analysis. The L3 output rate is administratively limited to 120 Hz so as to not overload the downstream processing. The trigger architecture is designed to accommodate a *Level 2* should unexpected background conditions demand higher performance in

the future.

BABAR has no fast counters for triggering purposes, and bunch crossings are nearly continuous at 4 ns. Dedicated L1 trigger processors receive data which is continuously clocked in from the DCH, EMC and IFR detector subsystems. The L1 trigger processor produces a clocked output to the FCTS at 30 MHz, the time granularity of resultant L1 Accept signals. The arrival of an L1 Accept signal by the data acquisition system causes a window of each subsystem's L1 Latency Buffer to be read out. This window is about 500 ns wide for the silicon vertex tracker and $4 - 16$ μs wide for the calorimeter. Absolute timing information for the event, i.e., associating an event with a particular beam crossing, is determined offline. The ingredients for this calculation include the timing distributions for drift chamber hits within a track segment, waveforms from the electromagnetic calorimeter and accelerator timing fiducials.

2.9.3 Data Acquisition and Online Computing

The data acquisition and computing systems are responsible for the transport of event data from the detector FEE circuits all the way to mass storage with a minimum of deadtime and is shown schematically in Figure 2.30. These systems interface with the trigger systems and enable specialized modes of operation, such as calibration and testing. Other parts of these systems provide for the control and monitoring of the detector and supporting facilities.

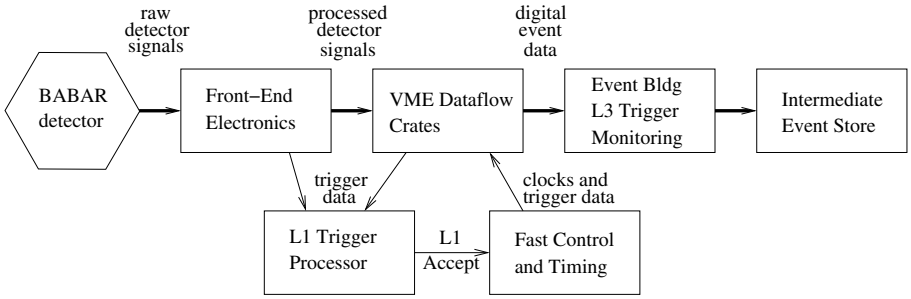

Figure 2.30: Data acquisition schematic.

Hardware

The data acquisition system hardware consists of VME crates, specialized VME-based processors called Readout Modules (ROMs) [reference], the Fast Control and Timing System, a UNIX processor farm, various server machines and an Ethernet network. A ROM consists of a commercial single board computer , event buffers, an interface to the FCTS, and a custom *Personality Card* which connects with the FEE circuits via 1.2 Gbps fiber optic cables. The ROM provides the standard interface between the detector specific front-end electronics, the FCTS, and the event builder. There are about 157 ROMs in the system which are located in 19 physical VME crates that represent 24 logical crates by virtue of segmented backplanes. The FCTS system consists of a VME crate plus individual Fast Control Distribution Modules in each of the data acquisition VME crates.

Detector monitoring and control is accomplished via a standard set of components, including a VME crate, a Motorola MVME177 single-board computer, and various other VME modules [this needs to be expanded to a small list of VME modules]. With the exception of the solenoid magnet and gas systems, which have their own specialized control and monitoring, all other *BABAR* elements plug into this system.

The online computing system relies on a complex of workstation consoles and servers with 0.8 TBytes of attached storage, all interconnected with switched 100 Mbps and 1 Gbps Ethernet networks. Multiple Gbit Ethernet links connect the experimental hall with the SLAC computing center.

Online Dataflow

The Online Dataflow software connects, controls, and manages the flow of data in the data acquisition hardware while incurring almost no dead time. This code is divided between embedded processors in the ROMs which run the VxWorks real-time operating system and UNIX processors running the Solaris operating system. Dataflow provides: a) configuration and read-out of the FEE over fiber links to the ROMs; b) data transport, buffering and event building from the ROMs to the OEP farm; c) masking and prescaling of L1 triggers; and d) partitioning into multiple, independent data acquisition systems. Additional code in the ROMs, supplied by the detector

systems, performs gain and pedestal correction, data sparsification, feature extraction and data formatting. Data from electronics calibrations are accumulated in the ROMs, the channel response functions evaluated, the results compared to reference data and subsequently applied in feature extraction. Calibration data is stored in a *Conditions Database*.

Online Event Processing

The On-line Event Processing receives and processes data from the *DataFlow* event builder on each of the 32 UNIX processors. In particular, OEP orchestrates the following tasks: a) L3 trigger algorithms; b) "fast monitoring" to assure data quality; and c) logging the selected events to disk. Logging involves a process to merge the multiple data output streams to a single file.

Online Prompt Reconstruction

Bridging the online and offline worlds is OPR [21]. This system reads raw data recorded to disk by OEP and, operating on farm of 150 Unix processors, selects physics events, performs complete reconstruction, performs a of "rolling" calibration, collects extensive monitoring data for quality assurance and writes the result into an object database. A "rolling" calibration is the generation of reconstruction constants during normal event processing which are then applied to the processing of subsequent data.

Online Detector and Run Control

The ODC system controls and extensively monitors the electronics and environment of the detector and assures the safety of the detector. Its implementation is based on EPICS [20], providing detector-wide standardization for the control and monitoring, diagnostics and alarm handling. ODC also provides communication with PEP-II and the magnet control system. Monitoring data are archived in the *Ambient Database*.

The ORC system ties together the various components of the online system and provides the operator with a single graphical interface to control the detector operation. Complex configurations are stored in a *Configuration Database*; keys to the configuration used for any run is stored along with

the data. The Event, Ambient, Conditions and Configuration Databases are implemented in an object database [22].

2.10 Impact of Beam-Generated Background on *BABAR*

Beam-generated backgrounds affect the detector in multiple ways. They cause radiation damage to the detector components and the electronics and thus may limit the lifetime of the experiment. They may also cause electrical breakdown and damage or generate large numbers of extraneous signals leading to problems with bandwidth limitations of the data acquisition system and with event reconstruction. The event reconstruction is affected both by degraded resolution as well as by losses in efficiency.

The impact of the beam-generated background on the lifetime and on the operation of the different detector systems varies significantly. Table 2.5 lists the limits on the instantaneous and integrated background levels in terms of the total dose and instantaneous observables. These limits are estimates derived from tests and/or experience in earlier experiments. For each detector system an annual radiation allowance has been established taking into account the total estimated lifetime of the components and the expected annual operating conditions. The typical values accumulated for the first year of operation are also stated in the table.

Systematic studies of background rates were performed with stable stored beams. Measurements of the current-dependence of the backgrounds were carried out for single beams, two beams not colliding, and colliding beams with the goal to identify the current background sources, to develop schemes of reducing these sources and to extrapolate to operation at higher luminosity. These experimental studies were complemented by Monte Carlo simulations of beam-gas scattering and of the propagation of induced showers in the detector. The studies show that the relative importance of the single-beam and luminosity background contributions varies, as illustrated in Figure 2.31. Data for the IFR are not shown because this system is largely insensitive to beam-generated backgrounds, except for the outer layer of the forward endcap due to insufficient shielding of the external beam line components.

The experience of the first year of operation and the concern for future

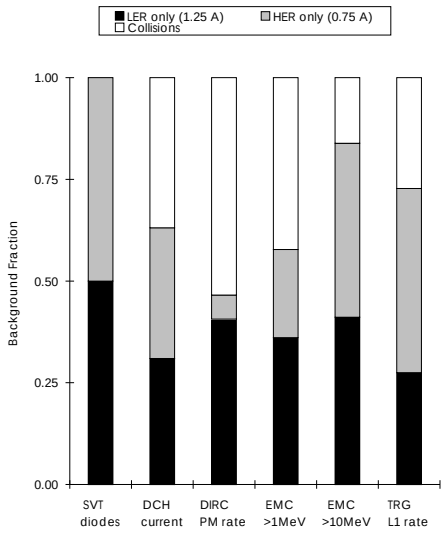

Figure 2.31: Fractional steady-state background contributions in *BABAR* detector systems, measured for single beams and colliding beams under stable conditions ($I^+ = 1.25\ A$, $I^- = 0.75\ A$, $L = 2.3 \times 10^{33}\,\mathrm{cm}^{-2}\,\mathrm{s}^{-1}$).

operation for each of the detectors are summarized as follows.

- The most significant concern for the SVT with regard to machine background is the integrated radiation dose. The instantaneous and integrated dose rates in the radiation protection diodes are representative, to within about a factor of two, of the radiation doses absorbed by the SVT modules. The exposure in the horizontal planes is an order of magnitude larger than elsewhere, averaging 15-25 mRad/s during stable beam operation. The worst integrated dose is 450 kRad, 30% below the allowance, giving confidence that the SVT can be operated several more years (see Figure 4.13).

- For the DCH, the currents on the wires are the main concern, both because of the limited capacity of the HV power supplies and the effect of wire aging. The currents drawn are approximately uniformly distributed among the 44 HV supplies (there is one (two) for every quadrant of superlayers 2-10 (superlayer 1). Consequently, the total current limit is close to the sum of the limits of the individual supplies.

During stable operation the total chamber current is 200-300 μA. However, radiation spikes can lead to currents that occasionally exceed the limit of 1000 μA, causing HV supplies to trip. Other background effects are measured to be well below the estimated lifetime limits and thus not a serious issue at this time. The average wire occupancy has not exceeded 1-2% during stable operations, but the extrapolation to future operation at higher luminosity and currents remains a major concern.

- The DIRC quartz bars were tested up to doses of 100 kRad without showing any measurable effects and thus radiation damage is not a concern. The present operational limit of the DIRC is set by the TDC electronics which induces significant dead time at rates above $200 - 300$ kHz, well above the stable-beam rate of 110 kHz in well shielded areas. Roughly half the current rate originates from radiative Bhabha scattering. The counting rate is due to debris from electromagnetic showers detected the water-filled stand-off box. Efforts are underway to improve the shielding of the stand-off box.

- The lifetime of the EMC is set by the reduction in light collection in the CsI crystals due to radiation damage. The cumulative dose absorbed by the EMC is measured by a large set of RADFETs distributed over the barrel and endcap. The absorbed dose increases approximately linearly with the integrated luminosity. The highest dose is observed in the innermost ring of the endcap, close to 200 Rad, while the barrel crystals accumulated about 80 Rad. The observed reduction in light collection of 10-15% in the worst place, and 4-7% in the barrel, is consistent with expectation (see chapter 7).

  The energy resolution is dependent on the single crystal readout threshold, currently set at 1 MeV. During stable-beam conditions the average crystal occupancy is 16%, with 10 % originating from electronics noise in the absence of any energy deposition. The spectrum of photons observed in the EMC from the LER and HER is presented in Figure 2.32. The HER produces a significantly harder spectrum. The occupancy increases significantly at smaller polar angles, in the forward endcap and the backward barrel sections, and in the horizontal

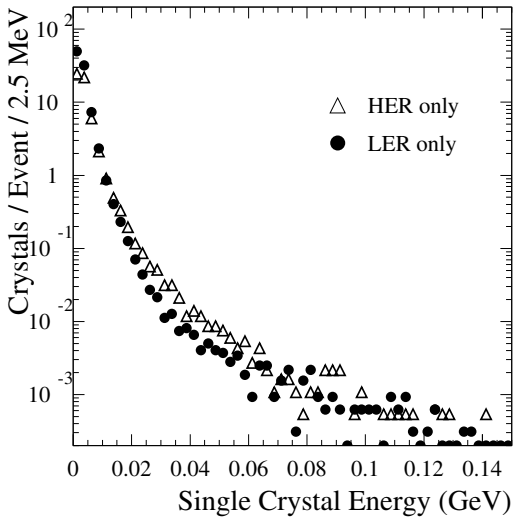

Figure 2.32: The energy spectrum of photons recorded in the EMC by random triggers with single beams at typical operating currents, LER at 1.1 A and HER at 0.7 A. The electronic noise has been subtracted.

plane. The rate of photons above the threshold of 1 MeV and 10 MeV is shown in Figure 2.33 as a function of beam currents for both single and colliding beams. The rate increase is approximately linear with the single beam currents. The data recorded with separated beams produce backgrounds that are consistent with those produced by single beams. For colliding beams, there is an additional flux of photons originating from small angle radiative Bhabha scattering. This effect is larger for low energy photons and thus it is expected that at higher luminosities the low energy background will raise the occupancy and thereby limit the EMC energy resolution.

- During stable-beam operation the typical L1 trigger rate is below 1 kHz, about a factor of two below the data acquisition bandwidth limit of about 2–2.5 kHz. Experience shows that background bursts and other rate spikes can raise the data volume by as much as a factor two and thus it is necessary to aim for steady state rates significant below the stated limit. For the L1 trigger, the dominant DCT triggers are due to particles generated by interactions in the vacuum flanges

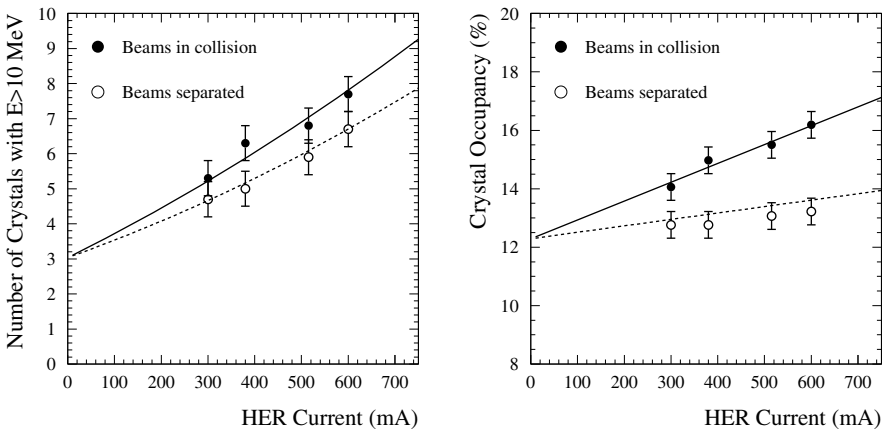

Figure 2.33: Rates in the EMC as a function of the HER current for a fixed LER current of 1.1 A, both for separated and colliding beams; a) the single crystal occupancy for thresholds of 1 MeV and b) the number of crystals with a deposited energy greater than 10 MeV. The solid curves represent a fit to the colliding beam data, the dashed curves indicate the sum of data recorded for single beams.

and the B1 magnets (see Figure XX in section 10), it is most pronounced in the horizontal plane. At present, the HER background is twice as high as that of the LER, and the luminosity trigger contributes less than half of the combined LER and HER single beam triggers.

Over the coming years, it is expected that the luminosity will rise to $1.5\ 10^{34}\,\mathrm{cm}^{-2}\,\mathrm{s}^{-1}$. As a result, the single beam backgrounds will rise and the projected luminosity background will exceed, or at best remain comparable to, the beam-gas contribution. For instance, the occupancy in the EMC is expected to more than double and the average L1 trigger will increase to 2 kHz (see Figure 2.34). In fact, the occupancy in all systems, except the SVT and IFR, will probably reach levels that are likely to impact the resolution and reconstruction efficiency.

Measures are being prepared to reduce the impact of machine-related background on *BABAR*, among them the addition of localized shielding against shower debris, especially for the DIRC standoff-off box, as well as upgrades to the DCH power supply system and to the DIRC TDC electronics. With

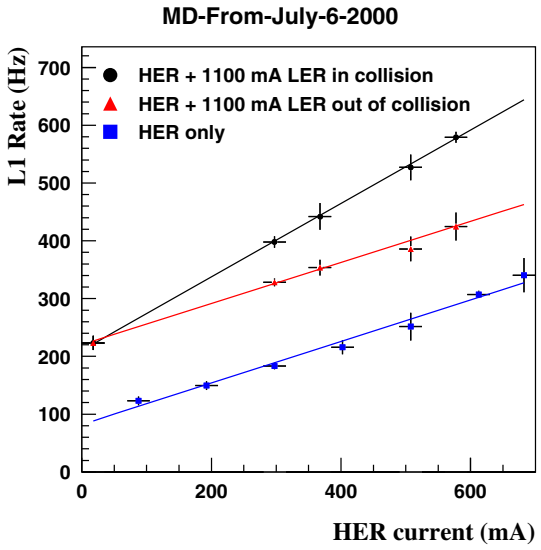

Figure 2.34: The L1 trigger rate as a function of the HER current for single beam only, for both beams, separated and colliding (with a LER current of 1.1 A).

the expected increase in LER current and luminosity both the single beam and the luminosity generated L1 rates are expected to increase. The DCH trigger is being upgraded to improve the rejection of background tracks originating from $\pm$ 20 cm from the IP. In addition, the data acquisition and data processing capacity will need to be expanded to meet the demands of higher luminosity. Beyond that, all efforts are being made to reduce the sources of background, in particular, vacuum pumps and masks are being added in critical regions upstream of the interaction point.

Detector system	Limiting factor and impact	Operational limit	First-year typical
SVT sensors & electronics	Integrated dose: radiation damage	2 MRad	0.33 MRad (hor.-plane modules) 0.06 MRad (other modules)
SVT sensors	Instantaneous dose: diode shorts	1.5 Rad/ms	N/A
DCH: electronics	Integrated dose: radiation damage	20 kRad	$\leq$ 100 Rad
DCH: wire current	Accumulated charge: wire aging	100 mC/cm	8 mC/cm
DCH: total current	HV system limitations	1000 μA	250 μA (steady-state)
DIRC photo tubes	Counting rate: TDC dead time	200 kHz	110 kHz (steady-state, well-shielded sector)
EMC crystals	Integrated dose: radiation damage	10 kRad	0.25 kRad (worst case)
L1 trigger	Counting rate: DAQ dead time	2 kHz	0.7 kHz (steady-state)

Table 2.5: *BABAR* background tolerance. Operational limits are expressed either as lifetime limits (radiation-damage and aging-related quantities), or in terms of instantaneous observables (DCH current, DIRC and L1-trigger rates).

Chapter 3

Silicon Vertex Tracker

The SVT (Silicon Vertex Tracker) is the most relevant detector for the measurement of time dependent *CP* asymmetries in *BABAR*. It has been designed to provide precise reconstruction of decay vertices and charged particle reconstruction, taking into account physics requirements and the constraints imposed by the PEP-II interaction region.

3.0.1 Physics requirements

The finite precision in the reconstruction of the z difference must must degrade the error on the *CP* asymmetry by less than 10%. In order to achieve this the resolution is required to be better than 80 μm on each B decay vertex.

A resolution in the transverse plane of about 100 μm is required in order to separate secondary decay vertices such as D mesons decays.

The SVT must provide stand-alone tracking for particles with transverse momentum less than 120 MeV/c, the minimum that can be reliably measured in the drift chamber alone. This feature is fundamental for the identification of slow pions from D^* meson decays: a tracking efficiency of 70% or more is required for tracks with a transverse momentum in the range 50–120 MeV/c. This also means that the material traversed by particles must be minimized.

3.0.2 PEP II constraints

Additional constraints are imposed by the storage rings. These constraints can be briefly summarized as follows:

The geometrical layout of the SVT is constrained by the limited amount of space available. The SVT is located inside the long support tube, that extends all the way through the detector. To maximize the angular coverage, the SVT must extend down to 350 mr (17.2°) in polar angle from the beamline in the forward direction. The region at smaller polar angle is occupied by the B1 permanent magnets. In the backward direction, it is sufficient to extend the SVT sensitive area down to 30°.

The SVT must withstand 2 MRad of ionizing radiation. A radiation monitoring system capable of aborting the beams is required. The expected radiation dose at the design luminosity is 240 kRad/yr in the horizontal plane immediately outside the beam pipe (where the highest radiation is concentrated), and 33 kRad/yr on average otherwise.

Reliability and robustness is essential: all components of the SVT inside the support tube must have long mean-time-to-failure, because the time needed for any replacement is estimated to be 4-5 months. Redundancies must be built in whenever possible.

The SVT must be cooled to remove the heat generated by the electronics. In addition, it must operate in a magnetic field.

The relative position of the individual silicon sensors must be stable over long time periods. The assembly must allow for relative motion of the support structures with respect to the B1 magnets. This feature is also necessary to sustain an earthquake of moderate intensity.

The choice of a Silicon Vertex Tracker made of five layers of double-sided silicon strip sensors with spatial resolution, for perpendicular tracks, of 10-15 μm in the three inner layers and about 40 μm in the two outer layers fullfills the physics requirements: the inner three layers perform the impact parameter measurements, while the outer ones are necessary for pattern recognition and low p_T tracking.

3.1 Silicon sensors

The SVT sensors [32] are made of 300 μm thick double-sided silicon strip devices. They were designed at INFN Pisa and Trieste (Italy) and fabricated commercially. They are built on high-resistivity (6-15 kΩ-cm) n-type substrates with p^+ strips and n^+ strips on the two opposite sides. The insulation of the n^+ strips is provided by individual p-stops, in such a way as to achieve an inter-strip resistance greater than 100 MΩ at operating bias voltage, normally about 10 V above the depletion voltage. Typical depletion voltage is in the range 25-35 V. On both sides the strips are biased with polysilicon resistors (4-20 MΩ) to insure the required radiation hardness, keeping the voltage drop across resistors and the parallel noise as low as possible. Strips are AC-coupled to electronics via integrated decoupling capacitors, whose capacitance depends on the sensor shape, but that is always greater than 14 pF/cm. The sensors were designed to maximize the active area, which extends to within 0.7 mm of the physical edges. Another design goal was to control the inter-strip capacitance, values between 0.7 pF/cm and 1.1 pF/cm were obtained for the various sensor shapes. To achieve the required spatial resolution, while keeping the number of readout channels as low as possible, most of the modules have a floating strip between two readout strips.

The leakage currents, because of the excellent performance of the manufacturing process, were as low as 50 nA/cm^2 on average, measured at 10 V above depletion voltage. The silicon sensor parameters have been measured after irradiation with ^{60}Co sources. Apart from an increase in the inter-strip capacitance of about 12% during the first 100 kRad, the main effect was an increase of the leakage current of 0.7 μA/cm^2/MRad. However, in a radiation test performed in a 1 GeV electron beam, an increase in leakage current of about 2 μA/cm^2/MRad, and a significant shift in the depletion voltage, dependent on the initial dopant concentration, were observed. A shift of about 8-10 V was seen for irradiation corresponding to a dose of approximately 1 MRad. These observations indicate significant bulk damage caused by energetic electrons. Due to the change in depletion voltage, the SVT sensors could undergo type inversion after about 1-3 MRad. Preliminary tests show that the sensors continue to operate properly after

Layer/ view	C_{input} (pF)	R_{series} (Ω)	Noise, calc. (elec)	meas. (elec)
1 z	6.0	40.	550	880
1 ϕ	17.2	164.	990	1200
2 z	7.2	48.	600	970
2 ϕ	18.4	158.	1030	1240
3 z	10.5	70.	700	1180
3 ϕ	26.8	230.	1470	1440
4 z	16.6	104.	870	1210
4 ϕ	33.6	224.	1380	1350
5 z	16.6	104.	870	1200
5 ϕ	39.7	265.	1580	1600

Table 3.1: Electrical parameters of the SVT, shown for the different layers and view. C_{input} refers to the total input capacitance, R_{series} is the series resistance. The amplifier peaking time is 200 ns for layers 1–3 and 400 ns for layers 4–5.

type inversion [33]. Studies of the behavior of SVT modules as a function of radiation dose continue.

3.2 SVT Layout

The SVT detector are organized in five layers of double-sided silicon strip sensors: a photograph is shown in Figure 3.1. The strips on the two sides are oriented orthogonally to each other: the ϕ strips run parallel to the beam and the z strips are oriented transversely to the beam axis.

The modules are made of several rectangular silicon sensors, of different sizes, that are assembled in a plane. The modules are divided electrically into two half-modules, which are read out at the ends. Two identical trapezoidal sensors must be added (one each at the forward and backward ends) to form the arch modules. To satisfy the different geometrical requirements of the five SVT layers, six different sensor shapes are required (five rectangular and one trapezoidal). The half-modules are given mechanical stiffness by

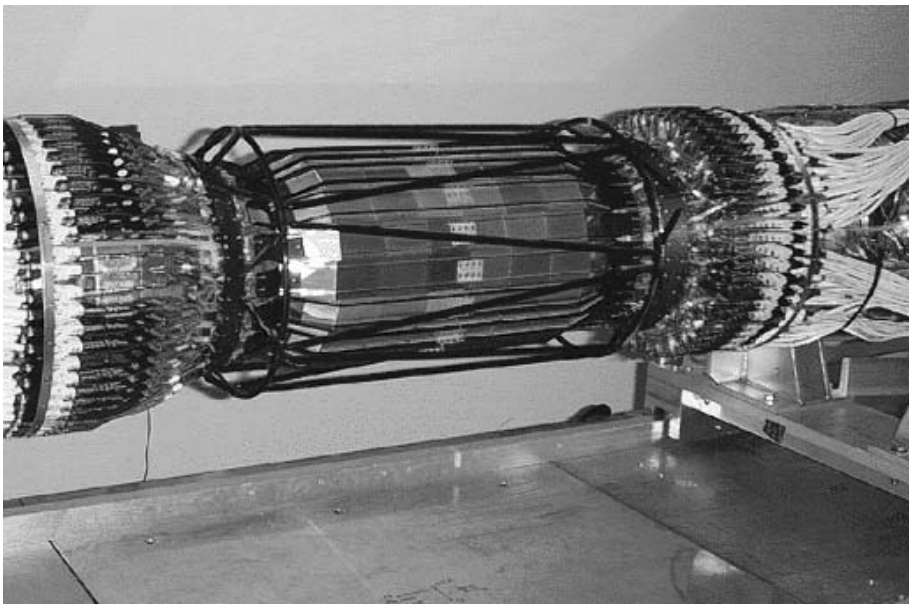

Figure 3.1: Fully assembled Silicon Vertex Tracker. The silicon sensors of the outer layer are visible, as is the carbon-fiber space frame (black structure) that surrounds the silicon.

means of two carbon fiber/kevlar ribs, which are visible in Figure 3.2. ϕ strips of the same half-module are electrically connected with wire bonds. This results in a total strip length up to 14 cm in the inner layers and up to 24 cm in the outer layers.

The modules of the inner 3 layers are straight, while the modules of layers 4 and 5 are arch-shaped (Figures 3.2 and 3.3), This arch design was chosen to minimize the amount of silicon required to cover the solid angle, while increasing the crossing angle for particles near the edges of acceptance. A photograph of an outer layer arch module is shown in in Figure 3.4.

The signals from the z strips are brought to the readout electronics using fanout circuits consisting of conducting traces on a thin (50 μm) insulating Upilex substrate. In layers 1 through 3 each z strip is connected to its own preamplifier channel, while in layers 4 and 5 the number of z strips on a half module exceeds the number of electronics channels available, requiring that pairs of z strips are electrically connected (ganged) to a single electronics channel. The length of a z strip is about 5 cm (no ganging) or 10 cm (two strips connected). The ganging introduces an ambiguity on the z coordinate

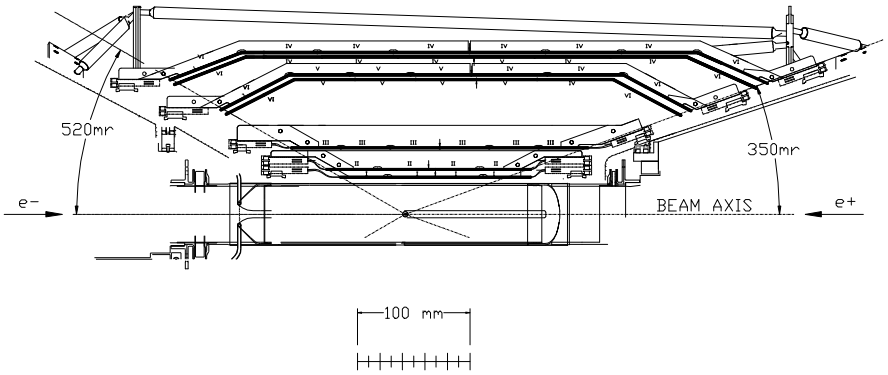

Figure 3.2: Schematic view of SVT: longitudinal sections.

measurement, which must be resolved in the pattern recognition procedure. The total number of readout channels is approximately 145,000.

The inner modules are tilted in ϕ by 5°, allowing an overlap region between adjacent modules, a feature that is very useful for the alignment. The outer modules cannot be tilted, because of the arch geometry. To avoid gaps and to have a suitable overlap in ϕ, layers 4 and 5 are divided into two sub-layers (4a, 4b, 5a, 5b) placed slightly different radii. The relevant geometrical parameters of each layer are summarized in Table 3.2.

In order to minimize the material in the detector acceptance region, the readout electronics are mounted entirely outside the active detector volume. The forward electronics must be mounted in the 1 cm space between the 350 mr stay-clear space and B1 magnet. This implies that the hybrids carrying the front-end chip must be positioned at an angle of 350 mrad relative to the sensor for the inner layers, and at an even larger angle for the outer ones (Figure 3.3). In the backward direction the available space is larger and the inner layer electronics can be placed in the sensor plane, allowing a simplified assembly procedure.

The module assembly and the mechanics are quite complicated, especially for the arch modules, and are described in detail elsewhere [31]. In this write-up we recall only that the SVT support structure (Figure 3.1) is a rigid body made from two carbon-fiber cones, connected by a "space-frame", also made of carbon-fiber epoxy laminate. This structure is attached to the B1 magnets by a set of gimbal rings, in such a way as to allow for rela-

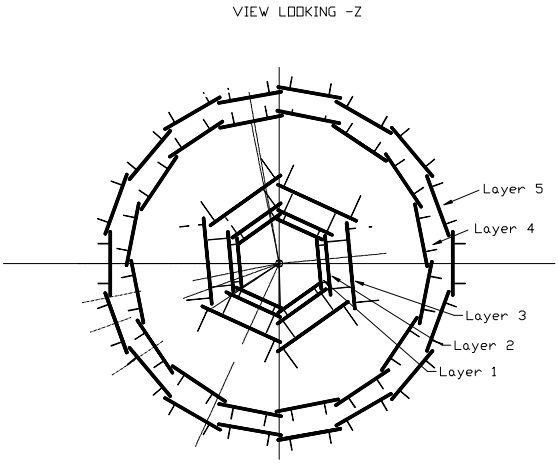

Figure 3.3: Schematic view of SVT: transverse sections.

Layer/ view	Radius (cm)	Readout pitch (μm)	Floating strips	Strip length (mm)
1 z	3.2	100	1	40
1 ϕ	3.2	50-100	0-1	82
2 z	4.0	100	1	48
2 ϕ	4.0	55-110	0-1	88
3 z	5.4	100	1	70
3 ϕ	5.4	110	1	128
4 z	9.1-12.7	210	1	104
4 ϕ	9.1-12.7	100	1	224
5 z	11.4-14.4	210	1	104
5 ϕ	11.4-14.4	100	1	265

Table 3.2: Geometrical parameters of the SVT, for each layer and view. "Floating strips" refers to the number of strips between readout strips. Note: parts of the ϕ sides of layers 1 and 2 are bonded at 100 μm and 110 μm pitch, respectively, with one floating strip. Strip length for layers 4 and 5 z takes into account the ganging.

Figure 3.4: Photograph of an arch module.

tive motion of the two B1 magnets while fixing the position of the SVT relative to the forward B1 and the orientation relative to the axis of both B1s. Note that the SVT/B1 magnet/support tube structure is supported independently of the rest of the *BABAR* apparatus, leading to the possible movements between the SVT and the rest of *BABAR*. Precise position monitoring of the beam interaction point is necessary, this is described in section 3.4.

The total active silicon area is 0.96 m^2 and the material traversed by particles is minimal. The geometrical acceptance of SVT is 92% of the solid angle in the center-of-mass system.

3.3 SVT Components

A block diagram of SVT components is shown in Figure 3.5. The basic components of the detector are the silicon sensors, the fanout circuits, the front

end electronics and the data transmission system. Each of these components is discussed in the following sections.

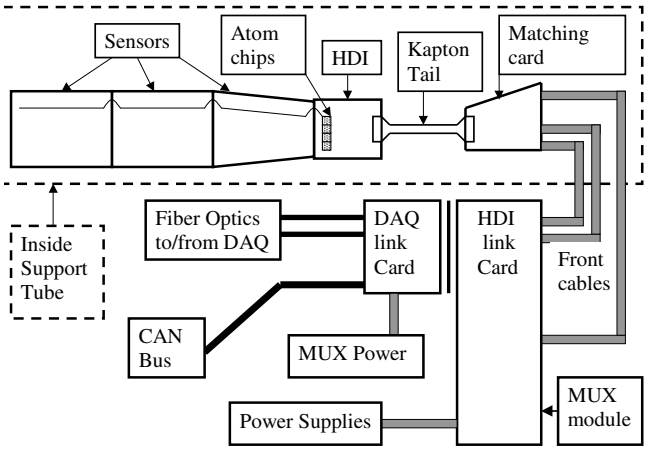

Figure 3.5: Schematic block diagram showing the different components of the SVT.

3.3.1 Fanout circuits

The fanout circuits, which route the signals from the strips to the electronics, have been designed to minimize the series resistance and the inter-strip capacitance. As described in [34], a trace on the fanout has a series resistance about 1.6 Ω/cm, an inter-strip resistance > 20 MΩ, and an inter-strip capacitance < 0.5 pF/cm. The electrical parameters of the final assembly of sensors and fanouts (known as DFAs: Detector Fanout Assemblies) are summarized in Table 3.1. Due to the different strip lengths, there are large differences between the inner and the outer layers. Smaller differences are also present between the forward and backward halves of the module, that are of different lengths.

3.3.2 Front end electronics

The electrical parameters of a DFA and the general *BABAR* requirements are the basic inputs that drove the design of the SVT front-end chip: the

ATOM (A Time-Over-Threshold Machine). In particular, the front-end IC had to cope with the following requirements:

1. signal to noise ratio > 15 for minimum ionizing particle (MIP) signals for all modules;
2. signals from all hit strips must be retained, in order to improve the spatial resolution through interpolation, while keeping the number of transmitted hits as low as possible. 'hit" means a deposited charge > 0.95 fC, corresponding to 0.25 MIP (MIP = the average charge deposited by a minimum ionizing particle) ;
3. the amplifier must be sensitive to both negative and positive charge;
4. the peaking time must be programmable, with a minimum of 100 ns (in layers 1 and 2, because of the high occupancy), up to 400 ns (outer layers, with high capacitance)
5. capability to accept random triggers with a latency up to 11.5 μs and a programmable jitter up to ± 1 μs, without dead time;
6. radiation hardness (requirement 3.0.2 above);
7. small dimensions: 128 channels in a 6.2 mm wide chip.

These requirements are fully satisfied by the ATOM chip [35], which is depicted schematically in Figure 3.6. The linear analog section consists of a charge-sensitive preamplifier followed by a shaper: two values (LOW with a gain of 200 mV/fC and HIGH with 300 mV/fC) are digitally selectable, while the gain dispersion across channels of one chip is about 5 mV/fC. Signals are presented to the time-over-threshold (ToT) comparator, whose threshold is generated and controlled by a DAC. The signals above threshold induce at the comparator output a logic signal whose width, the ToT, is related to the collected charge by a quasi-logarithmic relationship. This design choice effectively retains the analog charge information with only 4 bits. This is not, however, the limiting factor to the measurement of the spatial resolution. The ToT is digitized by comparison with a reference clock (30 MHz) and the resulting stream of pulses is stored into a 193 location buffer, to compensate for the trigger latency and jitter. Upon receipt of a first level trigger, the

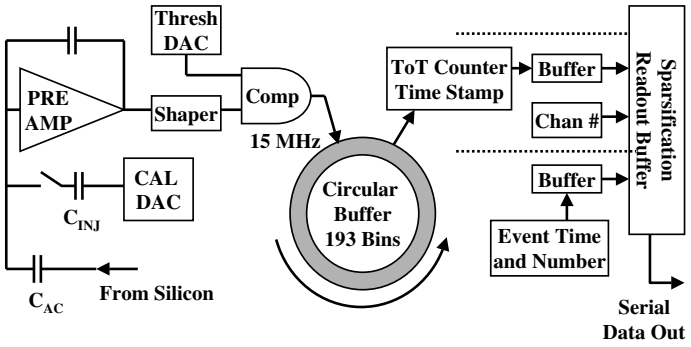

Figure 3.6: Schematic diagram of the AToM front end IC.

ATOM peaking time	Noise Charge at zero Capacitance	Noise slope
100 ns	380 e^-	40.9 e^-/pF
200 ns	280 e^-	33.9 e^-/pF
400 ns	220 e^-	25.4 e^-/pF

Table 3.3: ATOM chip Equivalent Noise Charge (ENC) parameters at different peaking times

ToT is retrieved from the latency buffer, associated to a 5 bit time stamp and stored into one of four buffers. The output data (the 4 bits of the ToT value, the 5 bits for the time stamp and 7 bits for the strip address) are formatted, serialized and delivered upon the receipt of a readout command. The IC also contains a test charge injection circuit, controlled by the calibration DAC, and by the command decoder and control register. The typical noise behavior of the ATOM, as described by the equivalent noise charge (ENC) of the linear analog section is given in Table 3.3.2.

The power consumption of the IC is about 4.5 mW/channel. Radiation hardness was measured up to 2.4 MRad of ^{60}Co irradiation. At that dose, a decrease of 20% in the charge gain has been observed, with a noise increase of less than 15%.

With the parameters of Tables 3.1 and 3.3.2, it is possible to perform a calculation of the expected noise in the various SVT modules, taking into account that the shot noise, due to the sensors leakage current fluctuations is negligible. The results of such a calculation are shown in Table 3.1, together with the measured average values for the selected modules. The agreement is satisfactory, and the maximum average noise is 1600 electrons, leading to a signal to noise ratio > 15.

The Atom IC's are housed on thick-film double-sided hybrid circuits, known as High Density Interconnects (HDIs), which are fabricated on 1.2 mm thick AlN substrate [36]. The chips and the other discrete components are mounted on both sides of the hybrid substrate to read out the ϕ and z sides of the half-modules. The electronics on each side of the HDI is biased through a floating power supply system, in such a way as to guarantee a small voltage drop (< 1 V) across the detector decoupling capacitors.

3.3.3 Data transmission

The digitized signals are transmitted from the AToM chips through a thin kapton cable ("tail") to the matching cards, from where they are routed to more conventional cables. Just outside the *BABAR* detector signals are multiplexed by the MUX modules, converted into optical signals and transmitted to the ROMs. The MUX also receive digital signals from the DAQ via a fiber optical connection. The SVT is interfaced to the *BABAR* online detector control and monitoring system via the industry standard CAN bus. Details on SVT data trasmission system and DAQ can be found in [37]. Power to SVT modules (silicon sensor bias voltage and ATOM low voltages) is provided by a CAEN A522 power supply system.

3.4 Monitoring

To identify immediately any operational problems, the SVT is integrated in the *BABAR* control and monitoring system, based on the Experimental Physics and Industrial Control System (EPICS). Major concerns for SVT monitoring are temperature and humidity, mechanical position and radiation dose. Calibration procedures are also discussed in this section.

3.4.1 Temperature and humidity monitors

The total power dissipation the SVT modules is about 350 W, mainly dissipated in the ATOM chip. External cooling is provided by chilled water at 8°C. In addition, humidity is kept down by a stream of dry air in the support tube.

Since excessive temperature can permanently damage the front-end electronics, temperature monitoring is very important to the safe operation of the SVT. Termistors are located on the HDIs (for the measurements of front-end electronics temperature), around the SVT, along the cooling systems and in the electronics (MUX) crates. All systems are able to monitor the absolute temperature to 0.2° C and relative changes of 0.1°C. Additionally, a series of humidity sensors are employed to monitor the performance of the dry nitrogen system. The temperature and humidity monitors also serve as an interlock to the HDI power supplies.

3.4.2 Position monitoring sensors

The relative alignment of the two tracking systems (DCH and SVT) must be monitored as well as possible, in any case much better than the spatial resolution of the outermost SVT layer (40 μm). This can be done on an hourly basis with charged particles from Bhabha and $\mu^+\mu^-$ events with a precision of approximately 10 μm. To detect sudden unexpected movements, it is important to monitor the SVT position on a much faster time scale. This is achieved by a system of capacitive sensors that measure the position of the SVT with respect to the PEP-II B1 magnets and the position of the support tube containing SVT with respect to the drift chamber.

An example of the understanding that can be achieved by the monitoring systems is given in Figure 3.7. The relative DCH-SVT horizontal position during a period of 6 days, as measured by the capacitive sensors, is shown. This curve is compared with the temperature, measured by the thermistors around the SVT: a correlation is evident, thus explaining the diurnal movement. The displacement measurement performed by the capacitive sensors is also confirmed by the measurements obtained with Bhabha and dimuon events, as shown in Figure 3.7(b).

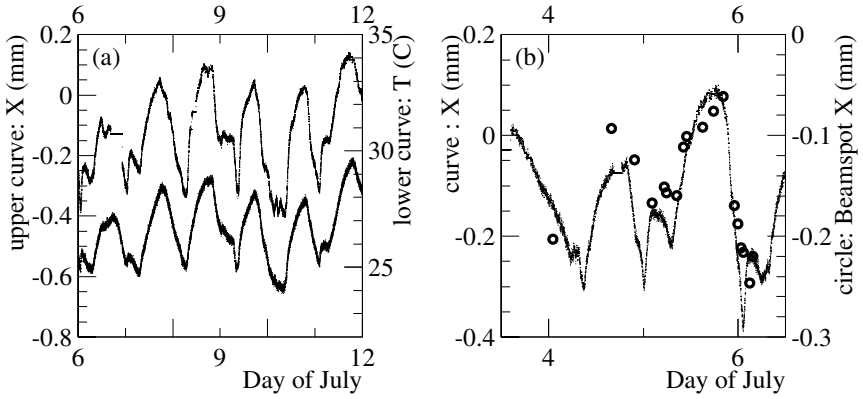

Figure 3.7: (a) Diurnal horizontal motion of the drift chamber relative to the SVT as measured with the capacitive sensors (upper curve) and temperature near the detector (lower curve) as a function of time, for six days in July 1999. (b) Horizontal motion measured with the capacitive sensors (curve) and mean x coordinate of the collision point (circles) measured with e^-e^- and $\mu^+\mu^-$ events for a three day period in July 1999.

3.4.3 Radiation monitors

Radiation monitoring is extremely important to insure the SVT does not exceed its radiation budget, which could cause permanent damage to the device. To date, the measured radiation absorbed by the SVT is well within the allowed budget. The monitoring of radiation dose to the SVT is discussed in detail in section 4.

3.5 Data analysis and performance

After a brief summary of the status of SVT defects incurred during construction, assembly and operation, this section describes the reconstruction of raw data into physics-related quantities such as charged track trajectories. SVT alignment procedures are also discussed.

3.5.1 Defects

Due to a series of minor mishaps incurred during the installation of the SVT, several of the SVT modules were damaged and are currently not functioning. There is no single primary failure mode, but rather a mixture of defective connectors, mis-handling during installation and not-fully-understood problems on the front-end electronics hybrid. There has been no module failure due to radiation damage. A total of 9 readout sections (which corresponds to one side of a half-module) out of 208 are not functioning. It should be noted that due to the redundancy afforded by the five layers of the SVT, the presence of the defective modules has minimal impact on physics.

In addition, it is estimated that there are individual channel defects, of various types, at a level of about 1%. Calibrations reveal an increase in the number of defective channels at a rate of less than 0.2%/year.

3.5.2 Cluster and hit reconstruction

The average occupancy, in a time window of 1 μs, of the SVT under normal running conditions is about 3% for the inner layers, with a significant azimuthal variation due to beam-induced backgrounds, and $< 1\%$ for the outer layers, where noise hits dominate. Figure 3.8 shows the typical occupancy as a function of chip number (equivalent to azimuthal angle, in this case) for layer 1, ϕ side. In the inner layers, the occupancy is dominated by machine backgrounds, which are significantly higher in the horizontal plane, seen in the plot as the peaks near chip numbers 3 and 25, approximately.

The first step of the reconstruction program consists in discarding out-of-time channels. A time correction, the time between the passage of the particle and the time the shaper exceeds threshold, is performed, after which hits with times more than 200 ns from the event time (determined by the drift chamber) are discarded. The loss of real hits from this procedure is negligible. The resulting in-time hits are then passed to the cluster finding algorithm. First, the charge pulse height (Q) of a single pulse is calculated from the ToT value. In a first pass, clusters are formed grouping adjacent strips with consistent times. A second pass is then performed, where clusters separated by just one strip are merged into one cluster. The two original clusters plus the merged cluster are made available to the pattern recognition

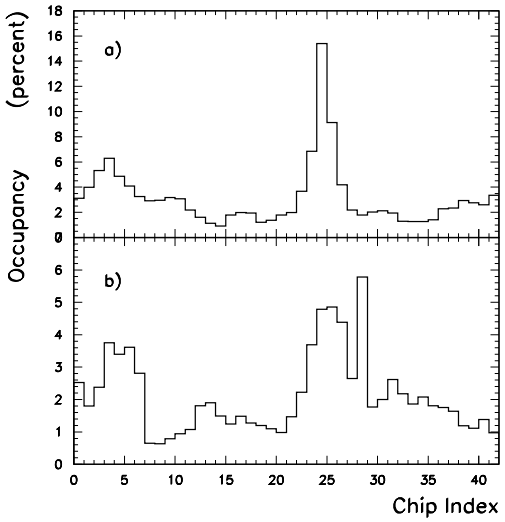

Figure 3.8: Typical occupancy in percent as a function of chip number in layer 1, ϕ side for a) forward half-modules and b) backward half-modules. Chip number corresponds to the azimuthal angle and the increased occupancy in the horizontal plane is visible near chips 3 and 25.

algorithm, which chooses among the three.

The position x of a cluster formed by n strips is determined, using the "head-to-tail" algorithm:

$$x = \frac{(x_1 + x_n)}{2} + \frac{p}{2}\frac{(Q_n - Q_1)}{(Q_n + Q_1)}$$

where x_i and Q_i are the position and collected charge of i-th strip, respectively, and p is the readout pitch. This formula results in a cluster position that is always within $p/2$ of the geometrical center of the cluster. The cluster pulse height is simply the sum of the strip charges, while the cluster time is the average of the strip times. Clusters are then converted to hits, before being passed to the tracking algorithms. Hits differ from clusters in that the hit position is expressed in the global coordinates, taking into account the physical positions of the sensors.

3.5.3 Performance

The SVT hit efficiency can be calculated for each half-module by comparing the number of associated hits to the number of tracks crossing the module. As can be seen in Figure 3.9, we typically measure combined hardware and software efficiencies of 97%, excluding defective readout sections (9 out of 208), but employing no special treatment for other defects, such as broken AC coupling capacitors or dead channels on front-end chips. Actually, since

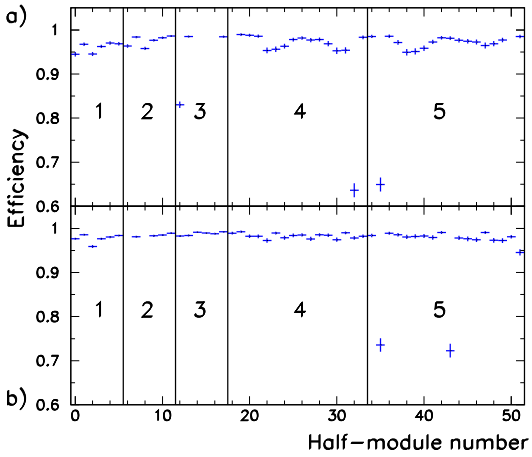

Figure 3.9: SVT hit reconstruction efficiency, as measured on $\mu^+\mu^-$ events for a) forward half-modules and b) backward half-modules. The plots show the probability of associating both a ϕ and z hit to a track passing through the active part of the detector. The horizontal axis corresponds to the different modules, with the vertical lines/numbers indicating the different layers. Missing values correspond to non-functioning half-modules.

most of the defects affect a single channel, they do not contribute heavily to inefficiency, because most charge depositions involve two or more strips, due to track crossing angles and, to some degree, charge diffusion.

The spatial resolution of SVT hits is determined by considering the distance along the sensor plane between the track trajectory and the hit, using high-momentum tracks in two prong events. The uncertainty due to the

track trajectory is subtracted from the width of the residual distribution to obtain the hit resolution. Figure 3.10 shows the SVT hit resolution for z side hits as a function of track incident angle, for each of the five layers.

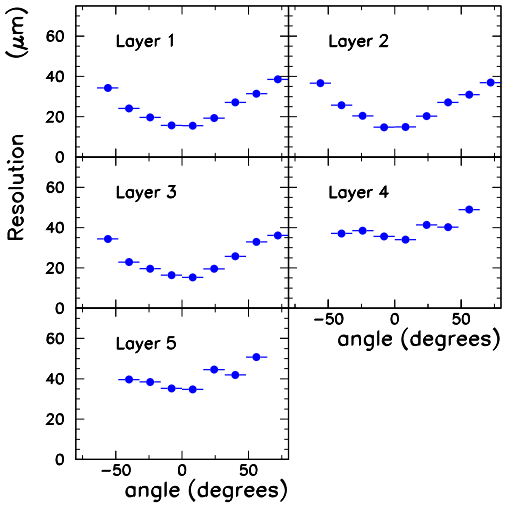

Figure 3.10: SVT hit resolution (z coordinate) in microns, plotted as a function of track incident angle in degrees. Each plot shows a different layer of the SVT.

Initial studies have shown that hit reconstruction efficiency and spatial resolution are effectively independent of occupancy for the occupancy levels observed so far.

Tracking resolution studies are discussed in detail in section 5.

3.6 Outlook

The Silicon Vertex tracker, effort of a collaboration among American and Italian institutes [39], has been operating efficiently since its installation in the *BABAR* experiment in May 1999. The five layer device, based on double-sided silicon sensors, has satisfied the original design goals, in particular achieving the targets specified for efficiency, hit resolution and low transverse momentum track reconstruction. The constraints imposed by the storage rings resulted in a complex mechanical design, with each of the layers being

mechanically distinct and with a forward/backward asymmetry that reflects the asymmetry of the storage rings themselves.

One result of this complexity is the current lack of spare modules. A program of spare module production has commenced, with the goal of replacing the non-functioning modules already in place in addition to providing additional spares for possible future need. The additional modules will be ready by summer 2001, although the exact date of the replacement is still under discussion due to the length of shutdown time (about five months) required to make the replacements.

Furthermore, a study is currently underway to understand the impact of significantly increasing the luminosity, well beyond the original design value, on SVT performance. Radiation studies, data acquisition issues and reconstruction software performance are all under consideration. A high priority item is understanding the behavior of SVT modules as the radiation dose increases above the nominal budget. Early results indicate that the sensors will continue to function after type inversion (at 1-3 MRad), but further tests with irradiated sensors and AToM ICs must be performed. Data acquisition for the SVT will not be a problem at increased luminosity. Some physics studies have also been performed, using simulated data with background at 5 times the current level, which is pessimistic since the outer layer occupancy is not expected to scale with luminosity. Preliminary results show no change in mass or vertex resolution for the mode $B^0 \to J/\psi K_S$ and a $\sim 20\%$ loss of resolution in the $D^{*+} - D^0$ mass difference. In this study, both channels suffered an inefficiency loss of 15–20%.

Chapter 4

SVT detector running

The running of the SVT detector is a basic issue for the *BABAR* experiment since is the fundamental device to reconstruct the decay vertices.

The quality of the SVT data have thus strong influence on the quality of the reconstructed events and we need to continuously monitor the performances of the SVT and the operating conditions in order to provide meaningful and reliable data.

In addition we need to ensure the necessary protection from the high level of radiation present around the interaction region. This is tightly coupled to accelerator and the storage ring operations, and to the interaction with the other sub-detectors.

The candidate has followed during his Ph.D. most of the activities related to the the start up, commissioning and running of the detector.

4.1 Quality assurance

SVT quality assurance starts on-line while taking data with the "fast monitoring", before the full reconstruction of the events in order to provide a fast quality feedback to the operators.

4.1.1 Fast monitoring

All the SVT channels above threshold are recorded to disk for each triggered event. The analysis of the simple channel occupancy (fraction of channels above threshold) can give us great information on the detector. We note

that layer 1 and layer 2 occupancies are dominated by hits of beam lost particles and particles coming from the IP. Sections 0,1 and 6,7, which are located in the horizontal plane, exhibit higher occupancy (fig. 4.1) than the neighbouring ones. This is due to the non uniformity of the radiation of beam loast lost particles, wich is concentrated in the horizontal plane due to the horizontal bending of the beams near the IP.

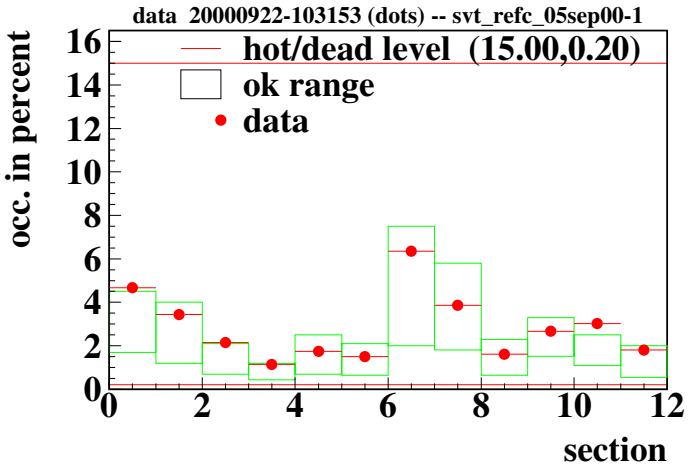

Figure 4.1: Occupancy distribution as a function of read out section (half module) for layer 1 ϕ, the bads correspond to normal conditions, values out of the bands generates alarm messages

Some sections can occasionally exhibit very low occupancies. Typically this low occupancy is due to a misconfiguration of the thresholds of the ATOM chip, a loss of the trigger, or some other condition that prevents the half module from acquiring data, condition which can be immediately individuated and corrected. Similarly a section with high occupancy can be generated by an unusual high background level or an increased noise on the module. Run-by-run generated histograms are thus automatically compared with a reference one and warning messages are reported to the operators in an automated system when the values are out of a range of occupancies defined on the basis of the "normal" variation for each section.

Since these histograms give us also a feeling of the background running conditions, they increase the ability of the SVT to be protected against high radiation levels and can give useful feedback to PEP-II operators to tune

the beam parameters.

A second level of the quality control is performed on the distribution of the time stamp of the SVT hits w.r.t. the (uncorrected) trigger time (Fig 4.2). The flat part of the distribution is due to uncorrelated background and electronics noise, while the peak is due to triggered events. The presence of the peak ensures that we are acquiring the triggered event in the jitter window of 1 μs.

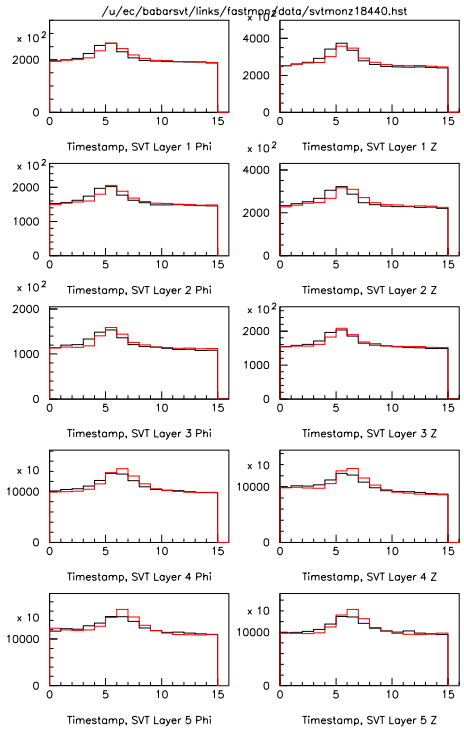

Figure 4.2: SVT time stamp distribution as seen in level 1 trigger events

4.1.2 On-line Prompt Reconstruction monitoring

After typically one day from the acquisition the raw data are fully reconstructed and a number of quality checks can be performed using the reconstruction informations, in particular the track fits.

In order to spot out possible problems some quantities are relevant:

- number of missed tracks;

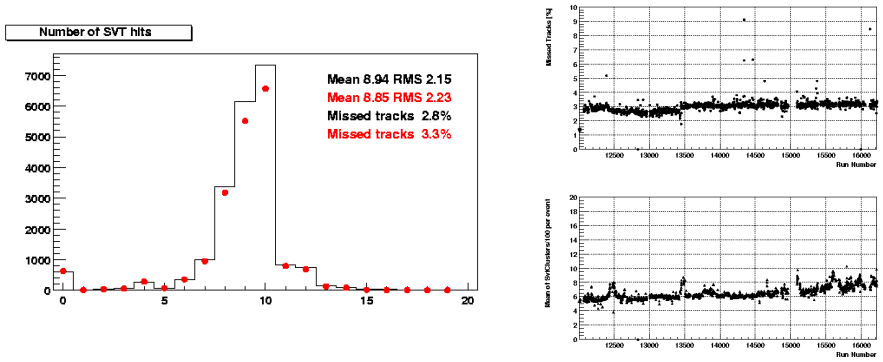

Figure 4.3: (left) Number of SVT hits per event, black is current run, red is reference run. The first bin represents the SVT hit pseudo efficiency. (right) Percentage of missed tracks and number of clusters per event distribution as a function of time from OPR quality monitoring plots

- number of clusters per event;
- z and ϕ residuals for each layer;
- corrected time stamp of the event.

The first one, the SVT pseudo tracking efficiency (fig. 4.3), is computed from the number of tracks reconstructed in the drift chamber not merged to any SVT hit, divided by the total number of drift chamber tracks. Since it is possible to reconstruct the tracks in the drift chamber independently from the SVT tracking the percentage of SVT "missed" tracks is an indirect measurement of the SVT efficiency. It is really useful to immediately spot out SVT loss of efficiency and tracking related problems.

The number of SVT clusters per event is directly related to background conditions and increases rapidly with the number of tracks present in the event. Its importance resides in the fact that if the number of clusters per event is too big the SVT tracking efficiency can be considerably degraded. The distribution of the number of SVT clusters per event as a function of run number (fig. 4.3) shows infact several bumps; all of them correspond to an increased level of the background coming from the beams when, indeed, the vacuum is turned back on after a long period of work around the IP and the residual materials in the beam pipe begin to degass and not allowing to reach the optimal level of vacuum. The gas particles remaining in the beam

pipe scatter with electrons and positrons of the beams and generate beam lost particles wich translate into background around the IP. The same effect is obtained if a vacuum leak is present.

Using reconstructed tracks we can also monitor the resolution of the SVT tracking using the track "residuals". The track residuals on a layer are computed from the difference of the center of the cluster with the crossing point of the fitted track. The value of this quantity is limited by in the intrinsic resolution of the silicon sensors (10-15 μm) but is sensitive to the local SVT alignment. In fig. 4.4 a summary of the distribution of the residuals as a function of run number is reported. It can be noted that several "jumps" are present in the distribution, which are related to changes in alignment constants. As the alignment procedure get better understood the residuals get smaller. The monitoring of this quantity is particularly useful after a work on the detector that implies moving of heavy parts of it like the iron doors for the magnet flux return. In such cases small assestments of sub-detectors relative positions can induce deformations on the SVT support structure, that even at the level of a few ten μm can be relevant for analysis. In addition thermal stress due to changes in the ambient temperature can generate internal tensions that modify the local alignment.

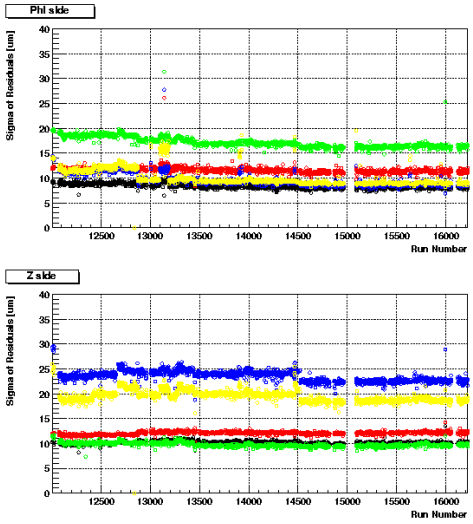

Figure 4.4: Distribution of residuals for ϕ and zed read out

In the reconstruction procedure the event time is fitted in the drift chamber as one of the parameters of the track. This time is used to correct the time stamp of the event as recorded by the SVT front end electronics (= time after the electronic has received the trigger) and leads to a very narrow time distribution in the SVT with a width of ~ 8 ns (fig. 4.2). In order to reduce background hits during the reconstruction the hits are required to be within 50 ns to the event time so a much wider distribution would thus result in a loss of signal hits and thus of efficiency. This quantity has been useful in the past to spot out timing problems of the trigger lines for the SVT front end electronics.

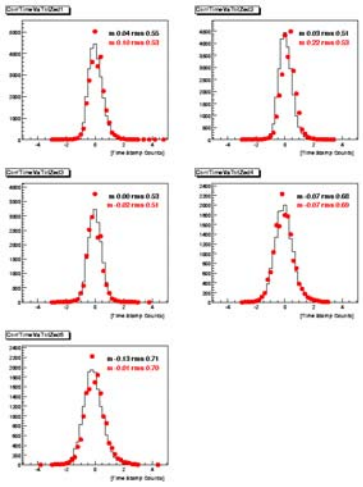

Figure 4.5: Distribution of corrected event time, black = current run, red = reference

4.1.3 Detector calibration

Detector calibration is needed to periodically verify the performance of the SVT sensors and front-end electronics, and to ensure its stability over time. It consists in measuring the noise and the gain of each read-out channel. The front-end electronic is infact provided with an internal circuit capable of injecting a variable amount of charge in the preamplifier, simulating in this way the response of the silicon sensors to a charge deposit on the corresponding strip. With the "threshold scan" procedure the threshold for the preamplified signal is varied from the minimum to the allowed maximum and the number of signals above threshold are recorded. Since we can imagine this signal as a fixed injected quantity plus the uncorrelated noise, the distribution of the signal amplitude is a Gaussian function with μ = signal, σ = noise. The number of events above a threshold x is just the integral of the Gaussian function from x to ∞. The result is thus an "error function" (fig. 4.6) from which is possible to extract the mean pedestal (mean value of the output of the preamplifier) and the noise (variance of the pedestal) for each channel. The gain of the preamplifier can be extracted from the plot of the pedestal as a function of the injected charge (fig. 4.7). The typical gain

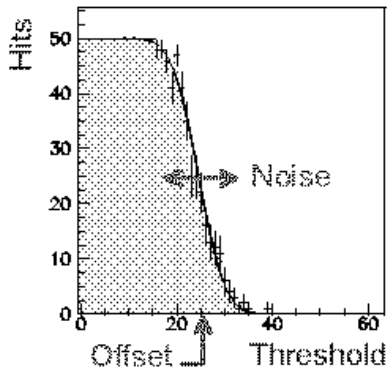

Figure 4.6: Example of threshold scan

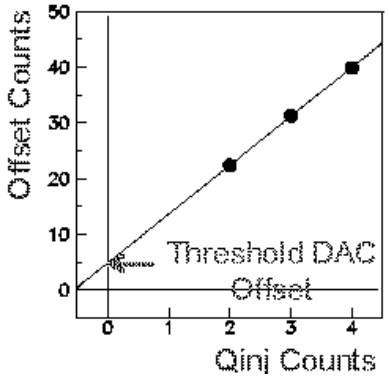

Figure 4.7: Pedestal as a function of the injected charge

is about 250 mV/fC and the noise varies from 750 to 1500 ENC (Equivalent Noise Charge) depending on the side and on the layer.

The calibration is performed every day and the result is compared with a reference histogram (fig 4.8).

After every calibration an automated analysis is run in order to identify defective channels. A defective channel is identified (defined) by a small threshold and a small noise which includes detached channels, broken AC capacitors, broken p-stop implants. A broken p-stop implant can be generated for example by an intense enough burst of radiation. In figure 4.9 the number of defective channels for layer 1,2,3 is reported as a function of time. The first jump around day 200 is due to a radiation burst generated by a misfunction of the PEP-II beam abort system, which has lead to conduct the beams directly into the SVT. The second jump is (probably) due to

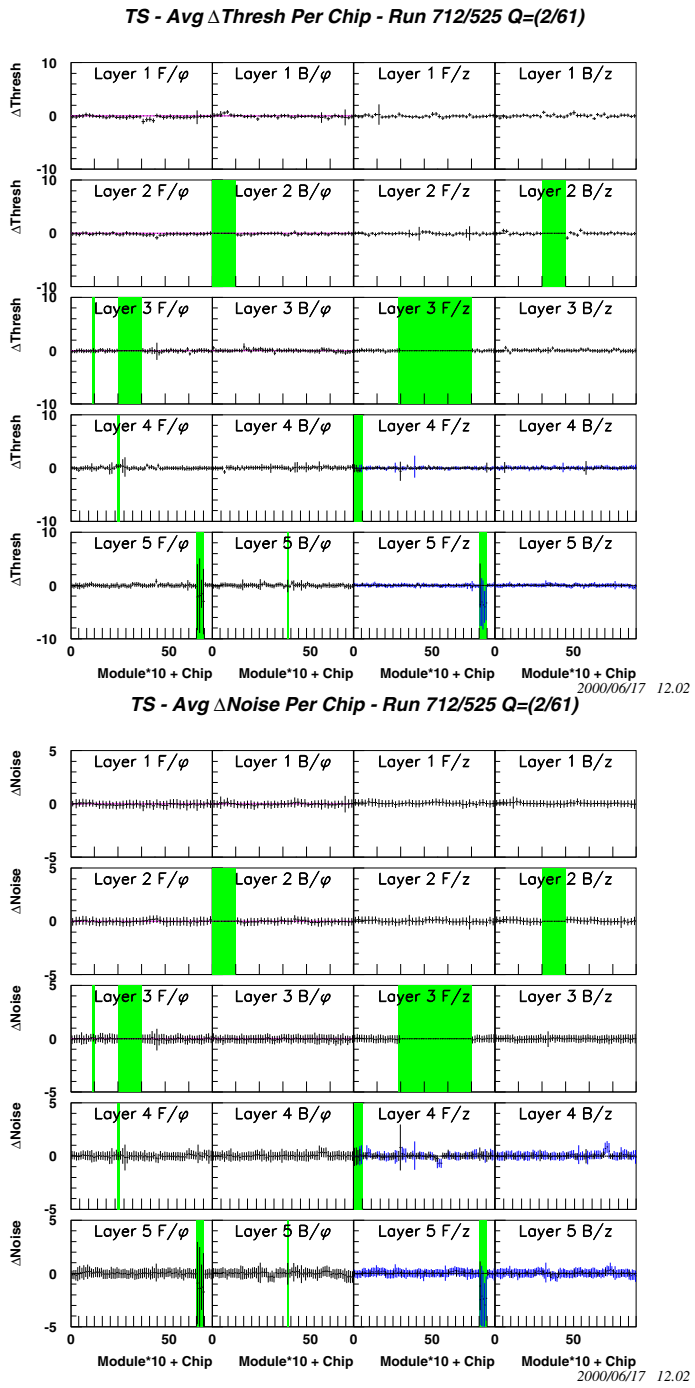

Figure 4.8: Pedestal(above) and noise(below) differences of a calibration run w.r.t the reference run. Green zones are not acquired sections

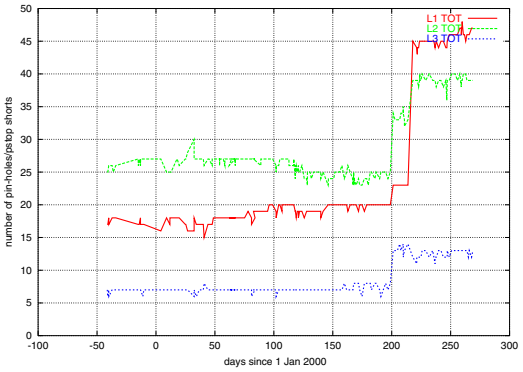

Figure 4.9: Number of defecting channels for layer 1,2,3 as a function of time

some electrical shock during a 2 weeks shutdown period.

4.2 Detector control and monitoring

Detector Control (or slow control) consists of monitoring and controlling the operating parameters of the detector, handling of interlocks and alarms, data archiving and interfacing with PEP-II. Its function crosses system boundaries since involves sensors and actuators which are part of the detector systems, data acquisition hardware which is part of electronics, and software which is part of online computing. An graphical overview is provided on fig 4.2. The arrows represent the flow of the data which can be monitoring information, control commands, hardware interlocks and analog signals.

The actual control and monitoring devices have been discussed in the SVT detector section. We remind here that they can be divided in:

- on-detector monitors
  - radiation monitors
  - temperature monitors
  - position monitors
- off-detector control and monitors
  - Power supply
  - Fluids

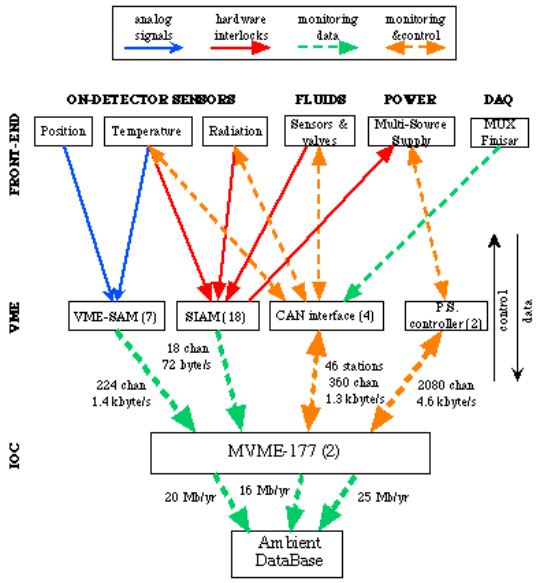

Figure 4.10: Overview of the SVT detector control schema.

Some more detailed comments are need about the power supply. Each SVT module is powered using 2 fully floating power supply modules, one for the forward half and one for the backward one. This leads to 104 independent boards. Each board provides power lines for the front-end electronic and the bias for the detector. The ground of the read-out electronic is referred to the bias of the corresponding side. The common of each SVT module is the "center tap" of the HV. All the commons are tied together with the along with module from the SVT monitoring system and defined as the SVT common. The following parameters of each power line is remotely monitorable and controllable:

- on/off/trip status
- voltage setpoint
- voltage output
- current setpoint
- current output
- last trip history

This is done with a custom Experimental Physics and Industrial Control System (EPICS) based driver via a VME crate that uses the caenet high speed protocol. All the informations are joined together to form the basic input and output of the SVT high level control mechanism, the "SVT state machine" (sec 4.3.2). In the following we will describe the general characteristic of the EPICS interface and then the SVT specific implementation.

4.3 EPICS interface

4.3.1 General principles

The Experimental Physics and Industrial Control System (EPICS) is an architecture for building scalable control systems, a collection of code and documentation comprising a software toolkit. primarily developed at the Los Alamos National Lab and at the Argonne National Lab.

Architecturally, EPICS embodies the standard model of distributed control system design. The most basic feature of EPICS is that it is fully distributed: It requires no central device or software entity. This achieves the goals of easy scalability, of robustness and of incremental operation and upgrade.

EPICS comprises three *physical layers* and five *software layers*. The physical "front-end" *layer* referred to as the Input/Output Controller (IOC) is typically built from VME/VXI hardware crates, CPU boards, and I/O boards, the physical "back-end" *layer* is a usual workstation. These layers are connected by the "network" *layer* (Ethernet).

The *software layers* are built on the "client-sever" schema. The "client" layer usually runs in the workstation/PC physical layer and represents the top software layer. Typical generic clients are operator control screens, alarm panels, and data archive/retrieval tools.

The second *software layer* that connects all clients with all servers is called "channel access" (CA). Channel access, the backbone of EPICS, hides all the details of the TCP/IP network from both clients and servers and creates a solid firewall of independence between all client and server code. CA also uses a technique called "callback" or "notify by exception": once a client has expressed an interest in certain data to a server, the server notifies the client only when the data changes. This not only minimizes traffic, but

signals both the health of the server and the freshness of the data.

The third *software layer* is the "server" layer. The fundamental server is the channel access server that runs on the target CPU embedded in every IOC and on the database server. This server cooperates with all channel access clients to implement the callback and synchronization mechanisms already described.

The fourth, or "database" *layer*, is really the heart of EPICS and is described in terms of function-block objects called records . About 50 record types exist (and can be extended) for performing such chores as analog input and output; binary input and output; building histograms; storing waveforms; moving motors; performing calculations; implementing PID loops, emulating PALs, driving timing hardware; and other tasks. Records that deal with physical sensors provide a wide variety of scaling laws; allow smoothing; provide for simulation; and accept independent hysteresis parameters for display, alarm, and archive needs.

The fifth, bottom *layer* of software, is the "device driver" layer. This implements the actual basic communication with the physical device.

4.3.2 SVT client interface

SVT EPICS panels are divided in sections specific for power supplies, radiation environment, fluids and position (fig. 4.11).

The power supply panels (*Power*) allow access to

- voltage monitors and settings,
- current monitors and limits
- ramp up/down speed, ramp-up sequence
- trip status

They provide also functionality to control the 104 HDIs in groups corresponding to a whole layer. The number of records that are involved is impressive : 1040 records with 10 fields each. The communication with the PS crates uses the caenet high speed protocol. Since it is impossible to scan all the 10400 data each second a cache mechanism has been implemented. Two separate tasks coexist in the Input Output Controller, one that reads

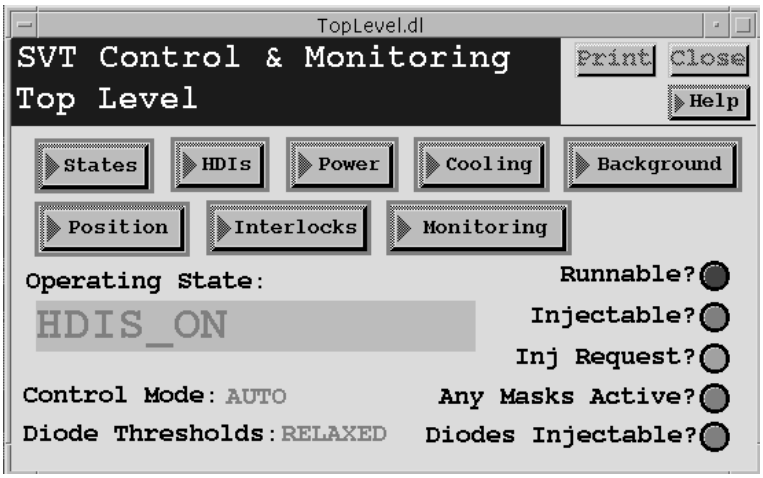

Figure 4.11: Top level panel for the SVT control and monitoring EPICS system

the values from the caenet and updates the memory cache, another one that reads the content of the cache in the cache in the IOC's memory. In this way the amount of data going trough the caenet is reduced to a feasible level [40].

On the radiation monitoring side the diode currents are digitized by 4 SVTRAD modules in the SVT MUX racks and then massaged in real-time EPICS to extract instantaneous dose rates and absorbed dose integrals, using the temperature and damage history correction factors.

The SVT EPICS comprises also panels (*Cooling*) dedicated to control the flow of the cooling water and the monitor of water and air temperature, humidity and dew point inside the SVT detector. Monitoring the dew point is important in order to avoid condensation of water on the front-end electronics.

All these informations join together in the so called "SVT state machine" (fig. 4.12) which uses a high-level language called the *State Notation Language* to implement a cooperating finite-state machine. Four states are defined:

- Cooling off
- Power off

- Stand by
- All on

The machine determines the current state of the detector on the basis of the input from the various monitoring systems and a button allow to go from one state to another. If something goes wrong in the transition or if simply the state of the detector is not anymore coherent with the one of the machine, it goes in a fault mode.

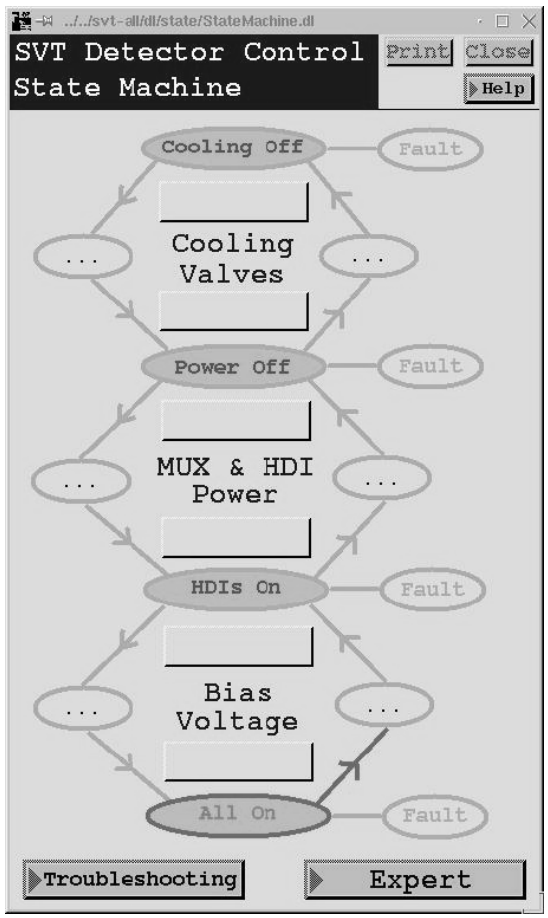

Figure 4.12: SVT state machine main panel

The first state (Cooling off) corresponds to all the systems powered off. The second one (Power on) corresponds just to the cooling being switched on, but all the power lines off. The third one (Stand by or HDIs on) corresponds to the situation in which the cooling is on, the data acquisition

electronic and the front-end electronic is powered but the HV of the silicon is zero. This is the situation in which the SVT stands when waiting for the machine to have beams. In the last state (All on) the HV of the silicon is at the nominal value and the diode thresholds are in the strict setting.

In addition to this the state machine implements the interaction of the SVT with the PEP-II controls by setting the "runnable/injectable flag" for the SVT. This is needed in in order to ensure that the beams are not injected when the bias of 40 Volts is applied to the silicon sensors, because the high radiation levels generated during the injection process could damage the p-stop implants.

Finally all the monitoring data from the power supplies (current/voltage monitoring and trip status) radiation protection (dose rates), fluids and position monitors are archived for off-line analysis and correlation plots in an object oriented database.

4.4 Radiation Protection

Radiation damage

We will introduce here the relevant aspects of the damage in the silicon sensors due to ionizing radiation in order to understand the problematics related to the SVT dose budget.

Radiation damage is usually referred to as surface or bulk damage, where the second one has the most dramatic consequences in an high hadron fluence environment.

Surface damage is due to ionizing radiation passing through the silicon and is usually parameterized with the absorbed dose. The effects are caused by surface defects, introduced at the interface between the silicon and the oxide, which is always present on the non implanted silicon surface, and by the increased positive charge trapped in the oxide.

The macroscopic consequences of the surface damage are:

- an increase in the silicon reverse leakage current;
- an increase in the inter-strip capacitance.

Both effects are roughly proportional to the dose and the latter one shows a saturation behavior after a few tens of krad. Both these effects cause an

increase in the noise of the front end electronics and result in a continuous deterioration of the detector performance.

On the contrary, bulk damage cannot be simply related to the absorbed radiation dose but it depends on particle type, fluence, and energy. The NIEL scaling (Non Ionizing Energy Loss) has proven to work very well in describing bulk damage from hadrons [1]: it is strictly related to the so called equivalent particle fluence ϕ_{Eeq}. Then, to evaluate bulk damage, particle fluences should be normalized to 1 MeV neutron fluence, taking into account the different damage efficiency, dependent on particle type and energy. As an example, in the range between 1 MeV and 1 GeV, neutrons are expected to be between 50 and 10 times more effective in causing bulk damage than electrons of the same energy. Studies performed for the LHC experiments, focused on hadron bulk damage, validate the NIEL scaling in a wide range of energy and particle types.

The main macroscopic effects of bulk damage, relevant for silicon detector performance, are:

- an increase in the silicon reverse leakage current, proportional to the equivalent fluence;
- a change in the total depletion voltage, the voltage necessary to extend the electric field, required for charge collection, through the full detector thickness.

The depletion voltage is proportional to the absolute value of the effective doping concentration of the bulk, the sum of donor and acceptor concentrations $N_{eff} = N_d - N_a$. Irradiation causes a partial donor removal, depending exponentially on the fluence, and an introduction of acceptors, proportional to the fluence. This dependence on the equivalent fluence has been confirmed in many irradiation experiments with hadrons, although in literature data for bulk damage from electrons in the GeV range are not available.

Silicon strip detectors built on n-type silicon substrate ($N_d > N_a$), like the SVT detectors, have p^+ and n^+ implanted readout strips on the two sides. With low particle fluences detector depletion voltage starts to lower; after type inversion ($N_a > N_d$) a junction is still present between the n^+ strips and the p-type bulk, and the depletion voltage starts to increase again. The dependence of this effect on particle fluences is also complicated due to

the presence of annealing and reverse annealing mechanisms. As an example of the magnitude of the effect consider that an equivalent fluence of 2×10^{13}part/cm^2 can cause type inversion in n-type silicon detectors, with an initial depletion voltage of about 40V.

The increase in the bulk leakage current causes an increase in the front end electronics noise and could deteriorate the detector performance in a continuous way. The change in the depletion voltage is by far the most worrying effect, type inversion being critical for SVT operation. For particle fluences below type inversion, SVT silicon detectors are still fully efficient: keeping constant the bias voltage applied to the detectors, even with a lower depletion voltage, the active detector volume is the total detector volume. On the contrary there are serious concerns about SVT operability with higher particle fluences, above type inversion: SVT silicon detectors were not designed to work after type inversion and they are not proven to work in these conditions, although this possibility is under investigation.

Experiments were performed irradiating with Γ from ^60Co some silicon strip detectors and diagnostic structures. The results, as expected, showed a dominant surface damage with an increase in the surface leakage current of about $0.5\mu A/MRad-cm^2$ and an increase of about 20% in the inter-strip capacitance.

Two radiation experiment has been performed: at the SLAC facility with the shower developed by the 3.1 GeV LER beam on a copper target, and at Elettra, the Trieste syncrotron facility, using a 0.9 GeV electron beam.

The most important result is the change in the depletion voltage of the sensors after irradiation up to 0.5-0.7 Mrad respectively, sumarized in table 4.1

Radiation source	Dose	$\Delta_I bulk$	$\Delta_V depletion$
Elettra electrons (e^- 0.9 GeV)	250 KRad	$4.1\frac{\mu A}{MRad\ cm^2}$	8 V
Elettra beam dump (e^- 0.9 GeV)	500 KRad	$6.4\frac{\mu A}{MRad\ cm^2}$	12 V
SLAC beam dump (e^+ 3.1 GeV)	700 KRad	$2.0\frac{\mu A}{MRad\ cm^2}$	7 V

Table 4.1: Comparison between the 3 SVT radiation tests.

Dose budget

The results of the SLAC beam dump experiment were used to evaluate the total SVT radiation budget at the beginning of BaBar data taking in May 1999. The radiation dose budget was set at 2MRad, to be spent in ten years of operation. The SVT radiation budget is the upper curve in figure 4.13 and is directly proportional to the integrated luminosity of PEP-II

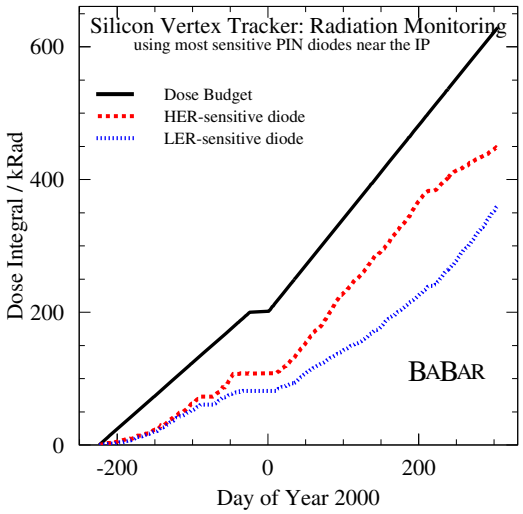

Figure 4.13: Integrated radiation dose as measured by 3 different PIN diodes located near the SVT. Also shown (upper curve) is the radiation budget.

4.4.1 Radiation sensors

Radiation monitors measure the integrated and the instantaneous doses, both in the mid plane, which is most affected by radiation backgrounds, and out of it as well. The radiation monitors consist of 2 sets of six PIN diodes [38], placed at a radius of 3 cm, and at $z = \pm 10$ cm. Their leakage currents, after a correction for temperature dependence, provide a signal that is proportional to the radiation exposure level.

The system is also capable of interlocking the SVT power supplies and the PEP-II beams (sec. 4.4), and provide useful feedback and diagnostics for PEP-II controls. They are located under the support cones below layer-1

HDIs, on a ring around the beam-pipe at z= +/- 10 cm at a radius of about 3 cm and measure the radiation dose rates due to machine backgrounds. The sensors are 12 photodiodes with an active area of 1 $cm \times 1\ cm \times 0.03\ cm$, they are reverse biased to about 50 $Volts$ and generate a signal of about 0.2 nC per mRad absorbed. Their leakage current increases by about 1 nA per kRad absorbed because of the damages cause by the ionizing radiation and varies by about 10% per degree C. The diode behaves like a current source whose output varies with the instantaneous dose rate, the integrated dose received, and the temperature. The accuracy for measuring dose rate (= total current - leakage current) depends on the current-measuring accuracy of the readout, and eventually (after sufficient radiation damage) on the accuracy to which the diode temperature can be monitored to correct for leakage current variations. The accuracy for measuring integrated dose (= increase in leakage current) is limited by how well a diode's annealing history has been tracked, and the uncertainty in the damage coefficient (nA/kRad).

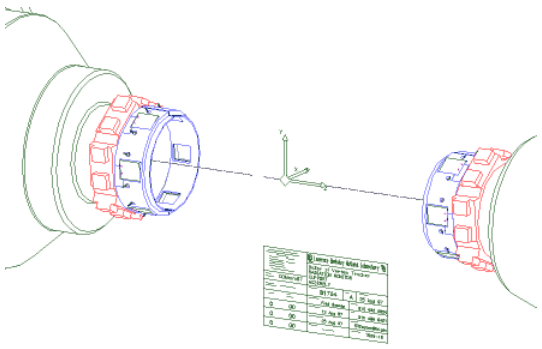

Figure 4.14: Radiation monitors disposition over the support cones

Each diode is read out using either a monitoring (RADMON) or interlock (ABORT) module. These 2 modules are based on complementary designs: the RADMON module is based on a flexible and sensitive ADC, while the ABORT module is based on a simpler but more reliable current-to-frequency converter and is used to generate the hardware beam abort signal.

The system is able to monitor average dose rates to better than 0.5 mRad/s, allowing us to keep the average dose per day within 10% of the 1.5 kRad/day budget. The integrated dose, as measured by the PIN diodes, is

shown in Figure 4.13. The system also provides an instantaneous measurement of the radiation rates at a level better than 5 mRad/s and an interlock protection to PEP II. Injection can be inhibited, or, if necessary, the beams aborted.

Beam abort system

If a considerable amount of radiation hits the silicon when the bias voltage is applied serious damage can happen. The radiation would create a conducting channel of electron/hole pairs between the positive and the negative side. The presence of the AC coupling insulator would generate a drop of all the HV on the AC capacitor. Even if the capacitors are designed to hold 40 Volts a considerable amount of capacitor (2 % from a test done at INFN of Pisa) will brake down. We know that during the injection of the beam in the machine high radiation events happen quite often and thus we have installed an hardware interlock circiut (ABORT circuit) that prevents PEP-II from injecting the beams when the SVT HV is on.

In order to protect SVT against high radiation blasts an hardware abort system has been installed (called the ABORT circuit) for each of the four mid plane diodes.

This system uses the diodes currents directly and converts the it to a radiation dose in mRad/s using a conversion factor computed taking into account temperature accumulated dose corrections. It starts integrating the radiation when the dose goes above a "chronic" threshold (d_0). When the integrated dose goes above the abort threshold (D_0) the system aborts the PEP-II beams. In this way for a fixed dose above the chronic threshold the time needed to trip the beams is directly proportional to D_0. The abort can't be faster than the system response time that is about $200\mu sec + 400\mu sec/Rad * D_0$ and depends on the D_0 threshold.

The current thresholds are $d_0 = 1000mRad/s$ and $D_0 = 10Rad$. This protect against very intense radiation events.

While this "fast" abort mechanism is completely hardware and protects the SVT against too much radiation too fast there is another software based abort mechanism. This system, based on EPICS code, trips the beams if the radiation level is above a panel-adjustable dose threshold for 5 consecutive minutes. It allow to prevent the SVT from absorbing too much radiation

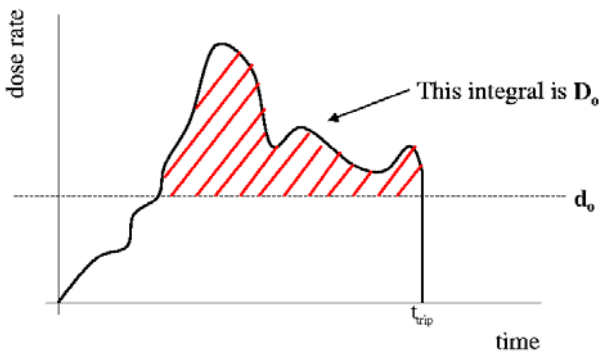

Figure 4.15: Graphical view of the abort thresholds of the SVTRAD hardware abort system

continuously.

However we have to keep in mind that every trip of the beam causes about 10-15 minutes of down-time needed to inject again the beam in PEP-II, so the figure of merit of the abort system is the number of trips per integrated luminosity (fig. 4.16 that measure our efficiency in taking data without tripping the beams too often.

4.4.2 IV measurements

In order to monitor the status of the silicon wafers from an electrical point of view, we perform a measurement of the I-V (current-voltage) characteristic curve about every six months for each half module. This kind of measurement shows the fundamental characteristics of the wafers: the depletion voltage and the leakage current. The radiation exposure causes an increase in the leakage current of the wafers. We can assume that the radiation seen by the neighboring diode is equal to the radiation absorbed by the corresponding half module and we can plot the increase in the bias current as a function of the radiation. This is shown in fig. 4.17.

It is particularly important to monitor the depletion voltage because we know that the radiation damage causes the depletion voltage to diminish and after about 2-3 MRad the inversion of type of the n bulk (recent studies done at the INFN of Trieste show that the wafer continue to function properly also after type inversion).

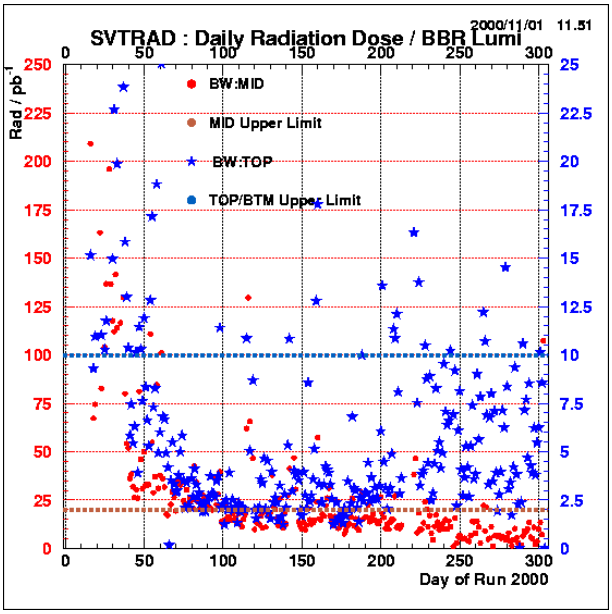

Figure 4.16: number of trips per integrated luminosity: red colors (scale on the left) correspond to a MID plane diode, blue colors (scale on the right) correspond to a non MID plane diode

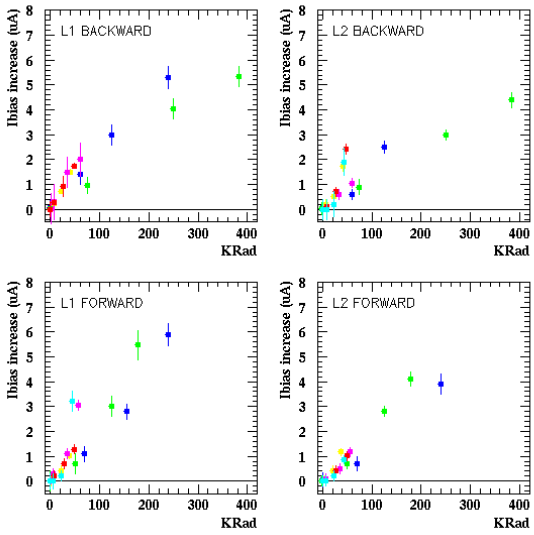

Figure 4.17: Increase in bias current as a function of the absorbed radiation: different colors correspond to different location of the half modules

Chapter 5

Tracking and Vertexing

We will now introduce the basics of the tracking and vertexing of *BABAR* since these are the main ingredients used in the analysis of the events for the D^0 lifetime measurement.

5.1 Tracking strategy

Charged track finding in off-line reconstruction starts with pattern recognition in the DCH. A better event time is needed than that available from the L3 trigger, so the first step is to find an improved t_0 using three parameter fits (d_0, ϕ_0, t_0) to four-hit track segments in the DCH super-layers.

The first pass at DCH track finding takes the track parameters and associated lists of hits from the output of the L3 track finder and performs helix fits; if a fit succeeds, that track is retained. A search for additional hits in the DCH that may belong on these tracks is made, and the event time is further refined using the timing information from only those hits assigned to tracks. Two subsequent track finders are run on the remaining DCH hits. These use super-layer segments constructed out of hits not used on previous tracks, and are designed to find tracks either at lower p_T than found by the L3 track-finder, passing through fewer than the full ten super-layers, or without bias towards originating from the interaction point. In this way more sophisticated track finders run in a progressively cleaner tracking environment with a constantly improving measure of the event time.

At the end of this process, the found tracks are refit using a Kalman filter fitter. This fitter takes into account the detailed distribution of material

in the detector and the full map of the non-uniformities in the detector magnetic field. The tracks are then projected into the SVT, and silicon strip hits are considered for addition to the tracks if they are consistent with the expected error from extrapolating through the intervening material and field. Various possible combinations (branches) of SVT hits are considered, and the branch contributing the least to χ^2, while meeting pattern requirements designed to limit the number of silicon wafers providing no measurement, is retained. When all intersected wafers have been inspected for hits and the best branch is selected, a full Kalman fit is performed on the ensemble of DCH and SVT hits.

Any remaining SVT hits are then passed to two complementary SVT stand-alone track-finding algorithms. The first one reconstructs tracks starting with triplets of space points (matched ϕ and z hits) in layers 1, 3 and 5 of the SVT, and adding to the triplets consistent space points from the other layers. A minimum of four space points are required to form a good track. The second stand-alone SVT tracker first finds circles from hits in the xy plane, then looks for consistent z hits. This second method is particularly effective in using hits that do not form space points, *e.g.,* when one side of a half-module is not functioning. Together, the stand-alone SVT tracking algorithms are responsible for reconstructing tracks with low transverse momentum, which do not reach the drift chamber.

At the end of the SVT-only track finding, a search of the track list is made for tracks made up of only SVT hits which match closely at the support tube to other tracks made up of only DCH hits, since the support tube is a localized source of scattering between the two devices. If any candidates are found, a common fit to both sets of hits is attempted. If this succeeds, only the combined track is retained; otherwise, both stand-alone tracks are kept on the track list. At the end of pattern recognition and fitting, all tracks are checked to see if they lie in momentum ranges where the particle hypothesis might affect the result of the fit, and if so, each track is fit with up to five stable-particle mass hypotheses.

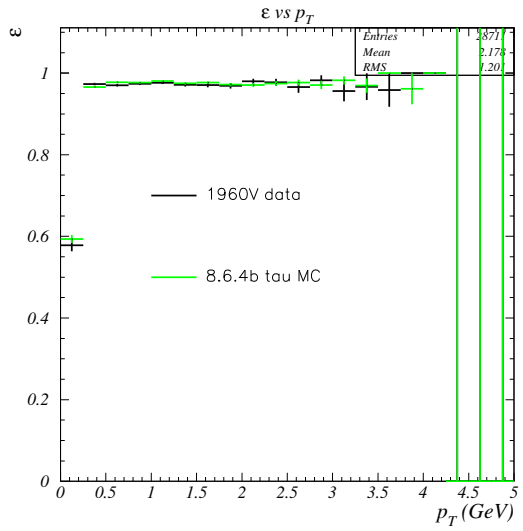

Figure 5.1: Absolute reconstruction efficiency determined from tau-pair events.

5.2 Tracking efficiency

The track reconstruction efficiency has been determined from data using control samples and by employing the fact that track-finding is accomplished using two independent tracking devices, the SVT and the DCH.

A control sample of 1-prong versus 3-prong tau pair events are used to estimate the absolute tracking efficiency. Events are selected without making any requirements on the third track on the 3-prong side. After correcting for detector acceptance, which is done using Monte Carlo simulation data, the fraction of such tau pair events for which the third track is successfully reconstructed provides a measurement of the reconstruction efficiency for tracks in the range $0.2 < p_T < 3.0\,\mathrm{GeV}/c$ (fig. 5.1).

The ability of the SVT tracking to reconstruct tracks with low transverse momentum, tracks that would otherwise go undetected, is illustrated in Figure 5.2. A sample of slow pions is selected by reconstructing events of the type $\bar{B} \to D^{*+}X$ followed by $D^{*+} \to D^0\pi^+$, where the pion from the D^* decay has a soft momentum spectrum. As can be observed in the figure, the majority of such pions are have only SVT hits associated to them, *i.e.*, they have not been reconstructed in the drift.

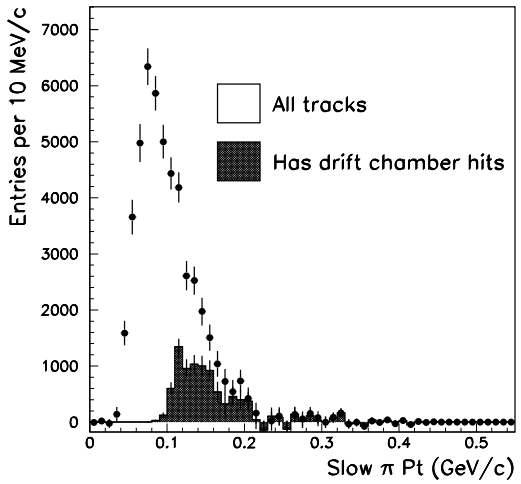

Figure 5.2: Transverse momentum spectrum of slow pions from $D^{*+} \to D^0\pi^+$ from B decays. Continuum subtraction is used to reject higher momentum D^* mesons from continuum production. Only a small fraction of the pions have drift chamber hits (shaded area), the others are reconstructed by SVT stand-alone tracking.

DCH efficiency

The tau pair studies, as well as Monte Carlo simulation studies, suggest that the DCH is the major contributor to the track reconstruction inefficiency. This has been studied by measuring the fraction of time the DCH portion of a track is reconstructed, given an existing SVT track that falls into the acceptance of the DCH. Corrections are made to take into account the small rate of fake SVT tracks. This relative tracking efficiency, R_{eff}, has been tabulated in bins of p_T, polar and azimuthal angle and event track multiplicity for each run in the data sample.

As a cross-check and measure of systematic uncertainties in the above method, a control sample of $D^0 \to K^-\pi^+\pi^+\pi^-$ decays, where the D^0 is reconstructed from the decay $D^{*+} \to D^0\pi^+$, is used to make an alternate measurement of R_{eff}. All of the D^0 daughter tracks are required to have SVT hits and the number of such D^0 for which three of the four tracks have

DCH hits is compared with the number of D^0 for which all four tracks have DCH hits. The ratio of the two numbers is the relative efficiency R_{eff}.

Good agreement is observed between the two methods and no further systematic uncertainty is assigned to the track reconstruction efficiency.

We assign a conservative 1.0% systematic error per track to the absolute DCH track finding efficiency above 200 MeV/c in p_T.

5.3 Tracking resolution

For the purpose of most physics analyses, charged tracks are defined by five parameters $(d_0, \phi_0, \omega, z_0, \tan\lambda)$ at the track's point of closest approach (poca) to the z axis, and the associated error matrix. d_0 and z_0 are the distances from the origin to this poca in the transverse (x, y) plane and along the z axis, respectively. ϕ_0 is the angle between the transverse component of the track tangent vector at this poca and the x (horizontal) axis. λ is the angle between the transverse plane and the track tangent vector at this poca (the "dip" angle). ω is the curvature of the track, and the charge of the track is incorporated in the signing convention for ω while the sign of d_0 is determined from the angular momentum of the track w.r.t. the x axis.

d_0, ϕ_0, z_0, and $\tan\lambda$ resolutions are dominated by the resolution of the SVT while the DCH makes a significant contribution to the p_T measurement.

Track resolution is monitored in online prompt reconstruction with Bhabha and mu-pair events, and is further investigated after the data is fully reconstructed with tracks in hadronic events and reconstructed cosmic ray events.

Fig. 5.3 shows the d_0 and z_0 resolutions as a function of transverse momentum (p_T) as determined from tracks in hadronic events. For this study, the tracks not being examined were vertexed together, and the d_0 and z_0 with respect to this vertex were calculated. These were accumulated and a Gaussian fit was made to the negative part of the distributions (particle lifetime can contribute to the positive part of the distributions). Requirements were also made on event thrust and vertex χ^2 to reduce the effect of decay lifetimes on this measurement. The contribution from the vertex errors were accumulated and fit for, and removed from the measured resolutions in quadrature. The d_0 and z_0 resolutions so measured are about 27 and 40 μm respectively at $p_T = 3$ GeV/c. These agree well with resolutions

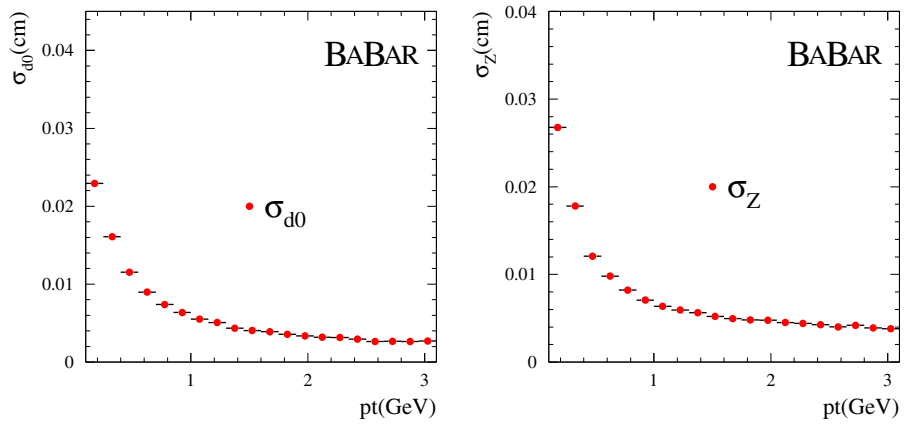

Figure 5.3: a) Impact parameter resolution of tracks, reconstructed using all available tracking information, in the xy plane as a function of transverse momentum; b) Impact parameter resolution for the z projection.

measured in the other studies.

The ϕ_0 and $\tan\lambda$ resolutions are measured in the cosmic ray studies to be 0.45 mr and 0.8×10^{-3}, respectively, at about GeV/c. The p_T resolution, directly related to the ω resolution, is measured in the cosmic ray studies as a function of p_T (Fig. 5.4), and is about 0.8% at $p_T = 3\,\mathrm{GeV}/c$. For the cosmic rays studies, cuts were made on the d_0, z_0, and $\tan\lambda$ of the track to make sure the track passed close to the nominal beam interaction point in d_0 and z_0 and populated the parts of the detector normally populated with tracks in beam interaction events. The upper and lower halves of the cosmic ray were fit as two separate tracks, and the resolutions were derived by comparing the values of the track parameters for the two tracks at their poca's to the z axis.

5.3.1 $\mathrm{d}E/\mathrm{d}x$ Resolution

Fig. 5.5 shows the distribution of the reconstructed and corrected $\mathrm{d}E/\mathrm{d}x$ from the drift chamber as a function of track momenta. The superimposed Bethe-Block curves for the individual particle species have been determined using various particle control samples.

The resolution achieved to date is typically about 7.5% for Bhabha, as

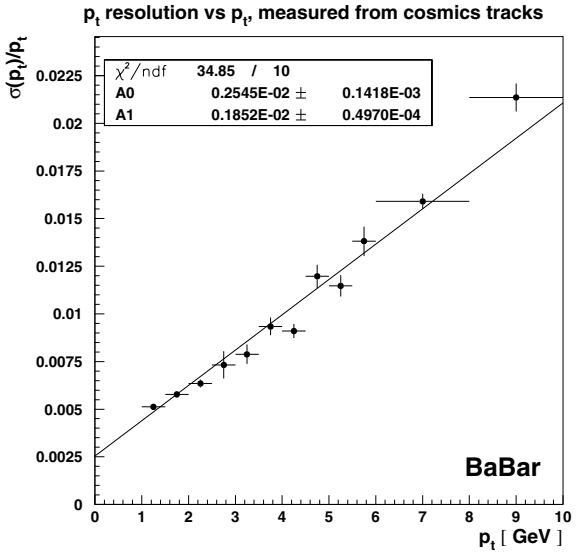

Figure 5.4: p_T resolution determined from cosmic ray muons.

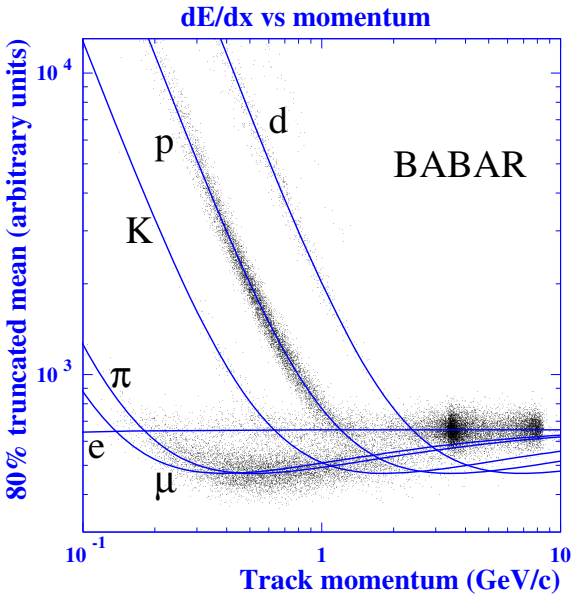

Figure 5.5: Reconstructed $\mathrm{d}E/\mathrm{d}x$ as a function of track momenta

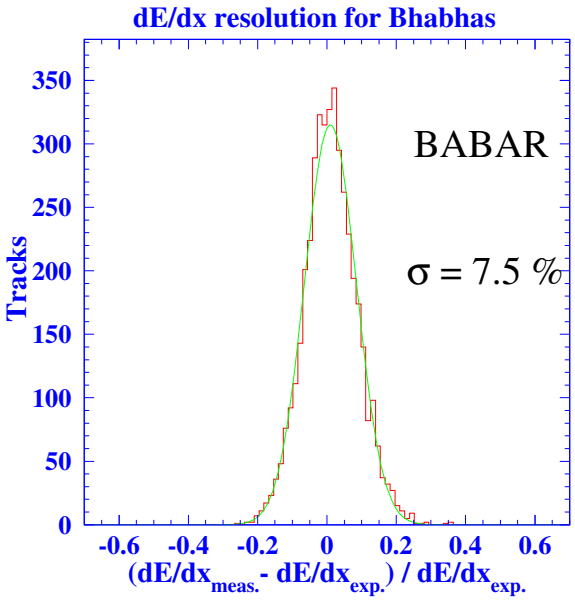

Figure 5.6: Distribution of the difference between the measured and expected dE/dx for Bhabha while operating at 1900 V

shown in Fig. 5.6 This is close to the expected resolution of 7%, which we expect to achieve with further refinement or addition to the applied corrections.

Independent dE/dx measurement of charged tracks is a less important, but non-negligible, function of the SVT. A truncated mean algorithm is used, keeping 60% of the hits for tracks with at least 4 associated SVT hits. The resulting dE/dx distribution as a function of momentum is shown in Figure 5.7.

5.4 SVT and DCH Alignment

SVT alignment is performed in two steps. The first consists in its internal (or local) alignment, that is the determination of the relative position of the silicon sensors. This is followed by the global alignment, which determines the position of the SVT relative to the drift chamber. In both cases, high momentum tracks from two-prong $\mu^+\mu^-$ events are used by the alignment algorithms.

For the local alignment, SVT stand-alone tracking is used to reconstruct

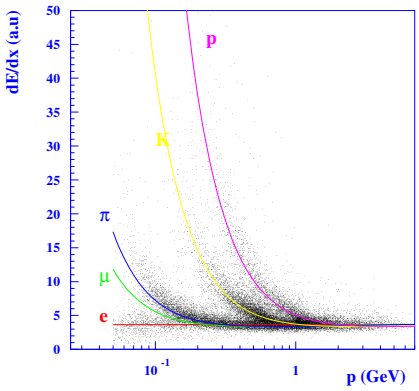

Figure 5.7: Energy loss per unit length (dE/dx) as measured in the SVT as a function of momentum. The enhancement of protons is due to beam-gas interactions. The vertical scale is arbitrary.

the tracks, effectively decoupling the SVT local alignment from the drift chamber, but the curvatures of the tracks are constrained to the values measured by the DCH. The two tracks are fit simultaneously, imposing the known invariant mass of the two tracks. This technique significantly improves the determination of the track parameters, leading to a more precise alignment. A χ^2 minimization is employed to find the optimum position of each sensor by minimizing the track-hit residuals. A new internal alignment must be performed typically every 1-2 months. The internal alignment procedure is still under development and we expect, in the near future, to make significant improvements to the algorithm.

After the internal alignment, the SVT is considered as a rigid body. The second alignment step consists in determining the position of the SVT with respect to the drift chamber. Tracks with sufficient numbers of SVT and DCH hits are fit twice: once using only the DCH information and again using only the SVT hits. The six global alignment parameters, three translations and three rotations, are determined by minimizing the difference between track parameters obtained with the SVT-only and the DCH-only fits. As reported in sec. 3.4.2, because of the diurnal movement of the SVT with respect to the drift chamber, this global alignment needs to be done once

per run ($\sim$ every 2 hours). The alignment constants obtained on a given run are then used to reconstruct the data in the subsequent run. This procedure, known as "rolling calibrations", ensures that track reconstruction is always performed with up-to-date global alignment constants.

5.5 Vertex reconstruction

In the following we will describe briefly the vertexing algorithms, as described in several *BABAR* publications in preparation, used in this analysis.

In *BABAR* there are two main vertexing algorithms `GeoKin` and `FastVtx`. The first has been designed to be more flexible for kinematic fitting of a whole decay tree, dealing in a simple way with complex decay chains, the second is faster and can be preferred in very high multiplicity events.

In the D^0 lifetime analysis we have used the `GeoKin` algorithm since we have to deal with the refit of the D^0 and soft pion candidate to the Beam Spot position.

5.5.1 Formalism

While in the tracking code the tracks are represented with the five parameters $(d_0, \phi_0, \omega, z_0, \tan\lambda)$ at the track's point of closest approach to the nominal z-axis, the vertexing code make use of the position-momentum representation $(x_0, y_0, z_0, p_0^x, p_0^y, p_0^z)$ which introduces a correlation between the parameters but make easier the implementation of the constraints.

The vertexing procedure starts with an initial guess of the position of the vertex. For short living particles (such as B and D) the primary vertex is good enough. For V^0's (such as K^0's the point of closest approach of the two tracks is used. In the latter case the tracks are approximated to a circle in the transverse plane and the point of closest approach is computed analytically.

We call $\mathbf{y}$ the vector of the measured quantities and W_y its relative weight matrix, $\mathbf{y}$ is for example the vector of the track parameters. Our purpose is to find the best estimate of some unknowns $\mathbf{x}$, for example the position of the vertex of the tracks, using an iterative χ^2 minimization technique, that takes into account the m relations existing between the measured quantities

$\mathbf{y}$ and the unknowns $\mathbf{x}$:

$$f_k(\mathbf{x}, \mathbf{y}) = 0 \tag{5.1}$$

The χ^2 is constructed with the Lagrange multipliers technique [42] introducing the m multipliers $\boldsymbol{\lambda}$ and minimizing the χ^2

$$\chi^2(\mathbf{x}, \mathbf{y}, \boldsymbol{\lambda}) = \chi^2(\mathbf{x}) + \chi^2(\mathbf{y}) + \sum_{k=1}^{m} \lambda_k f_k(\mathbf{x}, \mathbf{y}) \tag{5.2}$$

with respect to $\mathbf{x}, \mathbf{y}, \boldsymbol{\lambda}$. In order to find analytically the minimum of eq. 5.2 is necessary to expand the function f in the vicinity of the current guess of the parameters x_0, y_0

$$\begin{aligned} \chi^2(\mathbf{x}, \mathbf{y}, \boldsymbol{\lambda}) \quad \simeq \quad & \chi^2(\mathbf{x}) + \chi^2(\mathbf{y}) + \\ & + \boldsymbol{\lambda}^t \left(\mathbf{f}(\mathbf{x}_0, \mathbf{y}_0) + \partial_{\mathbf{x}} \mathbf{f}|_{(x_0, y_0)} (\mathbf{x} - \mathbf{x}_0) + \partial_{\mathbf{y}} \mathbf{f}|_{(x_0, y_0)} (\mathbf{y} - \mathbf{y}_0) \right) \end{aligned} \tag{5.3}$$

To obtain the minimum of the χ^2 is sufficient to solve the linear equation

$$\frac{\partial \chi^2}{\partial(\mathbf{x}, \mathbf{y}, \boldsymbol{\lambda})} = \begin{pmatrix} W_x & 0 & \partial_{\mathbf{x}} \mathbf{f} \\ 0 & W_y & \partial_{\mathbf{y}} \mathbf{f} \\ \partial_{\mathbf{x}} \mathbf{f}^t & \partial_{\mathbf{y}} \mathbf{f}^t & 0 \end{pmatrix} + \begin{pmatrix} 0 \\ 0 \\ \mathbf{f}(x_0, y_0) \end{pmatrix} = \begin{pmatrix} 0 \\ 0 \\ 0 \end{pmatrix} \tag{5.4}$$

The new weight matrix W' for the x/y parameters is given by the second derivative of the χ^2 function. Defining $G_x = \partial_x \mathbf{f} W_x^{-1} \partial_x \mathbf{f}^t$ and similarly for G_y we obtain

$$\begin{aligned} W'_{xx} &= \partial_x \mathbf{f}^t \left[G_x^{-1} + G_y^{-1} \right] \partial_x \mathbf{f}, \\ W'_{yy} &= x \to y \end{aligned} \tag{5.5}$$

for the diagonal terms, and

$$W'_{xy} = -W_{xx}^{-1} \partial_x \mathbf{f}^t \left(\partial_y \mathbf{f}^t \right)^{-1}, \; W'_{yx} = \left(W'_{xy} \right)^t \tag{5.6}$$

for the correlation terms. The best estimate of the x/y parameters is given by

$$x_1 = x_0 - W'_{xx} \partial_x \mathbf{f}^t G_y^{-1} \mathbf{f}(x_0, y_0) \tag{5.7}$$

$$y_1 = x \to y \tag{5.8}$$

The found parameters are used as the starting guess in the subsequent iteration.

5.6 Vertexing control samples

In order to validate the vertex algorithms in *BABAR* they have been tested real data using several control samples and still other samples are being studied.

Three main points have to be addressed to validate vertexing algorithms: the bias in the position of the vertex, the correct estimate of the errors, the resolution function compared to the Monte Carlo.

In order to estimate the bias of the position of the reconstructed vertex a sample of τ decays to three prongs have been used. The relevant variable to be studied is the so called "missed distance", i.e. the distance of one track from the vertex made with the other two. Since the three particles come from the same vertex the "missed distance" is expected to have zero mean. This can be done both in the transverse plane and along the z-axis direction. Of course the error on the "missed distance" can be computed and the distribution can be normalized to the event error. The resulting shape is expected to be a Gaussian function with zero mean an variance one. This variables are still being analyzed. Preliminary results [43] reveal some problems both in the transverse plane and along the z-axis. However while there seem to be a shift in the z position of the vertex, the mean value in the transverse plane is correct but remains a dependency on the ϕ region crossed by the tracks.

A sample of $D^0 \to K^-\pi^+\pi^-\pi^+$ can be used in a similar manner. The four tracks are grouped in two sets of two tracks. Each set is vertexed and the vertex positions are compared. In this case there is no real distinction between the two vertices and hence any bias in the position of the vertex is canceled. It is possible to analyze the distribution of the difference of the two vertices normalized to the event by event error (pull). The resulting distribution fitted with a normalized Gaussian function allow to extract a multiplicative scale factor for the event by event errors. The result show that the scale factor on data is ~ 1.18, exceeding the simulation by about 10%. In addition the RMS of the z resolution on data is worse ($\sim 500\,\mu$m) than the one measured on Monte Carlo events ($\sim 350\,\mu$m) and has bigger tails (64% w.r.t. 45%).

In the delta-z reconstruction for the *CP* measurement the resolution is

dominated by the "tag" vertex. The resolution function, for this particular algorithm [44], has been checked on off-peak data: the tracks are be divided in two lists and the "tag" vertex is reconstructed for each list. Since no B's can be produced the two processes estimate the same primary vertex and the difference of the vertices represent the resolution function. The results can be summarized in table 5.1 As in the previous case the fraction of events

δz reso	f_1	$\sigma_1(\mu$m)	$\mu_1(\mu$m)	f_{out}	$\frac{\sigma_2}{\sigma_1}$	$\mu_2-\mu_1(\mu$m)	RMS(μm)	$\mu(\mu$m)
MC	43.3	85±0.2	-0.20±0.10	11.2	2.09±0.00	0.61±0.23	141±1	0.10
Data	34.8	96±0.6	-0.35±0.23	15.6	2.04±0.01	0.79±0.45	162±1	0.09
δz pull	f_1	σ_1	μ_1	f_{out}	$\frac{\sigma_2}{\sigma_1}$	$\mu_2-\mu_1$	RMS	μ
MC	70.0	0.96±0.00	-	3.88	1.59±0.01	-	1.14±0.01	-
Data	55.9	1.06±0.01	-	6.05	1.55±0.01	-	1.32±0.02	-

Table 5.1: Resolution function parameters for data and MC continuum fits. The fit function is composed by two Gaussians with variance $\sigma_{1,2}$ mean $\mu_{1,2}$ and fraction of events $f_{1.2}$ plus a wide Gas Sian function to model outliers with a fraction f_{out} of events.

in the tails is bigger for data (65% w.r.t. 57%), the resolution and the scale factor for the errors is 10% bigger than in Monte Carlo events.

Chapter 6

D^0 lifetime measurement

6.1 Introduction

The measurement of D^0 meson lifetime in *BABAR* is important for several reasons. First of all it is a measurement of a decay length with a high statistic sample, which can be used as a stringent validation of the detector, and in particular of the most important part of it the SVT sub-detector. The inverse of the lifetime, the total width, is also needed to extract partial widths from branching ratio measurements $\Gamma(D^0 \to f) = \Gamma_{tot} \times \mathcal{B}(D^0 \to f)$. In addition the theoretical models that are used to compute the lifetime have to deal with the hadronisation of quarks into hadrons. These calculations are quite robust in the case of B hadrons since the mass involved are big with respect to the QCD scale, but are more difficult to treat at the c quark mass scale. The precise measurement of the lifetime can provide a test of these models. The possibility of measuring $D^{\pm}$ and D_s^+ lifetime in the same experiment in addition can allow a precise determination of the ratio between the lifetimes with a small systematic error. In addition the resulting D^0 measured lifetime and the resolution function can be used in a furhter study for the measurement of the $D^0\overline{D}^0$ mixing.

In the analysis a high purity sample of D^0 mesons of wich the decay length is known is selected and the lifetime is extracted from the decay lenght distribution.

6.2 Data sample and event selection

In order to measure the decay lenght of the D^0 meson is necessary to know the production point. In *BABAR* D^*'s are produced both directly in the continuum as $c\overline{c} \to D^*\ X$ or through cascade decays of B mesons: $\Upsilon(4S) \to B\overline{B}$, $B \to D^*\ X$. Only $c\overline{c}$ events have been selected because the D^* comes directly from $c\overline{c}$ hadronisation and this ensure that the decay point of the D^* is in the luminus region. For the analysis only the decay mode $D^* \to D^0\pi^+$ (68%) and the subsequent D^0 decay modes $D^0 \to K^-\pi^+$ and $D^0 \to K^-\pi^+\pi^-\pi^+$ has been considered because they are the most abundant. [1]

6.2.1 Data sample

As a dataset for all the analysis we have used 8.33 fb^{-1} of data collected in year 2000 near the $\Upsilon(4S)$ resonance, wich are composed of 88% of on resonance data and 12% of off resonance data (i.e.) collected at a lower energy).

6.2.2 MonteCarlo Samples

To study the background properties we have used the equivalent of 1.85 fb^{-1} of $c\overline{c}$ events, 4.27 fb^{-1} of $b\overline{b}$ events, 1.81 fb^{-1} of *uds* events wich was the hole Monte Carlo available at the time of the analysis. Since this is not the expected mixture we have rescaled each sample by the corresponding factor.

In addition, to study the signal properties, we have generated a sample of $c\overline{c}$ events preselected requiring at the generator level that at least one signal event is present for each event. We have generated 106000 events for the $D^0 \to K^-\pi^+$ channel, equivalent to 6.05 fb^{-1} and 102000 events for the $D^0 \to K^-\pi^+\pi^-\pi^+$ channel equivalent to 3.0 fb^{-1} .

6.2.3 Event Selection

Two decay channels of the D^0 meson have been considered: $D^0 \to K^-\pi^+$ and $D^0 \to K^-\pi^+\pi^-\pi^+$. The selection of the events is in many aspects

[1] Charge conjugated modes will be assumed throughout in the following

similar for the two cases so they will be discussed together. Three main requirements have been considered:

1. origin of the selected D^0 candidates within the beam spot, i.e. we don't want to select D^0's coming from B decays.
2. low background contamination.
3. well reconstructed D^0 vertex in order to improve the flight length and proper time resolution.

The first point is achieved by selecting those D^* with a momentum in the $\Upsilon(4S)$ center of mass frame greater than 2.5 GeV/c. This selection criterion removes almost competely the D^* coming from $b\overline{b}$ with an efficiency of 84.0 % for D^* from $c\overline{c}$. In figure 6.1 the CM D^* momentum for $c\overline{c}$ events is shown.

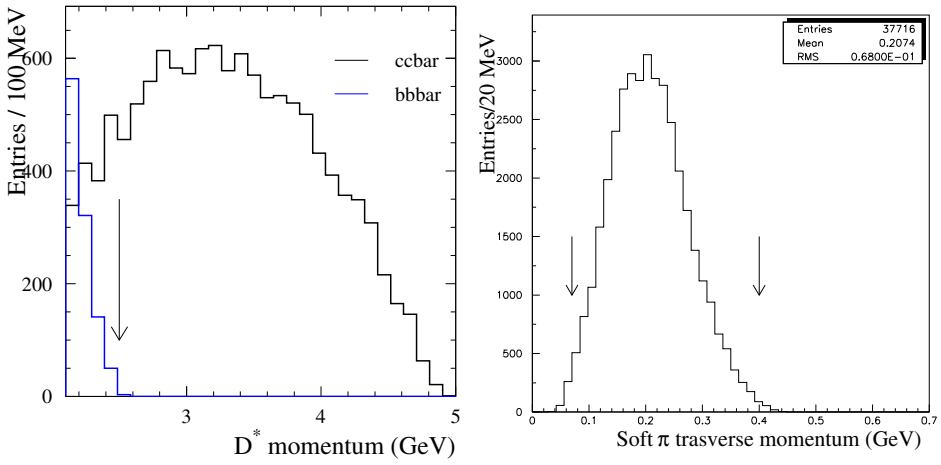

Figure 6.1: D^* momentum in $\Upsilon(4S)$ center of mass frame, π_s transverse momentum in lab frame in MC signal events

In order to obtain a clean D^0 sample the candidates are required to come from the decay chain $D^* \to D^0\pi^+$. Since the Q-value of the decay is very small (6 MeV) the resolution on the mass difference $m_{D^*} - m_{D^0}$ is dominated by the error on the measurement of the soft pion (π_s^+) transverse momentum. Its mean value in $c\overline{c}$ events is about $\simeq 200\,\mathrm{MeV}/c$ (fig 6.1) and thus the error is dominated by the multiple scattering in the beam pipe. If

we assume the tracking resolution measured from cosmic rays we obtain a resolution of about 600 keV.

To obtain a better resolution on $m_{D^*} - m_{D^0}$ we perform a vertex fit of the whole decay chain using the slow pion, the D^0 and the beam spot. The resolution on the angle between the slow pion and the D^0 gets better as shown in fig 6.2. The Δm distributions with and without refit are shown

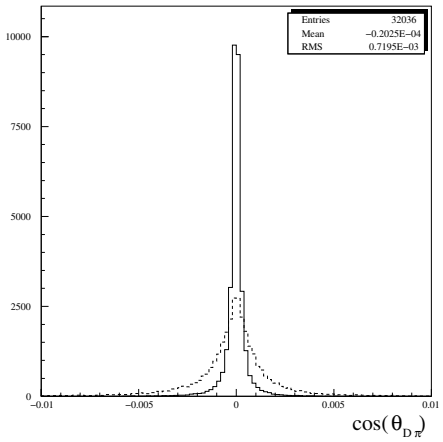

Figure 6.2: Error on $\cos\theta_{D^0\pi_s}$ without refit (dashed), with refit (continuous)

in fig. 6.3 The width of the core gaussian reduces from 0.670 MeV/c^2 to 0.227 MeV/c^2. The fit to the peak with two gaussian functions plus the background gives on data a weighted mean of 0.6 MeV/c^2. The selection criterion $|m_{D^*} - m_{D^0} - 145.4\,\mathrm{MeV}/c^2| < 0.6\,\mathrm{MeV}/c^2$ is used to allow good reduction of the background.

All the D^0 daughter tracks belong to the "GoodTrackLoose" set, i.e. tracks that have passed the quality criteria: number of hits in the Drift Chamber > 20, $|z0| < 10\,cm$ and $|d0| < 1.5\,cm$. In order to reduce the track error due to multiple scattering all the tracks from D^0 must have a momentum greater than 250 MeV/c.

The proper time resolution depends on how well we can reconstruct D^0 vertex and the D^* decay position. To ensure a good D^0 vertex reconstruction and to improve the position resolution we require that at least two tracks have a ϕ hit in one of the first two layers of the SVT detector and that each track has at least 5 svt hits (a hit is intended as a cluster in the *phi* or z

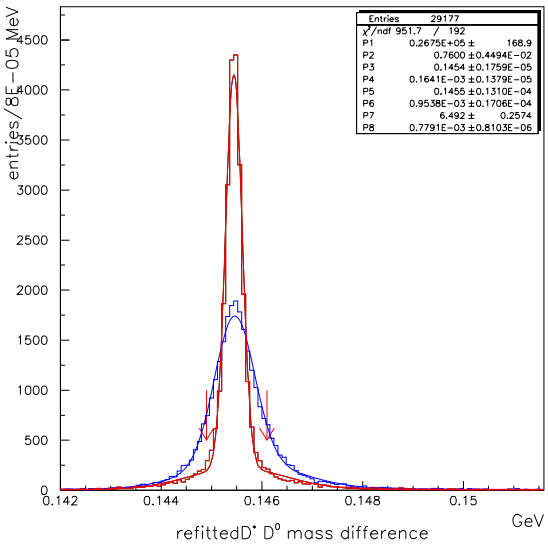

Figure 6.3: $m_{D^*} - m_{D^0}$ distribution for MC signal events: blue is no refit, red is after refit

view associated to the track).

Furthermore we require that the D^0 vertex χ^2 probability and the probability associated with the flight length calculation is greater than $> 1\%$ to reject those events for which the algorithm does not provide a good estimate of the flight length (fig. 6.4).

In order to reduce the background from the charm decays to KK and $\pi\pi$ and to reduce the combinatoric background in the $D^0 \to K^-\pi^+\pi^-\pi^+$ channel we make use also of our Particle Identification System (PID). The PID algorithm for each track combines the information of the $\mathrm{d}E/\mathrm{d}x$ from the SVT and the DCH, and the Čerenkov angle from the DIRC in a likelihood probability for a specific mass hypothesis. The D^0 sample is quite clean so we use a loose selection with the PID in the veto mode: we require that the kaon is not identified as a pion, and that each of the pions is not identified as a kaon. The effect of this selection on the generic MC background is shown in fig. 6.5 while the efficiency on signal events is close to 1. Furthermore we require a minimum $\mathrm{d}E/\mathrm{d}x_{SVT}$ for the soft pion in order to avoid fake SVT tracks.

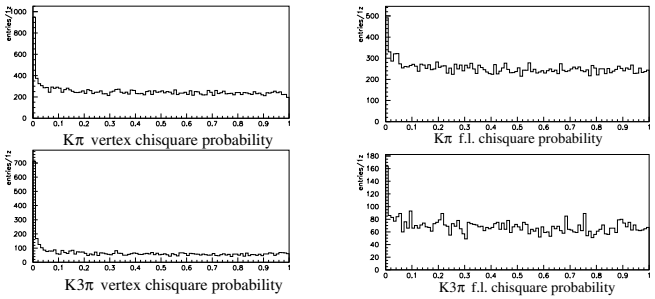

Figure 6.4: left : D^0 vertex χ^2 probability, right: flight lenght χ^2 probability for $D^0 \to K^-\pi^+$ (top) and $D^0 \to K^-\pi^+\pi^-\pi^+$ (bottom)

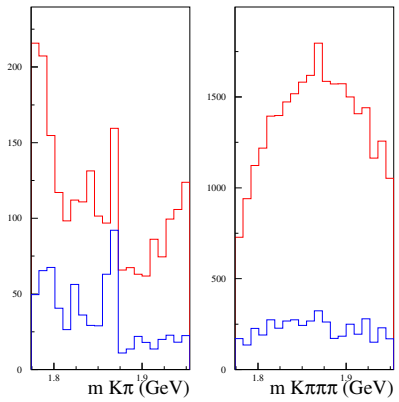

Figure 6.5: Invariant mass ditribution for background events (in the correct admixture of $c\overline{c}$, uds and $b\overline{b}$) for $D^0 \to K^-\pi^+$ (left) a nd $D^0 \to K^-\pi^+\pi^-\pi^+$ (right) with (blue) and without (red) using the particle identification

The selection requirements for the two decay channels are listed in table 6.1. The invariant mass distributions for the two decay modes after applying all the selection criteria are shown in fig. 6.6 for to the 8.33 fb^{-1} of data used in this analysis. The number of D^0 mesons in the sample can be determined from the fit of the distribution with a double Gaussian function plus a quadratic background distribution. We obtain 21150 ± 140 events in the $D^0 \to K^-\pi^+$ decay channel and 17321 ± 150 events in the $D^0 \to K^-\pi^+\pi^-\pi^+$ decay channel with a purity respectively of 99.0% and 96.0%.

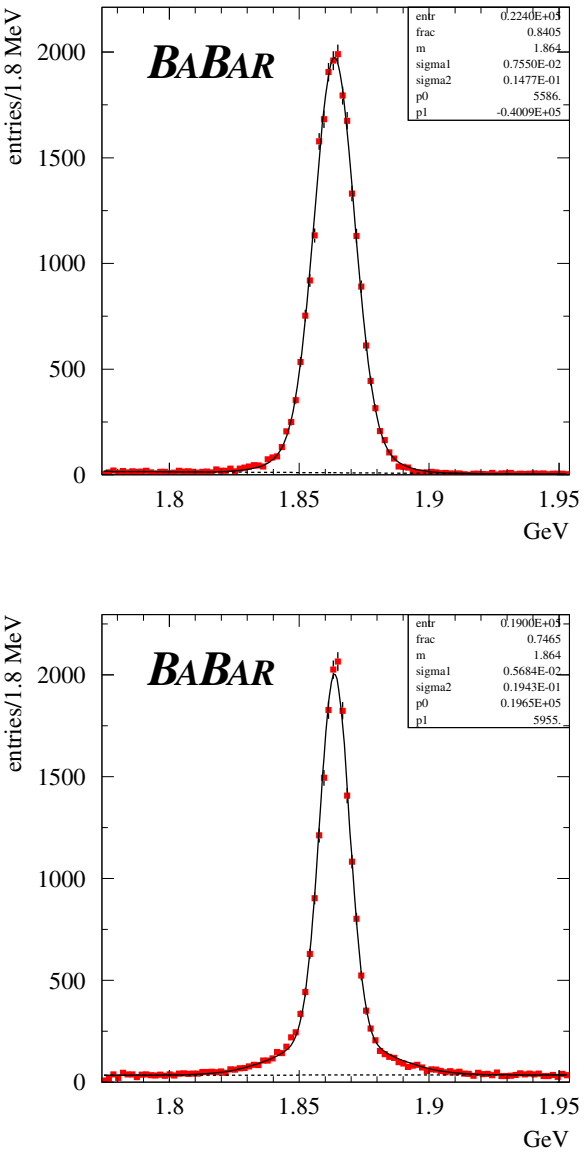

Figure 6.6: $D^0 \to K^-\pi^+$,$D^0 \to K^-\pi^+\pi^-\pi^+$ invariant mass distribution for data

Parameters	criterion	Parameters	criterion
Track quality	required	$p^{cm}(D^*)$	$> 2.5\,\mathrm{GeV}$
$P(K)$,$P(\pi)$	$> 0.250\,\mathrm{GeV}$	$\mathcal{P}(\chi^2_{D^0})$	$> 1\%$
$Pt(\pi_s)$	$> 0.070\,\mathrm{GeV}$	$\mathcal{P}(\chi^2_{refit})$	$> 1\%$
PID_K, PID_π	required	σ_d	$< 300\,\mu\mathrm{m}$
$\mathrm{d}E/\mathrm{d}x_{SVT}(\pi_s)$	> 1.5	$\lvert\Delta M - 145.4\,\mathrm{MeV}\rvert$	$< 600\,\mathrm{keV}$

Table 6.1: Selection criteria for the D^0 candidates

The number of reconstructed background events is determined from the same fit, extrapolating the quadratic background under the peak and computing the number of events in a 2σ window. We obtain 194 ± 9 events for the $D^0 \to K^-\pi^+$ and 720 ± 21 for the $D^0 \to K^-\pi^+\pi^-\pi^+$ channel.

The expected number of signal and background events is determined from Monte Carlo events applying the same procedure and is reported in table 6.2

Decay channel	MC eff.	Reconstr. D^0 mesons	Reconstr. bkg events	Expected bkg events
$D^0 \to K^-\pi^+$	$22.3 \pm 0.2\%$	21150 ± 140	194 ± 9	195 ± 29
$D^0 \to K^-\pi^+\pi^-\pi^+$	$9.3 \pm 0.1\%$	17321 ± 150	720 ± 21	1110 ± 69

Table 6.2: Yield of signal and background events in the data sample, efficiency and expected background from MC events

6.3 D^0 vertex resolution

For each D^0 candidate we reconstruct the vertex of the daughter tracks. Due to the smallness of the y dimension of the interaction region, the main source to the flight length uncertainty is usually the D^0 vertex resolution along its momentum direction but the error due to the knowledge of the position and dimension of the Beam Spot luminous region has also to be considered. In the following two paragraphs these contributions will be discussed and analyzed.

In fig. 6.7 the resolutions of the D^0 vertex along the projection of

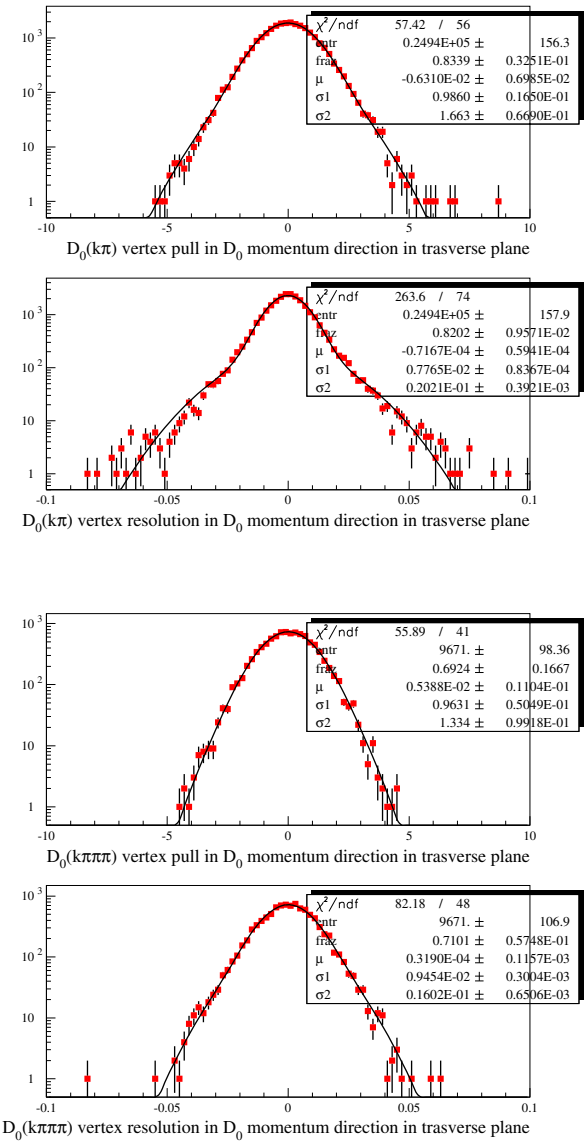

Figure 6.7: $D^0 \to K^-\pi^+$,$D^0 \to K^-\pi^+\pi^-\pi^+$ vertex resolution on MC events ($\boldsymbol{R}_{true} - \boldsymbol{R}_{reco}$) in D^0 momentum direction.

D^0 momentum in the transverse plane are shown for $D^0 \to K^-\pi^+$ and $D^0 \to K^-\pi^+\pi^-\pi^+$ decay modes in Monte Carlo events. This resolution is computed from the difference between the reconstructed and the true vertex position form the MC information. The distributions are fitted with two Gaussians function with same mean. The $D^0 \to K^-\pi^+$ plot is quite well described by a single Gaussian function but is presented with a double Gaussian fit for comparison with the $D^0 \to K^-\pi^+\pi^-\pi^+$ mode. A resolution of 78 μm and 94 μm is found (for the core Gaussian) for D^0(Kπ) and D^0(K3π) mode. The corresponding pulls are computed as the difference of the true vertex position and the reconstructed one divided by the corresponding error and are distributed as a Gaussian with zero mean and sigma one.

In order to understand if the D^0 vertex errors are well estimated on data we have considered the decay channel $D^0 \to K^-\pi^+\pi^-\pi^+$. Using these four tracks in the decay we can compute two separate vertices: Vtx12 that is the vertex between the kaon and an opposite-charged pion and Vtx34 that is the vertex of the remaining two pions. The significant quantity for the error calculation is the "pull" $\delta = \frac{(Vtx12-Vtx34)}{\sigma_{12-34}} \cdot \hat{P}_{D^0}$ where σ_{12-34} is the error on the vertex difference in the direction of D^0 momentum. If the errors are well calculated and the background contamination is small, δ should be distributed as a Gaussian function with mean zero and sigma one. In figure 6.9 this distribution is depicted for Monte Carlo and data events. In the hypothesis of no correlations between Vtx12 and Vtx34, these distributions seem to indicate that the two prong D^0 vertex errors (and by extension the $D^0(K3\pi)$ and $D^0(K\pi)$ errors) are correctly estimated.

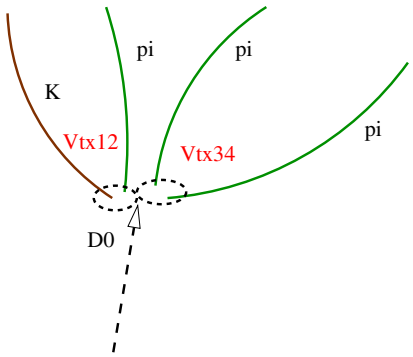

Figure 6.8: The four tracks of the $D^0 \to K^-\pi^+\pi^-\pi^+$ decay are used to form two vertices

The fact that the distribution of δ is compatible with a Gaussian function with zero mean and σ 1 on MC and data and is a stringent check of the vertex resolution on the data itself.

In fig. 6.10 the D^0 vertex error distribution for the two decay channels

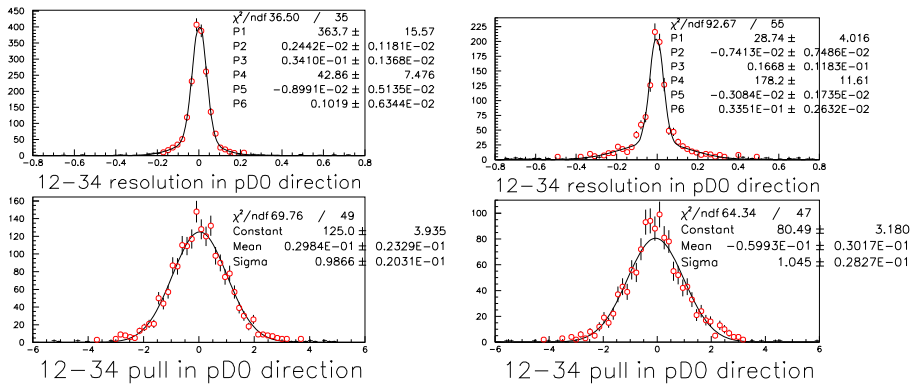

Figure 6.9: $D^0 \to K^-\pi^+\pi^-\pi^+$ vertex resolution in D^0 momentum direction using the difference between 2-trk vertices for M.C. and Data

in Monte Carlo and data are presented wich show a nice agreement between data and MC.

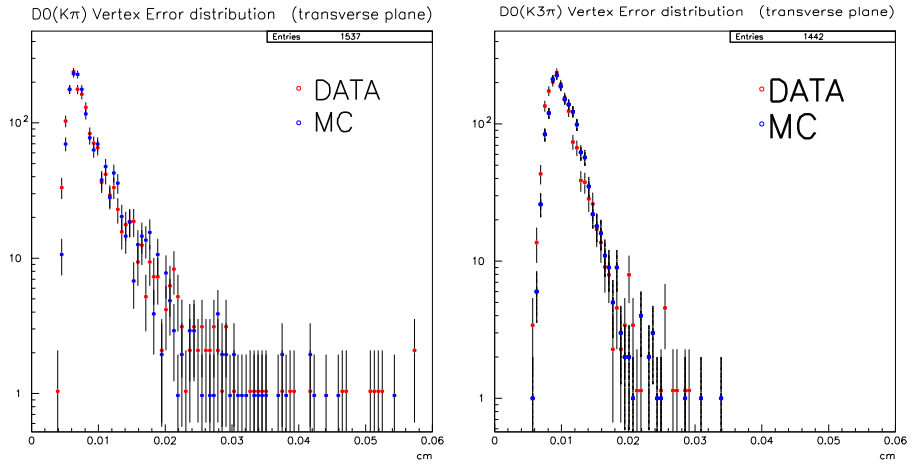

Figure 6.10: Distribution of D0 vertex errors for data and MC

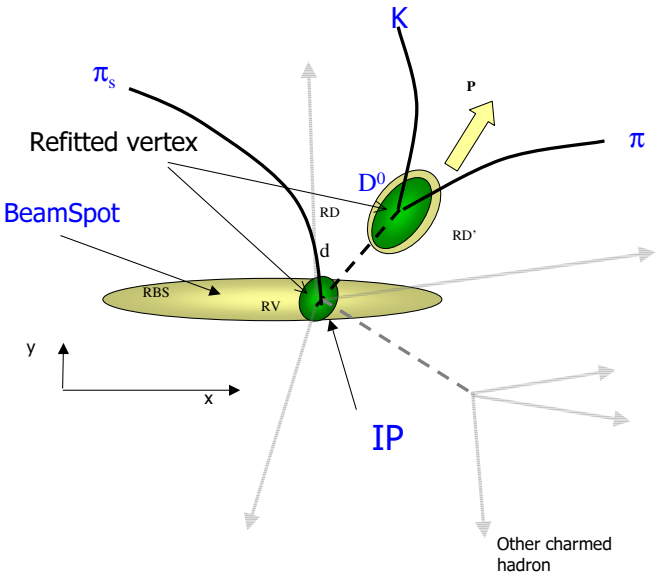

Figure 6.11: Typical topology of $D^* \to D^0\pi^+$ events

6.4 Flight Length and Primary Vertex reconstruction

In the following we will describe the flight length reconstruction method which is a key point of the analysis. We will call flight lenght the 2D distance, in the the plane orthogonal to the beam line, between the D^* decay position and the D^0 decay vertex.

In order to measure the D^0 flight length it is necessary to reconstruct the D^0 production and decay vertex. The decay point is found by simply vertexing the D^0 charged decay products. The evaluation of D^* production vertex is more problematic due to the fact that the resolution obtainable only vertexing the soft pion and the D^0 line of flight is not adequate. However in $c\overline{c}$ events the D^* meson rises from the $c\overline{c}$ hadronization and its production point coincides with the e^+e^- collision point, thus we can take as the D^0 production vertex the beam spot position with its relative error matrix. We know from luminosity considerations that the beam luminous region is about 1 cm along the z axis, 150 μm along the x axis and about 6-7 μm along the y axis. Due to the large z dimension of the Beam Spot the D^0 flight length is

evaluated in the transverse plane. In addition to this the D^* vertex is reqired to be on the line of flight of the D^0 meson wich substantially improves the resolution on the x position of the D^* vertex.

In figure 6.11 a typical $e^+e^- \to c\overline{c}$ event of interest is depicted. The flight length is extracted by minimizing the $\chi^2(\vec{r}_V, d)$ wich takes into account the beam spot and D^0 line of flight constraints:

$$\chi^2(\vec{r}_V, d) = (\vec{r}_{BS} - \vec{r}_V)^T \cdot W_{BS} \cdot (\vec{r}_{BS} - \vec{r}_V) + (\vec{r}_D - \vec{r}'_D)^T \cdot W_D \cdot (\vec{r}_D - \vec{r}'_D) \quad (6.1)$$

$$\vec{r}'_D = \vec{r}_V + d \cdot \hat{P}_D \quad (6.2)$$

r_{BS} and W_{BS} are the position and weight matrix of the beam spot, $\vec{r}_D$ and W_D are the position and weight matrix of the D^0, $\hat{P}_D$ is the direction of D^0 momentum, d is the transverse f.l. and $\vec{r}_V$ is the D^* vertex. These last quantities, d and $\vec{r}_V$, are extracted from the fit. As can be seen the χ^2 is a quadratic form in the fitted variables and therefore we can extract them analytically.

$$\begin{pmatrix} \vec{r}_V \\ d \end{pmatrix} = W^{-1}_{\vec{r}_V, d} \begin{pmatrix} W_{BS}\vec{r}_{BS} + W_D\vec{r}_D \\ \hat{P}_D W_D \vec{r}_D \end{pmatrix} \quad (6.3)$$

$$W_{\vec{r}_V, d} = \begin{bmatrix} W_{BS} + W_D & W_D\hat{P}_D \\ \hat{P}^t_D W_D & \hat{P}^t_D W_D \hat{P}_D \end{bmatrix} \quad (6.4)$$

Where $W_{\vec{r}_V, d} = \frac{1}{2}\frac{\partial\chi^2(\vec{r}_V, d)}{\partial(\vec{r}_V, d)}$ is the weight matrix for the fitted quantities.

The requirement that this $\chi^2(\vec{r}_V, d)$ have a probability $> 1\%$ ensures that the D^0 is consistent to come from the Beam Spot.

The f.l. resolution and pull is shown in fig 6.12. The distributions are fitted with two Gaussian functions with same mean. The means are compatible with zero and the width of the pull is compatible with one within 2 standard deviations. This ensures that our method to compute the errors give the correct answer, essential conditions in the maximum likelihood fit. The resolution for the core Gaussian is 87 μm for the $K\pi$ and 104 μm for the $K\pi\pi\pi$. It can ge noted that the pull distribution for te $K\pi\pi\pi$ channel is a good single gaussian distribution (it has been fitted with a double gaussian for comparison) due to the bigger number of tracks involved in the vertex fit which does not dramatically improve the resolution but reduce the fraction of events int the tails.

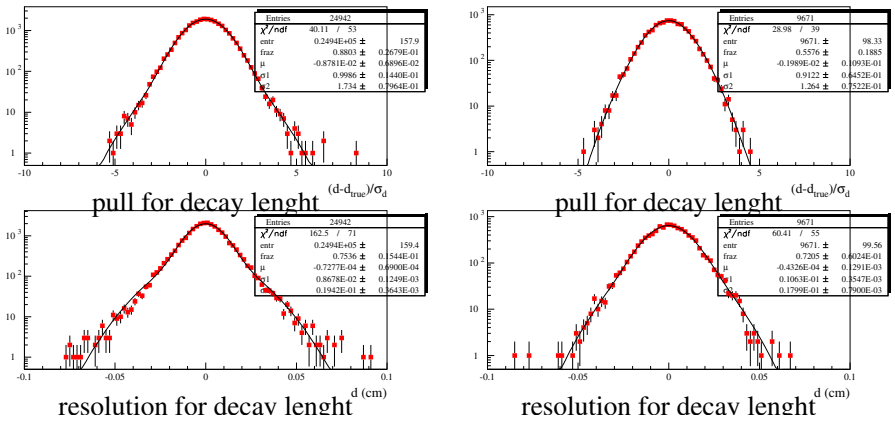

Figure 6.12: $D^0 \to K^-\pi^+$, $D^0 \to K^-\pi^+\pi^-\pi^+$ f.l. resolution and pull on signal MC events

6.5 Beam spot systematic effects

As mentioned in section 6.4 the D^* decay vertex is calculated by constraining the D^0 to come from the beam spot region. As a consequence, the precision on the flight lenght and on the errors on it depends on our knowledge of the position and size of the beam spot. This is a delicate point that requires an accurate study as it can be a source of systematic shifts in the lifetime and under/over-estimation of the flight length errors. In particular the estimate of the beam spot y size can not be taken from beam spot position measurements because it is smaller ($\sigma_y \simeq 7\,\mu$m) than the tracking resolution and needs to be assumed, for example, from luminosity considerations.

In this study we start from a MC sample of signal events with a given beam spot y dimension of 4 μm. Then we proceed to vary three quantities:

1. The beam spot σ_y assumed in the χ^2 minimization (eq. 6.2) in the range $4, 10, 30, 50\ \mu m$

2. A random movement of the beam spot y position with a spread of 10, 20, 30, 40 μm.

3. A fixed bias in the beam spot y position in the range 4, 10, 20, 30, 40 μm.

In the first case the assumed beam spot is bigger than the actual one but its position is correct. The error on the flight lenght is thus overestimated. In the likelihood function the error on the lifetime is multiplied by a scale factor S_1 which is fitted on the data itself. If the errors are correctly estimated the scale factor is 1. If the the errors are overestimated (as in this case) the scale factor becomes smaller than one to compensate the effect and reduce the size of the errors (fig. 6.5). In this way the fitted lifetime is not affected by the overestimation of the errors, as the scale factor decreases with increasing σ_y.

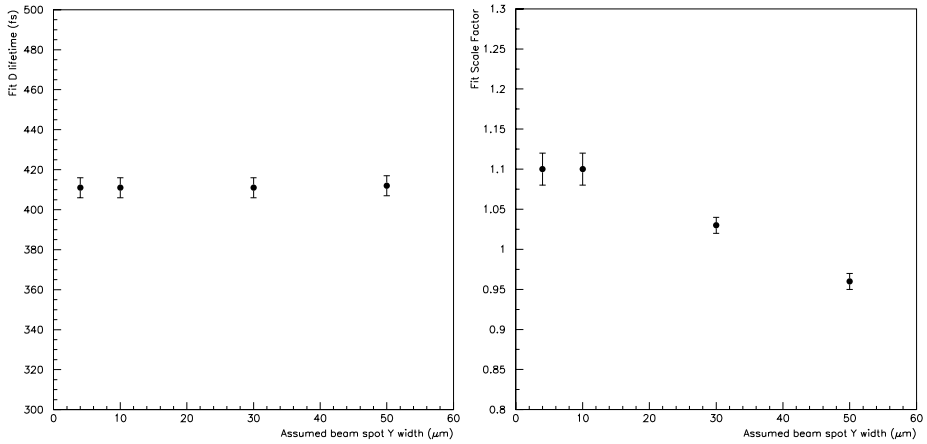

Figure 6.13: Fitted lifetime and scale factor variations for different assumed beam spot σ_y

In the second case the random movement of the beam spot results in an effective beam spot y width ($\sigma_{eff} = \sigma_y \oplus \sigma_{random}$) that is bigger than the generated and the assumed one. In this case the errors are underestimated, and the scale factor for the errors increases with increasing spreads (fig. 6.5).

The third case is analogous to the second, because a fixed bias in y is randomized by the fact that the direction of the momentum of the D^0 is isotropically distributed in the transverse plane (fig. 6.5).

The results of this Monte Carlo study give to us a feeling of how weel we can recover from an over/under estimatoin of the errors and of what is the effect of an uncertainty on the beam spot on the fit result which is summarized in tab. 6.3. However the systematic uncertainity is extracted from the fit of the data with different assumed beam spots.

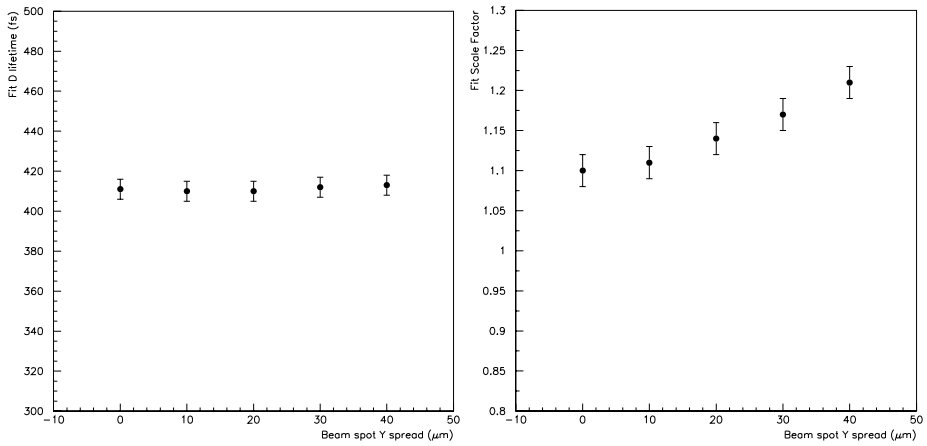

Figure 6.14: Fitted lifetime and scale factor variations for different assumed beam spot y random movements

B.S. Parameter	τ_{D^0} Variation
assumed σ_y	$\delta\tau = ^{+1}_{-0}\ fs$
assumed y bias	$\delta\tau = ^{+0}_{-5}\ fs$
assumed y spread	$\delta\tau = ^{+2}_{-1}\ fs$

Table 6.3: Variation of the lifetime on MC signal events when beam spot parameters are variated

6.6 Data-Monte Carlo background

The background samples generated has been selected and then rescaled to the luminosity of the used sample (8.33 fb^{-1}). In figure 6.16 (in log. scale) the various contributions to the invariant mass are shown, from which we can note that the $K\pi$ channel has much lower background than the $K\pi\pi\pi$ and the dominant contribution comes from $c\bar{c}$ events. The selection of high momentum D^0 eliminates the physical background from $b\bar{b}$, while the requirement of the slow pion eliminates the one from uds events. The remaining $c\bar{c}$ background originates from events in which we have one or more charmed meson (D^0, D^+, D_s^+).

Since the $K\pi$ final state has a very low multiplicity the background to the $D^0 \to K^-\pi^+$ decay mode can come from channels with higher multiplicity

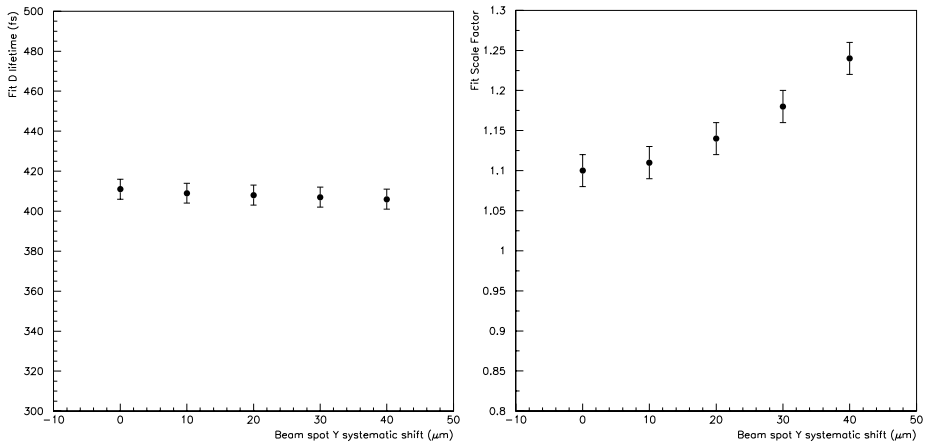

Figure 6.15: Fitted lifetime and scale factor variations for different assumed beam spot y shifts

(such as $D^0 \to K^-\pi^+\pi^0$) in which some of the final state particles are lost (π^0) and the reconstructed mass ends up on the left side of the peak. In the $K\pi\pi\pi$ the background, mainly combinatoric, originates from random combinations of tracks from charmed mesons and other tracks in the event.

The proper time distribution for background selected in a $\pm 60\,\mathrm{MeV}$ mass region around the D^0 mass is shown also shown in figure 6.17 The statistic is too small to perform a complete fit but we can note that the distribution of the background has a lifetime similar to the one of the signal. This is consistent with the composition of the background that we have extracted above, and the fact that most of the background comes from tracks originating from charmed mesons.

6.7 Likelihood definition and fit method

In the following we will describe the maximum likelihood fit method for the D^0 lifetime.

In order to minimize the systematic error we avoid extracting any of the parameters of the likelihood function from the Monte Carlo. The background properties are extracted from the data itself selecting the candidates to fit in a wide mass window of $\pm 60\,\mathrm{MeV}$ around the D^0 mass. This includes the signal pueak and the sidebands of the mass distribution (tab 6.4).

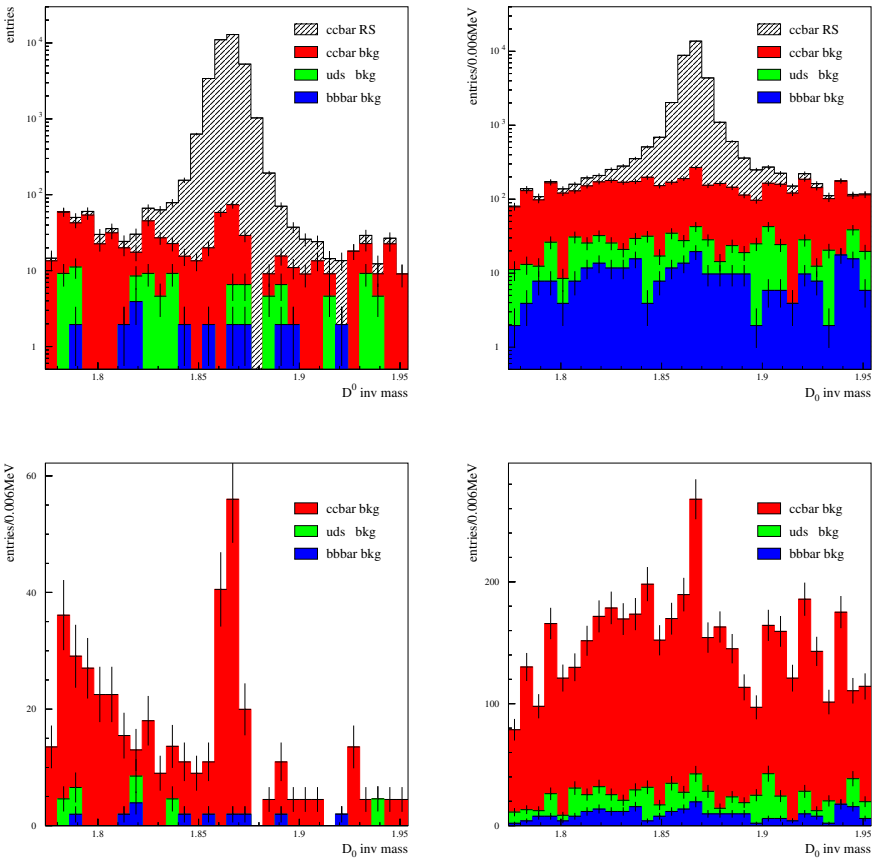

Figure 6.16: Invariant mass ditribution for MC events for $D^0 \to K^-\pi^+$ (left) and $D^0 \to K^-\pi^+\pi^-\pi^+$ (right), log (above) and linear (below) scale, the various contributions are shown. Plot below does not include signal events

Channel	Events selected
$D^0 \to K^-\pi^+$	23083
$D^0 \to K^-\pi^+\pi^-\pi^+$	21387

Table 6.4: Total number of events selected in the $\pm 60\,\mathrm{MeV}$ mass window used for maximum likelihood fit

For each D^0 candidate we reconstruct the flight length d and the momentum $p_T(D^0)$ in the direction perpendicular to the z beam spot axis. We

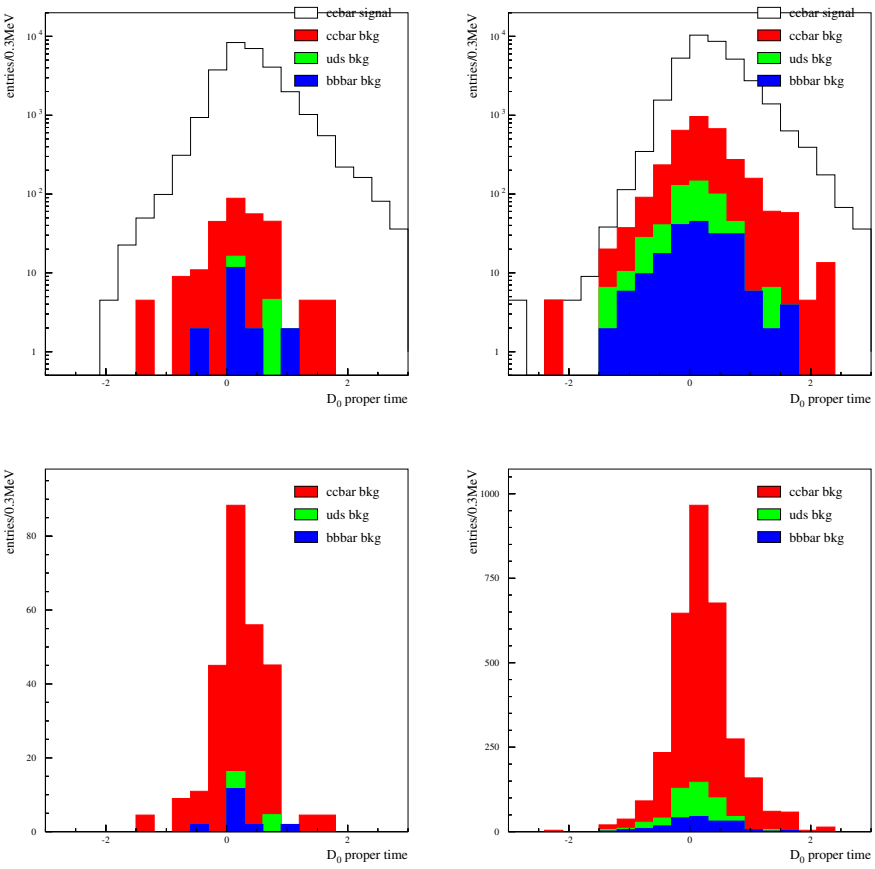

Figure 6.17: Proper time ditribution for MC events for $D^0 \to K^-\pi^+$ (left) and $D^0 \to K^-\pi^+\pi^-\pi^+$ (right), signal + background in log. scale (above) and background only in linear scale (below). The various contributions from $c\overline{c}$, $b\overline{b}$, uds are shown

compute the proper time and its error with the following formula:

$$t_i = \frac{M_{D^0}\ d_i}{p_T} \qquad \sigma_{t,i} = \frac{M_{D^0}\ \sigma_{d,i}}{p_T} \tag{6.5}$$

where M_{D^0} is the Particle Data Group D^0 mass, d_i is the signed transverse distance of flight for the i-th event, and $\sigma_{d,i}$ is the corresponding error, p_T is the transverse D^0 momentum.

In order to compute the signal probability we fit the D^0 invariant mass distribution with a double Gaussian plus a linear background as shown in fig

6.6 and compute the event by event probability as a function of the measured mass

$$p_{sig}(m_i) = \frac{g2(m_i)}{g2(m_i) + p1(m_i)} \tag{6.6}$$

where m_i is the reconstructed invariant mass of the i-th event, $g2(m_i)$ is the sum of 2 Gaussian functions with the same mean (and represents the signal) and $p1(m_i)$ is a linear background.

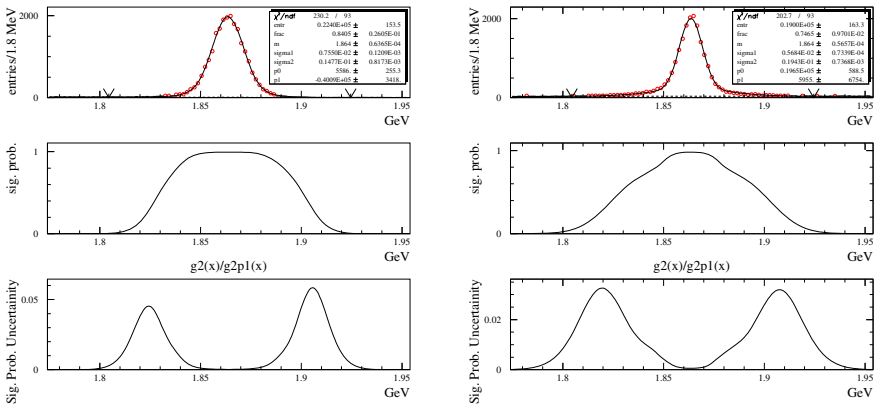

Figure 6.18: mass distribution, signal probability as a function of mass, error on the signal probability as a function of mass

The likelihood input quantities that are measured event by event are summarized in table 6.5.

Parameter	Description
t_i	proper time
$\sigma_{t,i}$	proper time error
$p_{sig}(m_i)$	event by event signal probability

Table 6.5: Event by event input quantities for the likelihood function

The likelihood function takes into account the signal ($\mathcal{S}$) and the background ($\mathcal{B}$) distribution weighted with he signal probability

$$\mathcal{L} = p_{sig}(m_i)\mathcal{S} + (1 - p_{sig}(m_i))\mathcal{B}. \tag{6.7}$$

Each of the two distributions will be the convolution of the physical ($\mathcal{P}_{\mathcal{S}/\mathcal{B}}$) function with the detector resolution ($\mathcal{R}_{\mathcal{S}/\mathcal{B}}$)

$$\begin{aligned} \mathcal{S} &= \mathcal{P}_{\mathcal{S}} \otimes \mathcal{R}_{\mathcal{S}} \\ &= \int_{-\infty}^{+\infty} \mathcal{P}_{\mathcal{S}}(t')\mathcal{R}_{\mathcal{S}}(t,t')dt' \qquad (6.8) \\ \mathcal{B} &= \mathcal{P}_{\mathcal{B}} \otimes \mathcal{R}_{\mathcal{B}} \\ &= \int_{-\infty}^{+\infty} \mathcal{P}_{\mathcal{B}}(t')\mathcal{R}_{\mathcal{B}}(t,t')dt' \qquad (6.9) \end{aligned}$$

The $\mathcal{P}_{\mathcal{S}}$ function for the signal is a pure exponential with constant τ_{D^0}

$$\mathcal{P}_{\mathcal{S}}(t|\tau_{D^0}) = E(t|\tau_{D^0}) \qquad (6.10)$$

where $E(t|\tau) = \frac{\theta(t)}{\tau}e^{-t/\tau}$ while the background proper time p.d.f is parameterized with a fraction $f_{\tau bg}$ with lifetime different from zero (τ_{bg}) plus a zero lifetime p.d.f. $\delta(t)$

$$\mathcal{P}_{\mathcal{B}}(t|\tau_{bg}, f_{\tau bg}) = f_{\tau bg}E(t|\tau_{bg}) + (1 - f_{\tau bg})\delta(t) \qquad (6.11)$$

The combinatorial background is generated by tracks coming from other charmed mesons (D^0, D^+, D_s^+) as well as from tracks coming from the primary vertex. As a result of this the mean value of the flight length of the background is roughly the mean of the charmed mesons lifetimes weighted with the relative fractions. The resulting p.d.f is not a single exponential distribution but the sum of serveral exponentials. We choose to parameterize the background shape in the simpler way (with a single exponential) in order to reduce the number of parameters to fit, taking into account that the background parameters are determined essentially only by the background events on the side bands and the number of background events is very low.

The resolution function ,in principle, is not equal for signal events and for background events. We can check the resolution for signal events on the Monte Carlo comparing the "true" position of the vertex with the reconstructed one (fig. 6.12) but for background events we don't have a single "true" vertex of origin for the D^0 candidate and we can not compute the resolution function. What we have done is to choose a form of the resolution function based on MC studies of signal events and use for the background one of the same form.

We take the resolution function of the form

$$\mathcal{R}(t,t') = (1-f_{mis})G(t,t',S_1\sigma_{t'}) + f_{mis}G(t,t',\sigma_{mis}). \tag{6.12}$$

where $G(x,x',\sigma_{x'}) = \frac{1}{\sigma_{x'}\sqrt{(2\pi)}}e^{(-(x-x')^2/2\sigma^2_{x'})}$ is a Gaussian distribution. The error $\sigma_{t'}$ is computed for each candidate, while σ_{mis} is a common width and S_1 is a global scale factor for the errors. f_{mis} and σ_{mis} represent the fraction and width of the tail of th distribution.

We use for the background the same functional form for the resolution function but we allow a different scale factor for the errors S_2.

The whole likelihood function used is shown below:

$$\begin{aligned}
&\mathcal{L}(\tau_{D^0}, S_1, S_2, f_{mis}, \sigma_{mis}, f_{\tau bg}, \tau_{bg}) = \\
&\int_{-\infty}^{+\infty} dt' \underbrace{p_{sig}E(t'|\tau_{D^0})}_{\mathcal{P}_\mathcal{S}} \underbrace{((1-f_{mis})G(t,t',S_1\sigma_{t'}) + f_{mis}G(t,t',\sigma_{mis}))}_{\mathcal{R}_\mathcal{S}} + \\
&\underbrace{+(1-p_{sig})\left(f_{\tau bg}E(t'|\tau_{bg}) + (1-f_{\tau bg})\delta(t')\right)}_{\mathcal{P}_\mathcal{B}} \\
&\underbrace{((1-f_{mis})G(t,t',S_2\sigma_{t'}) + f_{mis}G(t,t',\sigma_{mis}))}_{\mathcal{R}_\mathcal{B}}
\end{aligned} \tag{6.13}$$

In conclusion the likelihood depends upon 7 parameters, of which:

- the relevant physical quantity:
  - τ_{D^0} the D^0 meson lifetime
- the resolution function:
  - the signal scale factor S_1,
  - the bkg scale factor S_2,
  - the fraction of mismeasured events f_{mis}
  - the width of the mismeasured events σ_{mis}
- the background properties:
  - the fraction of flying background $f_{\tau bg}$
  - the lifetime of the background τ_{bg}

All of them are free parameters of the likelihood. Background properties are determined by the events in the sidebands that have $p_{sig} \simeq 0$, and in our case are very few. The resolution function and the lifetime are determined respectively by the negative and the positive side of the proper time distribution.

6.8 Consistency Checks

D^0 vertex pull and flight length pull demonstrate that the reconstruction algorithm is capable of computing the flight length without any bias and with correct errors. In the following we are going to investigate some other consistency checks in detail.

6.8.1 Efficiency versus proper time

The "physical function" $\mathcal{P}_S$ that describes the decay of the particle could be distorted if the selection efficiency depends on the value of the generated proper time.

To verify that the selection efficiency does not depend on the proper time we used our signal Monte Carlo events. We generated 106 000 signal events of $D^0 \to K^-\pi^+$ and $D^0 \to K^-\pi^+\pi^-\pi^+$ events and we applied to the sample the selection criteria described in 6.2.3. We divided the sample in bins of generated proper time and compared the expected number of events in each bin with the measured one.

The result can be seen in fig. 6.19, shows a nicely flat distribution for the efficiency as a function of the proper time, also at decay times corresponding to several D^0 lifetimes.

In addition the result of the fit (on MC data) of the true proper time distribution with a pure exponential function is compatible with the generated lifetime.

6.8.2 Signal MC fit

At this point we can apply the selection and the fitting procedure to the Monte Carlo signal. The fit results are summarized in table 6.6 below The events were generated with a lifetime of 415 fs. The data were fitted using

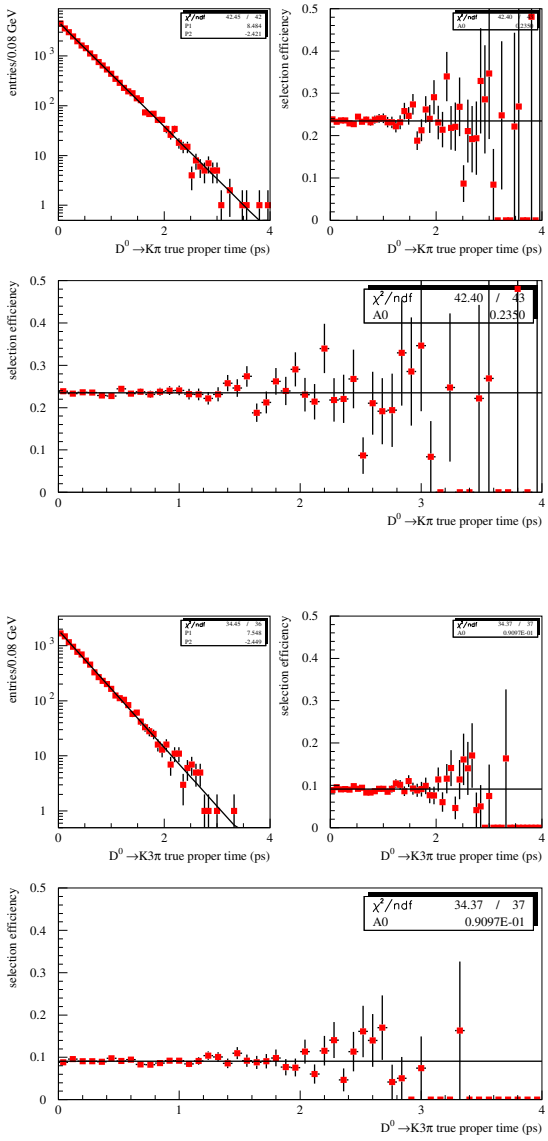

Figure 6.19: Selection efficiency of $D^0 \to K^-\pi^+$ and $D^0 \to K^-\pi^+\pi^-\pi^+$ candidates as a function of the proper time

only the signal part of the likelihood (this means setting the signal probability to 1) and fixing f_{mis} to zero. The results are well compatible with the generated lifetime.

Parameters	M.C. $D^0 \to K^-\pi^+$	M.C. $D^0 \to K^-\pi^+\pi^-\pi^+$
τ_{GEN}	$415.0 fs$	$415.0 fs$
τ_{D^0}	$412.0 \pm 3.1\ fs$	$411.9 \pm 4.7\ fs$
S_1	1.13 ± 0.01	1.09 ± 0.01

Table 6.6: Fit results for Monte Carlo events

6.8.3 Control checks

We divide our dataset in subsamples on which τ should not depend on and we perform the full likelihood fit on each subsample.

The variables that we have used are sensitive to SVT local alignment, to the dominant source of error on the flight length (D^0 vertex or beam spot), amount of traversed material, y position of the beam spot, background properties.

- D^0 momentum
- ϕ_{D^0} : sensitive to local alignment
- ϕ'_{D^0} : sensitive to the type of error on the f.l. and to alignment
- θ : sensitive to the fwd/bwd asymmetry and the amount of traversed material
- mass cut : sensitive to background properties
- data-set

The ϕ_{D^0} variable is the polar angle of the D^0 momentum vector and is defined as $\arctan(P_{y,D^0}, P_{x,D^0})$ in $[-\pi, \pi]$, ϕ'_{D^0} is the acute angle between the D^0 momentum direction and the x axis and is defined as $\arctan(|P_{y,D^0}|, |P_{x,D^0}|)$, θ is the azimuthal angle. In fig. 6.20 the fit results are shown.

The plots show some dependence of the fitted lifetime on the polar angle and on ϕ' that is similar for the two decay modes.Their effect will be included in the systematic error calculation.

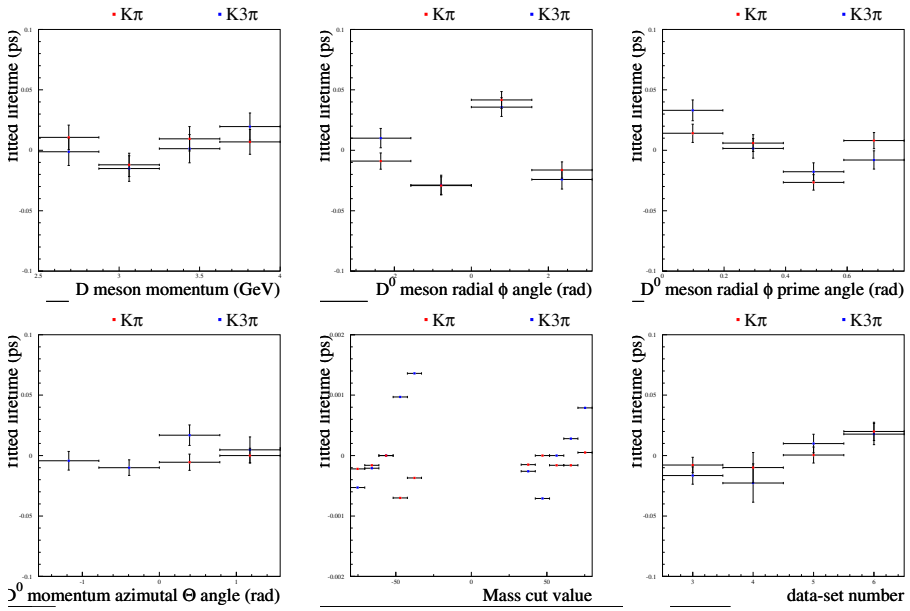

Figure 6.20: Summary of control check plots for $D^0 \to K^-\pi^+$ (red) and $D^0 \to K^-\pi^+\pi^-\pi^+$ (blue): The plots show the difference of the fitted lifetime w.r.t to the full set

6.9 Systematic errors

In this section we discuss the systematic errors estimates on the measured D^0 lifetime. We can divide the systematic uncertainties into two categories:

- Decay length / proper time measurement
  - Decay length
  - Beam spot size and position
  - Global detector scale
  - ϕ non uniformity
- Lifetime fit
  - Background properties
  - Signal probability

6.9.1 Decay length

In section 6.4 we have already shown that on Monte Carlo events the vertex position is not biased w.r.t to the true one and the errors are computed correctly. We have also shown that the proper time distribution is not biased.

As usual the actual detector is something different and we do not thrust the results only on the Monte Carlo but we need a way to verify this also on the data. We need to identify a zero lifetime sample of events and test our algorithms to check that the flight length of this sample has a zero lifetime distribution, i.e. a Gaussian distribution with zero mean.

To determine this bias we used $\gamma\gamma \to 4$ *prongs* events that is a zero lifetime sample because all the four tracks originate in the Interaction Point.

$\gamma\gamma$ Selection
$\sum_i p_t(i) < 100\,\mathrm{MeV}/c$
$E_{CAL} < 0.9\,\mathrm{GeV}$
$\mathrm{d}E/\mathrm{d}x_{DCH}$ compatible with π hypothesis
same-sign pair rejection

Table 6.7: $\gamma\gamma$ selection [41]

They can be selected (table 6.7) with a very low background (0.2% of $\tau\tau$ and 0.3% of $c\bar{c}$) but they have a momentum range quite different w.r.t. to the D^0 daughters tracks. In fact in the decay channel $D^0 \to K^-\pi^+$ the daughters have an average momentum of about $2\,\mathrm{GeV}/c$ while the pions from $\gamma\gamma$ events have an average momentum of about $0.5\,\mathrm{GeV}/c$. For this reason there could be a concern because the multiple scattering contribution is different in the two cases and is not obvious that the errors are well computed in the $\gamma\gamma$ case. Anyway the central value should not be spoiled and is acceptable to estimate the bias on the flight length from the mean value of the distribution of the distance of flight of opposite charged tracks.

The results can be summarized in a mean flight length bias of

- $< f.l. >= -2.80 \pm 0.45\,\mu\mathrm{m}$

that can be translated into a proper time correction factor using the average $\beta\gamma c$ in the transverse plane of $0.438\,\mu\mathrm{m/fs}$ leading to

- $\delta t = +6.4 \pm 1\ fs$

This value represents a net negative bias in the measurement of the proper time and the final result will be corrected for it while the error will be included in the systematic error.

6.9.2 Beam spot size

The calculation of the f.l. depends on the beam spot position and size since we constrain the D^0 to come from the beam spot.

The size of the beam spot used in the χ^2 minimization is not the value around $40\,\mu$m that is in the database, but a fixed value of $10\,\mu$m, because we know from luminosity considerations that the size has to be around $6-7\,\mu$m, but has large uncertainties.

The size that we use is somehow arbitrary and the actual size can vary from run to run of from 10 to 20 μm. The variation of the fitted lifetime when we vary the beam spot size and position has to be taken into account as a systematic error.

We have studied the effect of a variation of the beam spot assumed y size ($\sigma_y = 4, 10, 30, 50\,\mu$m), y position ($y = 10, 20, 30, 40\,\mu$m), *spread* of y position ($spread = 10, 20, 30, 40$) on the fitted lifetime on Monte Carlo events as discussed in more detail in 6.5, and we have found a variation $\delta t = ^{+2}_{-5}$ fs. Furthermore the variation of the beam spot parameters causes also a variation of the scale factor S_1 to compensate the under/over estimation of the errors.

The estimate of the systematic has been done reconstructing all the events with 3 different beam spot: $\sigma_y = 20\,\mu$m, y position shift $= +10\,\mu$m, y position shift $= -10\,\mu$m. We find differences summarized in table 6.8.

Decay channel	shift $= +10\,\mu$m	shift $= -10\,\mu$m	$\sigma_y = 20\,\mu$m
$D^0 \to K^-\pi^+$	$-0.41\ fs$	$+0.36\ fs$	$+0.00\ fs$
$D^0 \to K^-\pi^+\pi^-\pi^+$	$-0.51\ fs$	$+1\ fs$	$+0.24\ fs$

Table 6.8: Summary of beam spot related systematic errors

6.9.3 Global detector scale

Since we are measuring an absolute value for the lifetime we need to know the absolute scale of the detector transverse dimensions. If the global detector scale (i.e. the scale of the SVT and the DCH) is wrong with respect to what we use in the reconstruction code, we expect the same systematic effect in the decay length measurement (dominated by the SVT) and in the D^0 momentum calculation (dominated by the DCH).

Since in the formula 6.5 we have only the ratio between the two, the effect of a wrong global detector scale is a second order effect and will be negligible.

If only one of the two scales is wrong the effect on the lifetime will be a first order effect and need to be considered in detail.

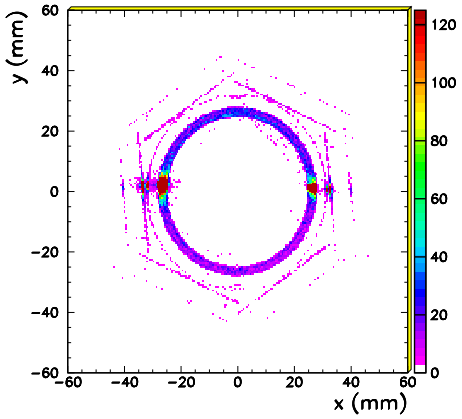

Figure 6.21: Proton radiography of the beam pipe and SVT

In order to determine the absolute transverse detector scale the survey measurements of the beam pipe radius have been compared with the proton radiography of the beam pipe (fig. 6.21).

The method consists in selecting events with the interaction of a background particle with a nucleon of the beam pipe in which a well identifiable proton is produced. The radial position of the vertices is accumulated after correcting for the beam pipe tilt. The distribution is then fitted taking into account the different materials of which the beam pipe is composed and the radius of the beam pipe is extracted. The comparison of the fitted value with the survey one shows that the absolute radial scale of the SVT detec-

tor is $99.927\% \pm 0.03\%$. This means that a distance is measured with an underestimation of $-0.073\% \pm 0.03\%$. the correction factor for the proper time is then

$$\delta t = +0.3 \pm 0.1 \; fs \tag{6.14}$$

6.9.4 ϕ non uniformity

As we have seen previously there is some dependency of value of the fitted lifetime on the ϕ azimuthal angle of the D^0 momentum direction. This is an indication of a distortion of the the SVT w.r.t. the alignment used. This distortion can eventually introduce some global bias in the decay length measurement, that can be corrected using the result on the zero lifetime sample $\gamma\gamma \to 4 \; prongs$. However, even if the mean value can be corrected, statistical fluctuations of the number of events in one ϕ region or the other can modify the value of the mean decay length measurement. In a pessimistic view we suppose to separate the data in two subsamples with a bias respectively of $+\delta$ and $-\delta$ with δ the maximum difference from the mean $= 50 \; fs$. The error on the mean will be simply

$$\delta t = \frac{\delta}{\sqrt{N/2}} = 0.5 \; fs \tag{6.15}$$

6.9.5 Background properties

We select the events in wide invariant mass region of $\pm 60\,\mathrm{MeV}$ around the D^0 mass to include the events in the side-bands of the mass peak. This choice of the mass region is somehow arbitrary and its variation consists only in an addition or subtraction of a few background events.

We consider a dependence of the lifetime from the chosen mass region an effect of our misunderstanding of the background properties and we include it in the systematic error.

We vary upper and lower bound of the region in the range $[-80\,\mathrm{MeV}, -40\,\mathrm{MeV}]$ $[+40\,\mathrm{MeV}, +80\,\mathrm{MeV}]$ and consider the differences as systematic errors due to our lack of knowledge of the background. The results are summarized in table 6.9.5

Decay channel	Upper/lower	40	50	70	80
$D^0 \to K^-\pi^+$	Lower bound	$-0.37\ fs$	$-0.7\ fs$	$-0.16\ fs$	$-0.21\ fs$
	Upper bound	$-0.15\ fs$	$-0.16\ fs$	$+0.1\ fs$	$+0.04\ fs$
$D^0 \to K^-\pi^+\pi^-\pi^+$	Lower bound	$+1.3\ fs$	$+1.0\ fs$	$-0.2\ fs$	$-0.55\ fs$
	Upper bound	$-0.26\ fs$	$-0.7\ fs$	$+0.28\ fs$	$+0.78\ fs$

Table 6.9: Lifetime differences for variations of mass region bounds

6.9.6 Signal Probability systematic

The event by event signal probability defined in eq. 6.6 is obtained from the fit of the invariant mass distribution. It is an input quantity of the likelihood function and has its own error so is source of systematic error. We vary the signal probability by raising or lowering all the probabilities of δP_{sig} wich is the fitted error on the signal probability. This corresponds to a error in the fit to the background level.

In addition we consider the fact that the error on the proper time is correlated with the fitted value of the the D^0 meson mass. If we vary the fitted value for the D^0 mass the signal probability decreases on one side while it increases on the other side. To consider this effect we vary the signal probability by $+1\ \sigma$ $(-1\ \sigma)$ if the reconstructed invariant mass difference w.r.t to the fitted value is positive (negative) and vice-versa. We call this variation $\delta P_{sig}\frac{m_{D^0}-m_i}{|m_{D^0}-m_i|}$. The differences on the fitted lifetime are shown in table 6.10

decay channel	$\delta\tau$ for $\pm\delta P_{sig}$ variations	$\delta\tau$ for $\pm\delta P_{sig}\frac{m_{D^0}-m_i}{\lvert m_{D^0}-m_i\rvert}$ variations
$D^0 \to K^-\pi^+$	$^{-0.14}_{-0.01}\ fs$	$^{+0.24}_{-0.49}\ fs$
$D^0 \to K^-\pi^+\pi^-\pi^+$	$^{+0.01}_{-0.02}\ fs$	$^{+0.58}_{-0.63}\ fs$

Table 6.10: Signal probability systematic

6.10 Total systematic error

The various sources of systematic uncertainty on the result are summarized in table 6.11. The total systematic uncertainity has been computed assuming no correlation between the various sources. The most important source of error is the decay lenght measurement obtained from the $\gamma\gamma$ control sample, but the background region definition and the ϕ non uniformity are also noticeable.

	$D^0 \to K^-\pi^+$	$D^0 \to K^-\pi^+\pi^-\pi^+$
decay length	$+6.4 \pm 1\ fs$	$+6.4 \pm 1\ fs$
ϕ non unif.	$\pm 0.5\ fs\ fs$	$\pm 0.5\ fs$
beam spot	$^{+0.36}_{-0.41}\ fs$	$^{+1}_{-0.51}\ fs$
background	$^{+0.0}_{-0.7}\ fs$	$^{+1.3}_{-0.7}\ fs$
signal probab.	$^{+0.24}_{-0.5}\ fs$	$^{+0.58}_{-0.63}\ fs$
radial scale	$+0.3 \pm 0.1\ fs$	$+0.3 \pm 0.1\ fs$
TOTAL	$+6.7^{+1.2}_{-1.5}\ fs$	$+6.7^{+2.1}_{-1.5}\ fs$
MC	$+3 \pm 3.1\ fs$	$+3.1 \pm 4.7\ fs$

Table 6.11: Summary of systematic errors

6.11 Final results

The results of the unbinned maximum likelihood fit are summarized in table 6.12. The errors are statistical errors from the maximum likelihood fit and the correlation matrix is also shown for completeness.

The result of this work is to be compared to the results from CLEO, BELLE, FOCUS and E791. The BELLE [45] analysis is similar to this work but is carried out without the D^* tag requirement, and thus has access to a higher statistic but with an increased background and has not quoted a systematic error. E791 [46] and FOCUS [47] are both fixed target experiments which have access to an extremely high statistic, while the CLEO [48] analysis is very similar to this work but has a lower statistical sample. The various results are compared in table 6.15.

Parameters	$D^0 \to K^-\pi^+$	$D^0 \to K^-\pi^+\pi^-\pi^+$
τ_{D^0}	$404.4 \pm 3.4\ fs$	$405.7 \pm 4.0\ fs$
S_1	1.20 ± 0.02	1.12 ± 0.014
S_2	2.42 ± 0.17	1.33 ± 0.05
$f_{\tau_{Bkg}}$	64 ± 27 %	70 ± 7 %
τ_{Bkg}	$3.6 \pm 1.3\ 10^2\ fs$	$341 \pm 33\ fs$
f_{mis}	11 ± 2.4 %	2.2 ± 1.3 %
σ_{mis}	$307 \pm 34\ fs$	$6.1 \pm 1.1\ 10^2\ fs$

Table 6.12: Fit results for the $D^0 \to K^-\pi^+$and $D^0 \to K^-\pi^+\pi^-\pi^+$decay modes

Correlations	τ_{D^0}	S_1	S_2	$f_{\tau_{Bkg}}$	τ_{Bkg}	f_{mis}	σ_{mis}
τ_{D^0}	1.000	-0.031	-0.049	-0.109	-0.020	-0.038	-0.047
S_1	-0.031	1.000	-0.911	-0.042	-0.168	-0.008	-0.643
S_2	-0.049	-0.911	1.000	0.040	0.159	0.048	0.637
$f_{\tau_{Bkg}}$	-0.109	-0.042	0.040	1.000	0.499	-0.753	0.149
τ_{Bkg}	-0.020	-0.168	0.159	0.499	1.000	-0.599	0.321
f_{mis}	-0.038	-0.008	0.048	-0.753	-0.599	1.000	-0.204
σ_{mis}	-0.047	-0.643	0.637	0.149	0.321	-0.204	1.000

Table 6.13: Correlation matrix from mamimum likelihood fit for $D^0 \to K^-\pi^+$decay mode

6.12 Summary and Conclusions

The study for the measurement of the D^0 meson lifetime using e^+e^- annihilation data collected with the *BABAR* detector near the $\Upsilon(4S)$ resonance is presented. D^0 mesons are reconstructed in the decay modes $D^0 \to K^-\pi^+$, $D^0 \to K^-\pi^+\pi^-\pi^+$. The charmed mesons are selected from $c\overline{c}$ events and the flight length is reconstructed assuming the beam spot region as their production point.

The results of the analysis are summarized in tables 6.15, 6.16.

Correlations	τ_{D^0}	S_1	S_2	$f_{\tau_{Bkg}}$	τ_{Bkg}	f_{mis}	σ_{mis}
τ_{D^0}	1.000	-0.174	-0.037	-0.196	-0.017	-0.039	0.088
S_1	-0.174	1.000	-0.735	0.035	-0.082	0.091	-0.429
S_2	-0.037	-0.735	1.000	0.054	0.097	-0.083	0.333
$f_{\tau_{Bkg}}$	-0.196	0.035	0.054	1.000	-0.381	0.218	-0.220
τ_{Bkg}	-0.017	-0.082	0.097	-0.381	1.000	-0.844	0.016
f_{mis}	-0.039	0.091	-0.083	0.218	-0.844	1.000	-0.150
σ_{mis}	0.088	-0.429	0.333	-0.220	0.016	-0.150	1.000

Table 6.14: Correlation matrix from max. likelihood fit for $D^0 \rightarrow K^-\pi^+$decay mode

CLEO	$408.5 \pm 4.1^{+3.5}_{-3.4}\ fs$
E791	$413 \pm 3 \pm 4\ fs$
BELLE	$414.5 \pm 1.7\ fs$
FOCUS	$409.2 \pm 1.3\ fs$
This work	$414.4 \pm 2.6 \pm 2.8\ fs$

Table 6.15: Comparison of result with other experiments

$\tau_{D^0 \rightarrow K^-\pi^+}$	$414.1 \pm 3.4\ fs\ (stat) \pm 3.1\ fs\ (MC)^{+1.2}_{-1.5}\ fs\ (syst)$
$\tau_{D^0 \rightarrow K^-\pi^+\pi^-\pi^+}$	$415.4 \pm 4.0\ fs\ (stat) \pm 4.7\ fs\ (MC)^{+2.1}_{-1.5}\ fs\ (syst)$

Table 6.16: Final results

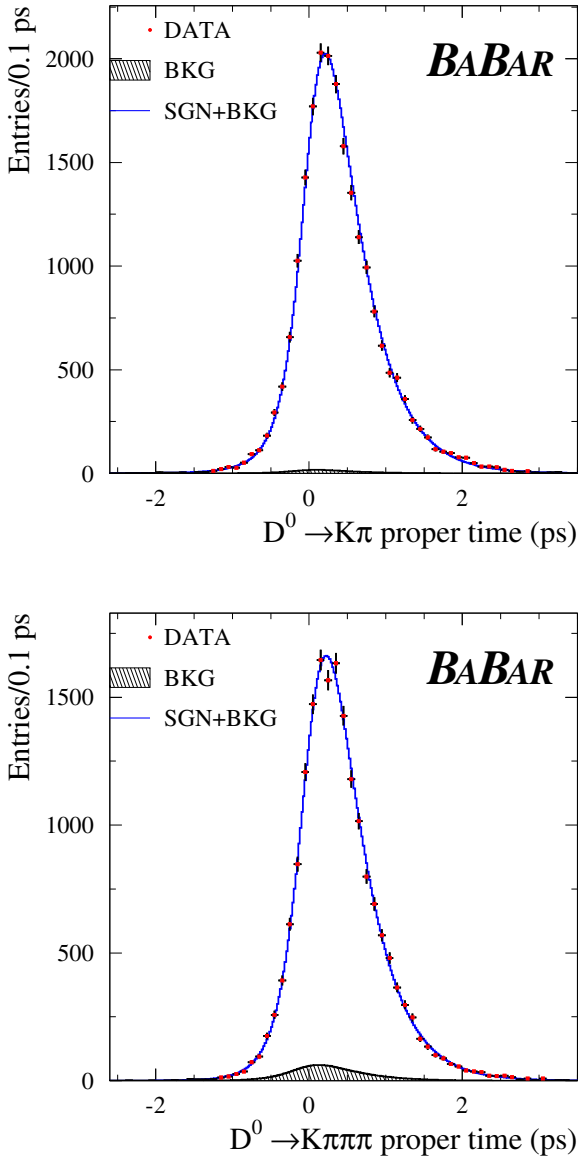

Figure 6.22: Fitted proper time distribution for $D^0 \to K^-\pi^+$,$D^0 \to K^-\pi^+\pi^-\pi^+$ (linear scale)

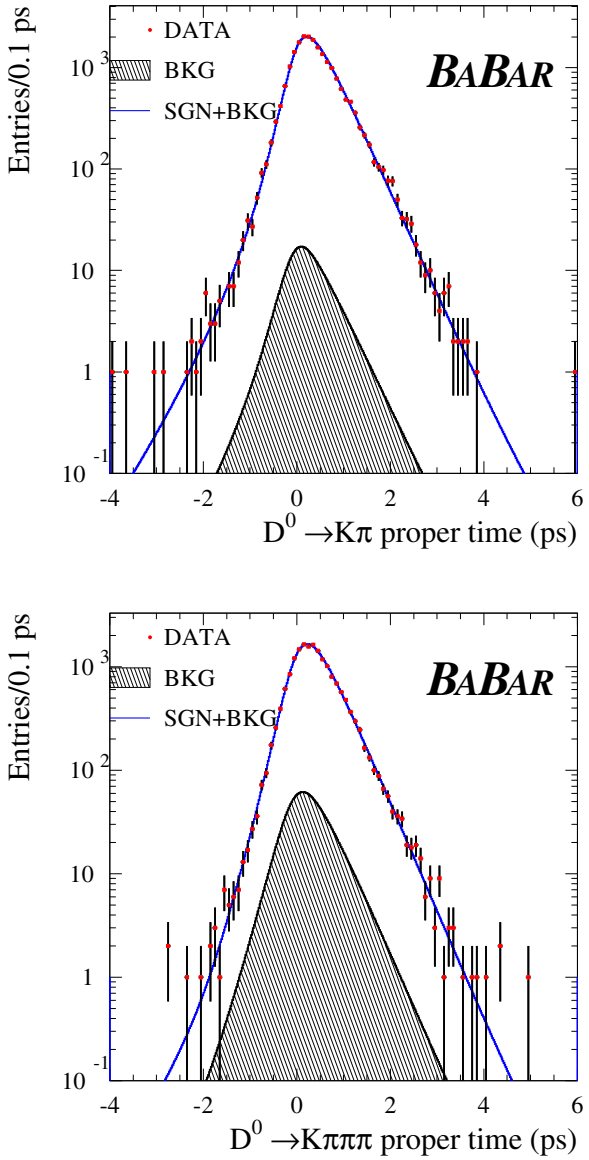

Figure 6.23: Fitted proper time distribution for $D^0 \to K^-\pi^+$,$D^0 \to K^-\pi^+\pi^-\pi^+$ (log scale)

Appendix A

Future developments

A.1 D mixing with doubly Cabibbo suppressed decays

As a natural development for this analysis we foresee the extraction of limits on D mixing parameters (eq. 1.3.1) using the interference of the doubly Cabibbo suppressed decay ($D^0 \to K^+\pi-$) of the D^0 meson with the mixed decay ($D^0 \to \overline{D}^0 \to K^+\pi^-$). In the following for brevity we will refer to the decay chain $D^{*+} \to (K^-\pi^+)\pi_s^+$ (and its complex conjugate) as the right sign decay (RS) and the $D^{*+} \to (K^+\pi^-)\pi_s^+$ as the wrong sign decay (WS) because of the charge of the two pions.

This very preliminary analysis is aiming the extraction of the doubly Cabibbo suppressed signal to be used in the study of the mixing of D^0. The underlying idea is the fact that the selection of the sample is completely similar to the one for the D^0 lifetime measurement and the results of the lifetime measurement (the lifetime itself and the resolution function) can be used as input parameters in the fit of the mixing parameters.

The WS decay mode is reconstructed using a pair of opposite charged hadrons h^+h^- to form the D^0. The pion mass is assigned to the negative hadron (the one with charge opposite to the slow pion π_s^+), the kaon mass to the positive one. This choice of the mass hypothesis is the opposite of what used in the RS decay. This is almost the only difference w.r.t. the D^0 lifetime selection. The other difference is a choice of tighter particle identification criterion to increase the signal to background ratio. The rest

of the selection is identical to the RS selection previously described and is summarized in the following:

Parameters	criterion	Parameters	criterion
Track quality	required	$p^{cm}(D^*)$	$> 2.5\,\mathrm{GeV}$
$P(K)$,$P(\pi)$	$> 0.250\,\mathrm{GeV}$	$\mathcal{P}(\chi^2_{D^0})$	$> 1\%$
$Pt(\pi_s)$	$> 0.070\,\mathrm{GeV}$	$\mathcal{P}(\chi^2_{refit})$	$> 1\%$
PID_K, PID_π	tight	σ_d	$< 300\,\mu\mathrm{m}$
$\mathrm{d}E/\mathrm{d}x_{SVT}(\pi_s)$	> 1.5	$\lvert\Delta M - 145.4\,\mathrm{MeV}\rvert$	$< 600\,\mathrm{keV}$

Table A.1: Selection criteria for the D^0 candidates

The two D^0 tracks are required to pass standard quality criteria and have a momentum greater than 250 MeV/c. The soft pion is used to form the D^* candidate and the mass difference between the D^0 and the D^* allows for an important reduction of the combinatoric background. The D^* momentum greater than 2.5 GeV is required in order to reject events from $b\bar{b}$ decays. The D^0 vertex is required to be well reconstructed.

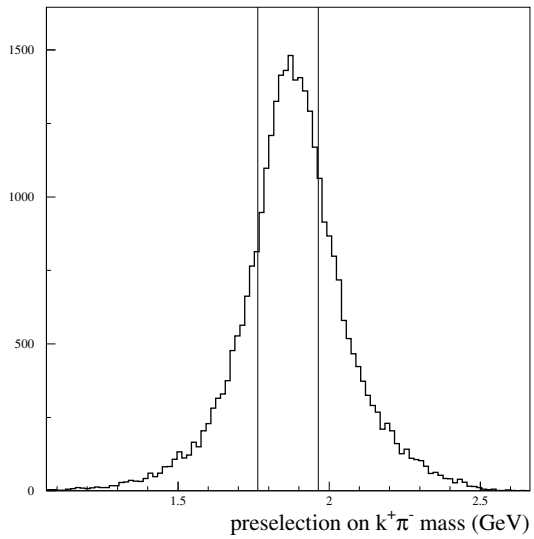

Figure A.1: Preselection cut on invariant mass of the RS combination

The preselection of the data was originally chosen for the RS sign combi-

nation only, hence a cut on the D^0 invariant mass of $\pm 100\,\mathrm{MeV}$ around the nominal D^0 mass was applied. In the case of a WS decay this invariant mass distribution is much broader (fig. A.1) because the wrong mass hypothesis has been used for the h^+h^- combination, thus the selection efficiency is degraded by a factor 49.9%. For this reason the number of events found must be rescaled by a factor of about 2.

The selection has been applied to the available set of MC events (sec. 6.2.2) that has been rescaled and mixed accordingly to the production cross sections to evaluate the expected number of background events. The invariant mass distribution for data and MC events is shown in fig A.1. The

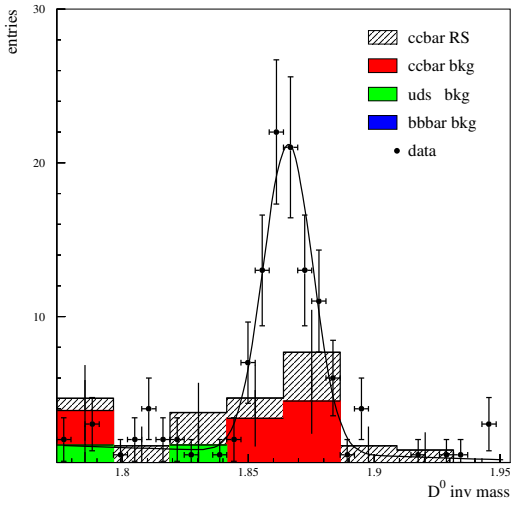

Figure A.2: Invariant mass distribution for WS decays: circles are data, Dashed is background from misidentified Right Sign decays in $c\overline{c}$ events, red is background from other $c\overline{c}$ events, green is uds, blue is $b\overline{b}$. Also shown the expected number of background events in a 2σ window.

statistic is poor but we can be seen that the background from $c\overline{c}$ events is dominant w.r.t. the one from generic uds and $b\overline{b}$ events. A significant part of the $c\overline{c}$ background (33%) is due to RS decays in which the two hadrons are both misidentified. In this case the invariant mass has a broad distribution with an RMS of $\sim 180\,\mathrm{MeV}$ and is thus almost flat in the D^0 mass peak region ($\langle\sigma\rangle \simeq 8.7\,\mathrm{MeV}$). The remaining 66% is peaked in the D^0 mass

region and is due to the $D^{*-} \to \overline{D}^0\pi^-$ RS decay ($\overline{D}^0 \to K^+\pi^-$) in which the negative pion is lost and a positive slow pion from the rest of the event is combined with the $\overline{D}^0$ to form a D^{*+} candidate.

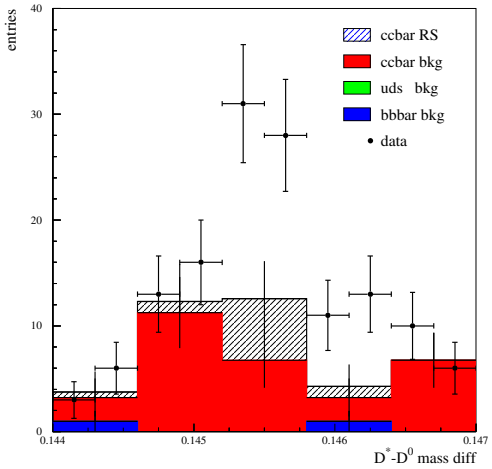

Figure A.3: $D^* - D^0$ mass difference distribution for WS decays: circles are data, dashed is background from misidentified Right Sign decays in $c\overline{c}$ events, red is background from other $c\overline{c}$ events, green is uds, blue is $b\overline{b}$

As an exercise we can extract the number of Wrong Sign decays subtracting the expected number of background events ($N_B = 47 \pm 13$) from the number of events obtained on real data in a 2σ window and correcting for the loss of efficiency in the preselection $\epsilon = 49.9\%$. We obtain $N_{WS} = \frac{40.7 \pm 15}{0.499} = 81 \pm 30$.

The number of WS decays can have contributions both from the doubly Cabibbo suppressed decay and from the mixed decay. If we assume that the mixing contribution is negligible the ratio $\frac{N_{WS}}{N_{RS}}$ gives directly the ratio of the branching ratios of the doubly Cabibbo suppressed to the Cabibbo favored mode R_{DCS}, obtaining a value of $R_{DCS} = 0.47 \pm 0.18\%$. [1]

If we consider also consider the possibility of mixing the two contributions can be disentangled in the proper time distribution (eq. 1.52)

$$r_{ws}(t) = e^{-t} \left|\bar{A}\right|^2 \left[R_{DCS} + \frac{r_{mix}}{2} t^2 + y' \sqrt{R_{DCS}} t\right] \qquad \text{(A.1)}$$

[1] Tree level S.M. prediction is $\sim \sin\theta_c^4 = 0.23\%$

The time t is measured in units of the D^0 meson lifetime, $\bar{A}$ is the cabibbo favoured amplitude, $R_{DCS} = |\lambda|^2$ where $\lambda = \frac{A}{\bar{A}}$ is the Doubly Cabibbo Suppresed rate, r_{mix} is the mixing rate and $y' = \frac{\Delta\Gamma}{2\Gamma}\mathcal{R}e\lambda + \frac{\Delta M}{\Gamma}\mathcal{I}m\lambda$

The doubly Cabibbo suppressed component has a pure exponential rate, the mixed component has a t^2 modulation and the interference has a t modulation. In order to fit the proper time distribution is necessary to know the resolution function and the background level. The D^0 lifetime value and the resolution function can be taken directly from the analysis of RS decays for the lifetime measurement since they must be the same. The background level can be fitted using the side bands of $m(D^0)$ and $m_{D^*} - m_{D^0}$ and the background shape can be fitted directly on data in the same way as for the lifetime analysis.

Thanks

Thanks to all the *BABAR* group pf Pisa for the support and the useful discussions. Special thanks to Matteo Rama for his contributions to the analysis.

Bibliography

[1] N. Cabibbo, M. Kobayashi, T. Maskawa, Prog. Th. Phys. , 49(1973) 652

[2] PEP-II An Asymmetric B Bactory, Conceptual Design Report, SLAC-418, LBL-PUB-5379 (1993)

[3] Letter of Intent for the Study of *CP* Violation and Heavy Flavor Physics at PEP-II, The BABAR Collaboration, SLAC-443 (1994)

[4] The *BABAR* Physics Book, Physics at an Asymmetric B Factory, P.F.Harrison and H.R.Quinn, Editors, SLAC-R-504, October, 1998.

[5] The Physics Program of a High-Luminosity Asymmetric B Factory at SLAC, SLAC-353 (1989), Proceedings of the Workshop on Physics and Detector Issues for a High Luminosity Asymmetric B-Factory at SLAC, SLAC-373 (1991), Proceedings of B Factories, The State of the Art in Accelerators, Detectors and Physics, SLAC-400 (1992).

[6] J. H. Christenson *et al.*, Phys. Rev. Lett. **13**, 138 (1964).

[7] M. Gronau and D. London, Phys. Rev. Lett. **65**, 3381 (1990).

[8] G. Bellini, I. I. Bigi and P. J. Dornan, Phys. Rept. **289** (1997) 1.

[9] I. I. Bigi and N. G. Uraltsev, Nucl. Phys. B **592** (2001) 92

[10] L. Wolfenstein, Phys. Rev. Lett. **51**, 1945 (1983).

[11] B. Blok, M. Shifman, "Lifetimes of charmed hadrons revisited. Facts and fancy", hep-ph/9311331

[12] G. Buchalla, A. Buras, M. Lautenbachen, "Weak decays beyond leading logarithms", hep-ph/9512380

[13] A. Di Giacomo, "Lezioni di fisica teorica", Edizioni ETS (1992)

[14] T.E. Browder and S. Pakavasa, Phys. Lett. **B 383**, 475 (1996).

[15] L. Wolfenstein, Phys. Rev. Lett. **75**, 2460 (1995).

[16] S. L. Glashow, J. Iliopoulos and L. Maiani, Phys. Rev. D **2**, 1285 (1970).

[17] A. Pich, Nucl. Phys. **66** (proc. suppl.), 456 (1998).

[18] M.Sullivan, *B*-Factory Interaction Region Designs, Proceedings of the IEEE Particle Accelerator Conference (PAC97), Vancouver, B.C. (1997); SLAC-PUB-7563.

[19] S.E. Csorna *et al.* (CLEO Collaboration), Phys. Rev. **D61**, 111101 (2000).

[20] Steven A. Lewis, "Overview of the Experimental Physics and idustrial Control System: EPICS", (2000)

[21] Francesco Safai Tehrani, "The Babar Prompt Reconstruction Manager: A Real Life Example of a Constructive Approach to Software Development.", submitted to Computer Physics Communications

[22] Objectivity/DB, Objectivity, Inc., 301B East Evelyn Avenue, Mountain View, California, 94041, USA.

[23] Private comunication with Prof. Mike Sulllivan

[24] B. N. Ratcliff, SLAC-PUB-5946 (1992); B. N. Ratcliff, SLAC-PUB-6067 (1993); P. Coyle et al., *Nucl. Instr. and Methods* **A343** (1994) 292.

[25] M. Benkebil*et al.*, *Nucl. Instr. and Methods* **A442**, 364 (2000).

[26] "The BaBar Technical Design Report"
D. Boutigny *et al.*, SLAC-R-457.

[27] R. Santonico, R. Cardarelli, Nucl. Instr. and Methods **A**187 (1981) 377.

[28] L.Lista, *Object Oriented Reconstruction Software for the IFR Detector of BABAR Experiment* in Proceedings of the Conference on Computing in High Energy Physics, Padova (Italy), 2000.

[29] A. Zallo et al., *The BABAR RPC System* in Proceedings of the 5th International Workshop on Resistive Plate Chambers and Related Detectors, Bari (Italy) 1999.

[30] D. Boutigny et al., SLAC-R-0443 (1994) 69.

[31] C. Bozzi et al., *Nucl. Instr. and Methods* **A447** (2000) 20.

[32] D. Barbieri et al., *Nuo. Cim.* **A112** (1999) 113.

[33] L. Bosisio, private communication of preliminary results.

[34] G. Della Ricca et al., *Nucl. Instr. and Methods* **A409** (1998) 258.

[35] V. Re at al., *Nucl. Instr. and Methods* **A409** (1998) 354.

[36] F. Lanni and F. Palombo, *Nucl. Instr. and Methods* **A379** (1996) 399.

[37] R. Claus et al., SLAC-PUB-8134 (1999).

[38] T.I. Meyer et al., Contribution to DPF 2000: Meeting of the Division of Particles and Fields of the American Physical Society, Columbus, Ohio, August 2000.

[39] Bergamo University, Ferrara University and INFN, Milano University and INFN, Pavia University and INFN, Pisa University and INFN and Scuole Normale Superiore, Torino University and INFN, Trieste University and INFN, Lawrence Berkeley National Laboratory, Stanford University, University of California Santa Barbara, University California of Santa Cruz, University of California San Diego, University of Maryland, Wisconsin University.

[40] Private comunication with Mario Bondioli, University of Pisa.

[41] Private comunication with Prof. Livio Lanceri, Univ. Trieste

[42] Statistical and Computational Methods in Data Analysis, Siegmund Brandt, North Holland Publishing.

[43] Private comunication with Eugenio Poloni, University of Pisa.

[44] Private comunication with Fernando Martinez Vidal, INFN Pisa.

[45] J. i. Tanaka, arXiv:hep-ex/0104053.

[46] E. M. Aitala *et al.* [E791 Collaboration], Phys. Rev. Lett. **83** (1999) 32 [arXiv:hep-ex/9903012].

[47] J. M. Link *et al.* [FOCUS Collaboration], Phys. Lett. B **485** (2000) 62 [arXiv:hep-ex/0004034].

[48] G. Bonvicini *et al.* [CLEO Collaboration], Phys. Rev. Lett. **82** (1999) 4586 [arXiv:hep-ex/9902011].

Contents